

BMO TR-80-40

SAI DOCUMENT NO. SAI-061-80-01-01

2
LEVEL III
A108848

AD A108849
PERFORMANCE TECHNOLOGY PROGRAM
(PTP-S II)

VOLUME X

MATERIAL CHARACTERIZATION OF POST-TEST ABLATION
MODELS

SCIENCE APPLICATIONS, INC.
MATERIAL SCIENCES OPERATION
IRVINE, CALIFORNIA 92715

APRIL, 1980

FINAL REPORT FOR PERIOD DECEMBER 1977 - JANUARY 1980

CONTRACT NO. F04701-77-C-0126

APPROVED FOR PUBLIC RELEASE; DISTRIBUTION UNLIMITED.

AIR FORCE BALLISTIC MISSILE OFFICE
NORTON AFB, CALIFORNIA 92409

DTIC
ELECTE
S DEC 28 1981 D

81 12 23 121

DTIC FILE COPY

This final report was submitted by Science Applications, Inc., 1200 Prospect Street, La Jolla, California 92038, under Contract Number FO4701-77-C-0126 with the Ballistic Missile Office, AFSC, Norton AFB, California. Major Kevin E. Yelmgren, BMO/SYDT, was the Project Officer in charge. This technical report has been reviewed and is approved for publication.

Kevin E. Yelmgren

KEVIN E. YELMGREN, Major, USAF
Chief, Vehicle Technology Branch
Reentry Technology Division
Advanced Ballistic Reentry Systems

FOR THE COMMANDER

Nicholas C. Belmonte

NICHOLAS C. BELMONTE, Lt Col, USAF
Director, Reentry Technology Division
Advanced Ballistic Reentry Systems

UNCLASSIFIED

SECURITY CLASSIFICATION OF THIS PAGE (When Data Entered)

REPORT DOCUMENTATION PAGE		READ INSTRUCTIONS BEFORE COMPLETING FORM
1. REPORT NUMBER BMD TR-80-40	2. GOVT ACCESSION NO. AD-A108 849	3. RECIPIENT'S CATALOG NUMBER
4. TITLE (and Subtitle) Performance Technology Program (PTP-S II), Vol. X, Material Characterization of Ground Test Models		5. TYPE OF REPORT & PERIOD COVERED Final
7. AUTHOR(s) D. A. Eitman J. E. DeMichaels		6. PERFORMING ORG. REPORT NUMBER SAI-061-80-01-01
9. PERFORMING ORGANIZATION NAME AND ADDRESS Science Applications, Inc. Material Sciences Operation 18872 Bardeen Ave., Irvine, California 92715		8. CONTRACT OR GRANT NUMBER(s) F04701-77-C-0126
11. CONTROLLING OFFICE NAME AND ADDRESS Ballistic Missile Office Norton AFB, California 92409		10. PROGRAM ELEMENT, PROJECT, TASK AREA & WORK UNIT NUMBERS
14. MONITORING AGENCY NAME & ADDRESS (if different from Controlling Office)		12. REPORT DATE January 1980
		13. NUMBER OF PAGES 154
		15. SECURITY CLASS. (of this report) Unclassified
		15a. DECLASSIFICATION/DOWNGRADING SCHEDULE
16. DISTRIBUTION STATEMENT (of this Report) Approved for Public Release; Distribution Unlimited.		
17. DISTRIBUTION STATEMENT (of the abstract entered in Block 20, if different from Report)		
18. SUPPLEMENTARY NOTES		
19. KEY WORDS (Continue on reverse side if necessary and identify by block number) Carbon-Carbon Composites Porosity Transition Surface Area Microstructure Roughness Processing Permeability		
20. ABSTRACT (Continue on reverse side if necessary and identify by block number) Characterization data is presented on twenty-four (24) carbon-carbon models which had been arc-jet ablation-tested and twenty-one (21) erosion samples from various ground tests. Materials include several construction, processing and yarn types. The characterization information presented includes photo-micrographs, measurements made using the photomicrographs and data from additional tests. The additional tests include mercury porosimetry, helium density, gas adsorption, bulk density and permeability.		

DD FORM 1 JAN 73 1473 EDITION OF 1 NOV 65 IS OBSOLETE

UNCLASSIFIED

42070-1 SECURITY CLASSIFICATION OF THIS PAGE (When Data Entered)

PREFACE

This document is the final technical report on the Material Characterization task of the SAMSO PTP-II program, Contract F04701-77-C-0126. This report presents characterization information on 45 ground tested specimens (24 ablation models and 21 erosion samples) examined in this program.

This task was conducted under the direction of D. A. Eitman as principal investigator. The program manager was J. F. Courtney. Captain J. W. Bohlen provided technical direction on this task for SAMSO.

Active support from the following agencies and corporations is acknowledged in supplying models and test information: Aerospace, AVCO, General Electric, McDonnell-Douglas, Naval Surface Weapons.

Accession For	
NTIS GRA&I	<input checked="checked" type="checkbox"/>
DTIC TAB	<input type="checkbox"/>
Unannounced	<input type="checkbox"/>
Justification	
By _____	
Distribution/ _____	
Availability Codes	
Dist	Avail and/or Special
A	

DTIC
ELECTE
DEC 28 1981
S D D

TABLE OF CONTENTS

	<u>Page</u>
SECTION 1.0 INTRODUCTION	1
SECTION 2.0 MATERIAL CHARACTERIZATION	4
2.1 Description of Characterization Tests	8
2.1.1 Microscopy	8
2.1.2 Density	8
2.1.3 Permeability	10
2.1.4 Internal Surface Area	10
2.1.5 Mercury Porosimetry	12
2.1.6 Porosity	12
2.2 Data Summaries	13
2.2.1 Structural Measurements	13
2.2.2 Permeability and Porosity	13
2.2.3 Microroughness Measurements	30
2.2.4 Macroroughness Measurements	31
2.3 Microscopy	53
2.4 Ablation Model Characterization	104
2.4.1 Yarn Effects on Matrix microstructure	104
2.4.2 Processing Facility Effects at Y-12 and MDAC	104
2.4.3 CVD Effects	105
2.4.4 Axially Symmetric Weave Geometries	106
2.4.5 Topographical Mapping of Ablation Models	107
SECTION 3.0 EROSION MODEL CHARACTERIZATION	108
3.1 Single Particle Impact Specimens	108
3.2 Holloman Sled Test Specimens	119
3.3 Ballistic Range (K)	121
3.4 Ballistic Range (G)	129

TABLE OF CONTENTS (Cont'd)

	<u>Page</u>
SECTION 4.0 CONCLUSIONS AND RECOMMENDATIONS	137
REFERENCES	139

LIST OF FIGURES

Figure	Title	Page
1.	Typical Ablation Model Cutting Plan	5
2.	Model Characterization Flow Diagram	6
3.	Schematic of Material Characterization Data Reduction	7
4.	Structural Measurement Schematic	9
5.	Optical Roughness Measurement	9
6.	Permeability Apparatus Schematic	11
7.	Typical Permeability Data for L-2 (FM1-221)	11
8.	Porosity Distribution for 233 T-50 Materials	18
9.	Porosity Distribution for 233 PAN Materials	19
10.	Porosity Distribution for 233 PAN, CVD Materials	20
11.	Porosity Distribution for 223 PAN, CVD, Materials	21
12.	Porosity Distribution for 223 PAN, HAT Materials	22
13.	Porosity Distribution for 223 FWPF, PAN Materials	23
14.	Porosity Distribution for FWPF PAN Materials	24
15.	Porosity Distribution for Pitch Materials	25
16.	Porosity Distribution for FWPF, LOPIC Processed Material	26
17.	Porosity Distribution for Jellyroll Material	27
18.	Microroughness Height Distribution for GE-01A (GE 223 T-50, Laminar)	33
19.	Microroughness Height Distribution for GE-07A (223 T-50, Turbulent)	33
20.	Microroughness Height Distribution for GE-02A3 (223 T-50, MDAC, Laminar)	34
21.	Microroughness Height Distribution for SR-10D (223 PAN, No CVD, Laminar)	34
22.	Microroughness Height Distribution for SR-120 (223 PAN, No CVD, initial LOPIC, Laminar)	35
23.	Microroughness Height Distribution for SR-13D (223 PAN, CVD, 2300°C Graph, Laminar)	35
24.	Microroughness Height Distribution for GE-39A (223 PAN, CVD, Laminar)	36
25.	Microroughness Height Distribution for GE-44A (223 PAN, CVD, Laminar)	36

LIST OF FIGURES (Cont'd)

Figure	Title	Page
26.	Microroughness Height Distribution for 427-HS1 (223 PAN, CVD, Laminar)	37
27.	Microroughness Height Distribution for 427-HS2 (223 PAN, CVD, Laminar)	37
28.	Microroughness Height Distribution for 658-11-HS2 (223 PAN, CVD, Laminar)	38
29.	Microroughness Height Distribution for GE-04A3 (223 PAN, HAT, Turbulent)	38
30.	Microroughness Height Distribution for HAT 5 (223 PAN, HAT, Turbulent)	39
31.	Microroughness Height Distribution for PF928-HS2 (FWPF PAN, LoPIC, Laminar)	39
32.	Microroughness Height Distribution for PF928-HS3 (FWPF PAN, Laminar)	40
33.	Microroughness Height Distribution for GE-06A3 (FWPF PAN, Laminar)	40
34.	Microroughness Height Distribution for GE-02PA (FWPF PAN, Laminar)	41
35.	Microroughness Height Distribution for SR-25PA (FWPF PAN, Laminar)	41
36.	Microroughness Height Distribution for SR-07AD (Pitch, No CVD, Laminar)	42
37.	Microroughness Height Distribution for SR-08AD (Pitch with CVD, Laminar)	42
38.	Microroughness Height Distribution for AFML-23R (FWPF, Laminar)	43
39.	Macroroughness Height Distribution for GE-01A (GE 223 T-50, Laminar)	47
40.	Macroroughness Height Distribution for GE-07A (223 T-50, Turbulent)	47
41.	Macroroughness Height Distribution for GE-02A3 (223 T-50, MDAC, Laminar)	47
42.	Macroroughness Height Distribution for SR-10D (223 PAN, No CVD, Laminar)	47
43.	Macroroughness Height Distribution for SR-12D (223 PAN, No CVD, initial LoPIC, Laminar)	48
44.	Macroroughness Height Distribution for SR-13D (223 PAN, CVD, 2300°C Graph, Laminar)	48
45.	Macroroughness Height Distribution for GE-39A (223 PAN, CVD, Laminar)	48

LIST OF FIGURES (cont'd)

Figure	Title	Page
46.	Macroroughness Height Distribution for GE-44A (223 PAN, CVD, Laminar)	48
47.	Macroroughness Height Distribution for 427-HS1 (223 PAN, CVD, Laminar)	49
48.	Macroroughness Height Distribution for 427-HS2 (223 PAN, CVD, Laminar)	49
49.	Macroroughness Height Distribution for 668-11-HS2 (223 PAN, CVD, Laminar)	49
50.	Macroroughness Height Distribution for GE-04A3 (223 PAN, HAT, Turbulent)	49
51.	Macroroughness Height Distribution for HAT 5 (223 PAN, HAT, Turbulent)	50
52.	Macroroughness Height Distribution for PF928-HS2 (FWPF, PAN, LoPIC, Laminar)	50
53.	Macroroughness Height Distribution for PF928HS3 (FWPF, PAN, Laminar)	50
54.	Macroroughness Height Distribution for GE-06A3 (FWPF, PAN, Laminar)	50
55.	Macroroughness Height Distribution for GE-02PA (FWPF, PAN, Laminar)	51
56.	Macroroughness Height Distribution for SR-25PA (FWPF, PAN, LoPIC, Laminar)	51
57.	Macroroughness Height Distribution for SR-07AD (Pitch, No CVD, Laminar)	51
58.	Macroroughness Height Distribution for SR-07AD (Pitch with CVD, Laminar)	51
59.	Macroroughness Height Distribution for AFML-23R (FWPF, LoPIC, Laminar)	52
60.	Macroroughness Height Distribution for AFML-19R (Jellyroll, Laminar)	52
61.	Effect of Roughness Element Spacing and Shape in Equivalent Sand Roughness	53
62.	Photomicrographs of GE-01A (GE 223 T-50, Laminar)	54
63.	Photomicrographs of GE-07A (223 T-50, Turbulent)	56
64.	Photomicrographs of GE-02A3 (223 T-50, MDAC, Laminar)	58
65.	Photomicrographs of SR-10D (223 PAN, no CVD, Laminar)	60
66.	Photomicrographs of SR-12D (223 PAN, no CVD, Initial LoPIC, Laminar)	62

LIST OF FIGURES (Con'td)

Figure	Title	Page
67.	Photomicrographs of SR-13D (223 PAN, CVD, Laminar)	64
68.	Photomicrographs of GE-39A (223 PAN, CVD, Laminar)	66
69.	Photomicrographs of GE-44A (223 PAN, CVD, Laminar)	68
70.	Photomicrographs of 427-HS1 (223 PAN, CVD, Laminar)	70
71.	Photomicrographs of 427-HS2 (223 PAN, CVD, Laminar)	72
72.	Photomicrographs of 668-11-HS2 (223 PAN, CVD, Laminar)	74
73.	Photomicrographs of GE-04A3 (223 PAN, HAT, Laminar)	77
74.	Photomicrographs of HAT 5 (223 PAN, HAT, 10KSI Processing, Turbulent)	79
75.	Photomicrographs of GE-06A3 (FWPF PAN, Laminar)	81
76.	Photomicrographs of GE-02PA (FWPF PAN, Laminar)	84
77.	Photomicrographs of SR-25FA (FWPF PAN, Laminar)	86
78.	Photomicrographs of PF928-HS2 (FWPF PAN, Laminar)	89
79.	Photomicrographs of PF928-HS3 (FWPF PAN, Laminar)	91
80.	Photomicrographs of SR-07AD (Pitch, no CVD, Laminar)	94
81.	Photomicrographs of SR-08AD (Pitch with CVD, Laminar)	96
82.	Photomicrographs of AFML-23R (FWPF T-50, LoPIC, Laminar)	98
83.	Photomicrographs of AFML-19R (Jellyroll, Laminar)	100
84.	Photomicrographs of AC02N and AC-03N (FWPF PAN, Laminar)	102
85.	Cross Section Showing Effect of Single Particle Impact at Room Temperature on Axial Yarns of 223 T-50	110
86.	Cross Section Showing Effect of Single Particle Impact at Room Temperature on Transverse Yarns of 223 T-50	111
87.	Cross Section Showing Effect of Single Particle Impact at Room Temperature on Axial Yarns of 223 PAN	112
88.	Cross Section Showing Effect of Single Particle Impact at Room Temperature on Transverse Yarns of 223 PAN	113
89.	Cross Section Showing Effect of Single Particle Impact Elevated Temperature on Axial Yarns of 223 T-50	115
90.	Cross Section Showing Effect of Single Particle Impact at Elevated Temperature on Transverse Yarns of 223 T-50	116

LIST OF FIGURES (Cont'd)

Figure	Title	Page
91.	Cross Section Showing Effect of Single Particle Impact at Elevated Temperature on Axial Yarns of 223 PAN	117
92.	Cross Section Showing Effect of Single Particle Impact Elevated Temperature on Transverse Yarns of 223 PAN	118
93.	View of In-Depth Damage Resulting from Small Particle Impacts	120
94.	Cross Section of Holloman Sled Tested 223 T-50	122
95.	Cross Section of Holloman Sled Tested 223 PAN	123
96.	Cross Section of Holloman Sled Tested FWPF PAN	124
97.	Cross Section of Holloman Sled Tested 1-1-1-3 Showing Isolated In-Depth Damage	125
98.	Cross Section of Holloman Sled Tested SSN Material	126
99.	Cross Section Showing Transverse Yarns in Holloman Sled Tested SSN Material	127
100.	Cross Sections Showing Effects of Single Impact and Two Impacts on Standard 223	128
101.	Cross Section Showing the Effect of a Single Impact on 223 PAN	130
102.	Cross Section Showing the Effect of Two Impacts on 223 PAN	131
103.	Cross Sections of GE 223 T-50 Showing Effect of Impact by Welding Debris on Initial Part of Flight	132
104.	Cross Sections of GE 223 T-50 Impacted by Dust	133
105.	Cross Sections of GE 223 T-50 Impacted by Snow	134
106.	Cross Sections of 223 PAN Impacted by Dust	135
107.	Cross Sections of 223 PAN Impacted by Snow	136

LIST OF TABLES

Table	Title	Page
1	Materials Selected for Post-Test Ablation Model Characterization	2
2	List of Samples Characterized According to Material	3
3	Unit Cell Structural Measurements	14
4	Permeability and Porosity Measurements	17
5	Microroughness Measurements	32
6	Microroughness Measurements	46
7	Model Test and Material Description	140

1.0 INTRODUCTION

A wide range of carbon-carbon composites are available for use as reentry vehicle nosetip material. These include several varieties of well-defined baseline materials, which are being evaluated in current flight-test programs, as well as developmental materials aimed at altering either performance characteristics or end-item costs and availability for DOD selection. Key variables in the microstructural makeup of these materials include the yarn type, weave geometry and processing history. Each of these contributes to the finished composite's ablation and erosion performance and are, to a large extent, elements which can be easily changed by material developers. These various carbon-carbon materials can be assessed by performing ablation and erosion ground tests and subsequently obtaining microstructural characterization information on the tested model to determine the role of each parameter of the material's makeup in the simulated flight test environment. In addition, the characterization information may also be used for making comparisons between test materials to define material variability and for a general assessment of weaving and process related defects which have been observed in the microstructure of prior materials.

For this program a selection was made of materials which represented several areas of interest to the Air Force. A list of these materials and the objective addressed in each case, is shown in Table 1. A total of 24 ablation models and 21 erosion specimens have been characterized and documented in this report. A complete list of the ablation models is presented in Table 2 which delineates the characterized models according to construction, billet identification, processing history, and final tested model appearance (laminar or turbulent).

TABLE 1. Materials Selected for Post-Test Ablation Model
Characterization

OBJECTIVE	MATERIAL DESCRIPTION	ISSUES ADDRESSED
Flight Test Support	<ul style="list-style-type: none"> • 223 material with both PAN and T-50 reinforcement. • Five FWPF (PAN) materials • One billet of 223 PAN with no CVD and 10 ksi processing 	<ul style="list-style-type: none"> • Differences in processor's end product. • Comparison with prior material characteristics • General material quality
New Material Construction	<ul style="list-style-type: none"> • AVCO "Jellyroll" with LoPIC densification 	<ul style="list-style-type: none"> • Relate microstructure to existing data base
Processing Variation Effects	<ul style="list-style-type: none"> • 223 PAN (No CVD) with and without initial LoPIC • 223 PAN with low temperature graphitization (2300°C) 	<ul style="list-style-type: none"> • Effect of initial LoPIC • Effect of graphitization temperature on microstructure
New Yarn Examination	<ul style="list-style-type: none"> • Pitch yarn material processed both with and without CVD 	<ul style="list-style-type: none"> • Initial comparison of pitch yarn reinforcement to T-50 and HM

TABLE 2. List of Samples Characterized
According to Material

223 (or Equivalent Construction)	FWPF	Jellyroll
<ul style="list-style-type: none"> Standard, T-50 GE-01A (399, L) GE-02A3 (408, L) GE-07A (425, T) 	<ul style="list-style-type: none"> T-50, LOPIC AFML-23R (881, L) 	AFML-19R (JR-4-2, L)
<ul style="list-style-type: none"> PAN -with CVD GE-39A (426, L) GE-44A (427, L) SR-13D (1819-2, L) *427-HS1 (427, L) *427-HS2 (427, L) *668-11-HS2 (668-11, L) 	<ul style="list-style-type: none"> PAN AC-02N (921, L) AC-03N (921, L) GE-06A3 (PF920, L) GE-02PA (PF928, L) SR-25PA (903-1-RZ2, L) *PF928-HS2 (PF928, L) *PF928-HS3 (PF928, L) 	

-No CVD

- GE-04A3 (HAT, T)
- SR-1CD (1819-3, L)
- SR-12D (1819-5, L)
- HAT 5 (T)

- Pitch Yarn
- with CVD
- SR-08AD (111P2, L)
- No CVD
- SR-07AD (111P1, L)

LEGEND

Model (billet number, laminar or turbulent model)

Test Mode For All Samples except*
is Ramp, Peaked Enthalpy

*Tested in Steady State Mode

Erosion samples from single particle impact tests, and various range tests (Holloman, AEDC K and AEDC G) are shown in Section 3 of this report. These samples clearly show that differences exist in material response between single particle impact and range tests. The coupling of flowfield and impact damage appears to be responsible for the major differences observed.

2.0 MATERIAL CHARACTERIZATION

Material characterization of post-test ablation models provides both qualitative and quantitative information for consideration of the influence of material microstructure on ablation performance.

The characterization plan relies on obtaining information from the tested ablation model to accurately represent local microstructural effects. A typical cutting plan is shown in Figure 1. The ablated portion is used for microscopy while other characterization tests are being run on the aft end of the specimen. A flow diagram of the complete model characterization cycle is shown in Figure 2. A series of computer programs developed for coupled data reduction (Figure 3) are used to provide quantitative descriptions for modeling efforts.

Subjective information from microstructural observations may be used to indicate processing parameters having the potential for improving ablation and performance. These observations include the response of each constituent in the carbon-carbon composite to the processing environment and to the resultant structure. Quantitative measurements are made using photomicrographs to determine surface roughness, pore structure, and weave geometry. Further tests are conducted to determine permeability, internal surface area, and open and closed porosity. The data is then reduced to arrive at a format which is consistent with its application in analytical ablation models.

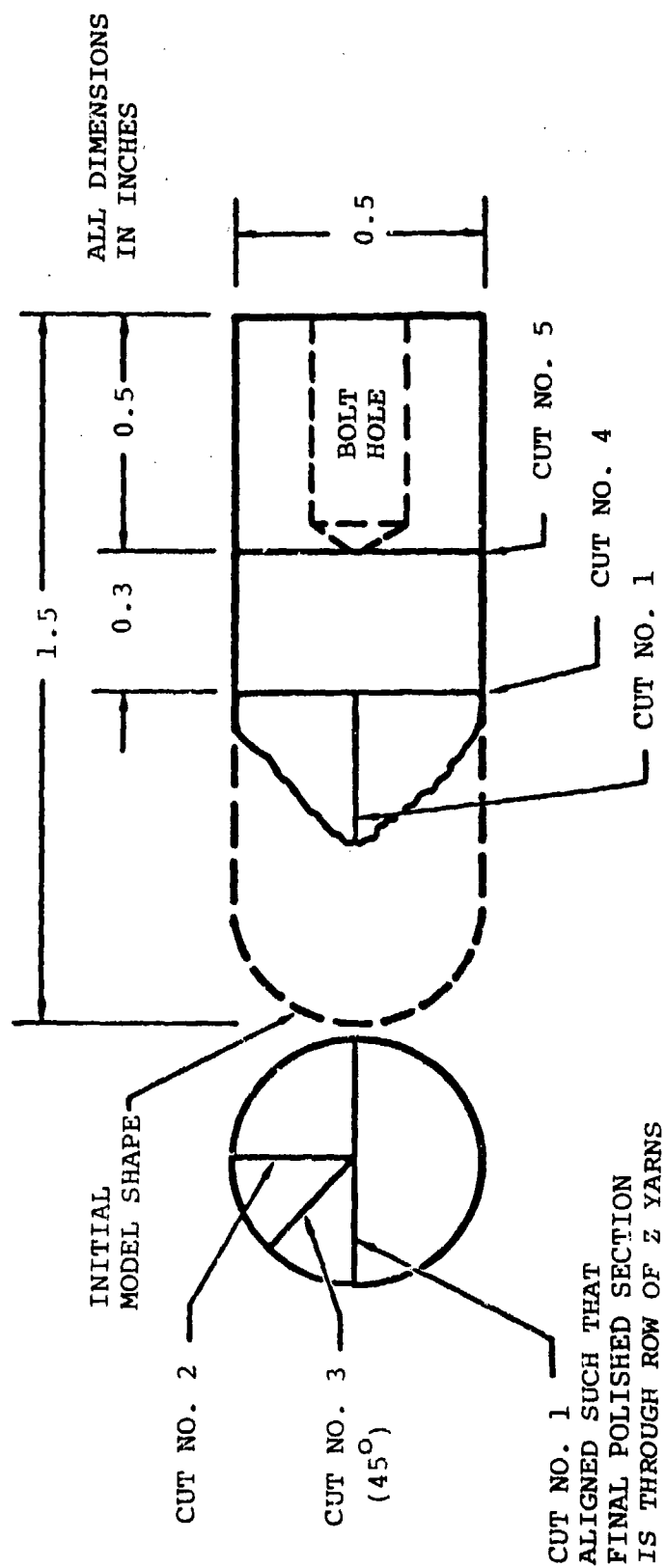


Figure 1. TYPICAL ABLATION MODEL CUTTING PLAN

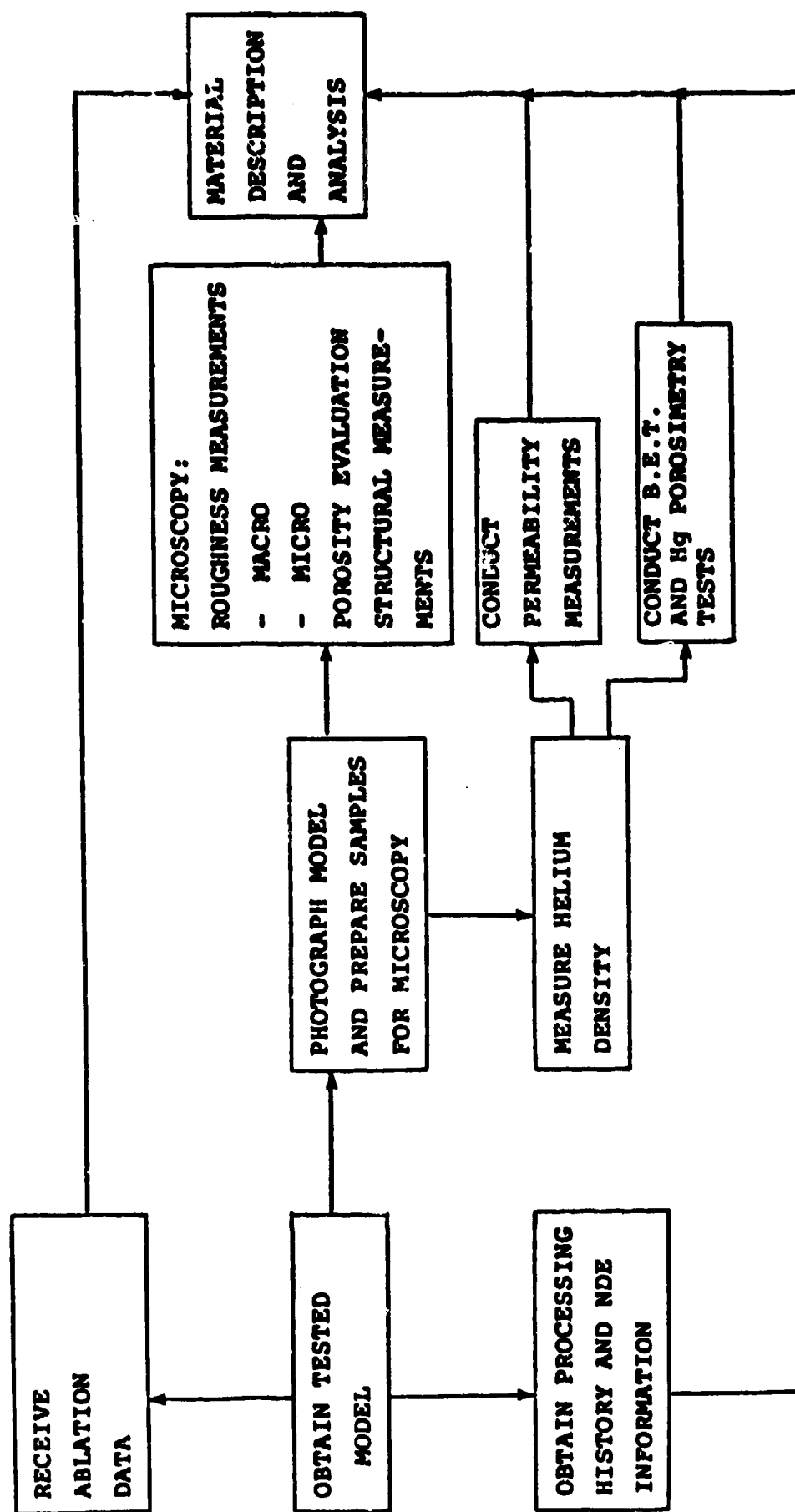


Figure 2. MODEL CHARACTERIZATION FLOW DIAGRAM

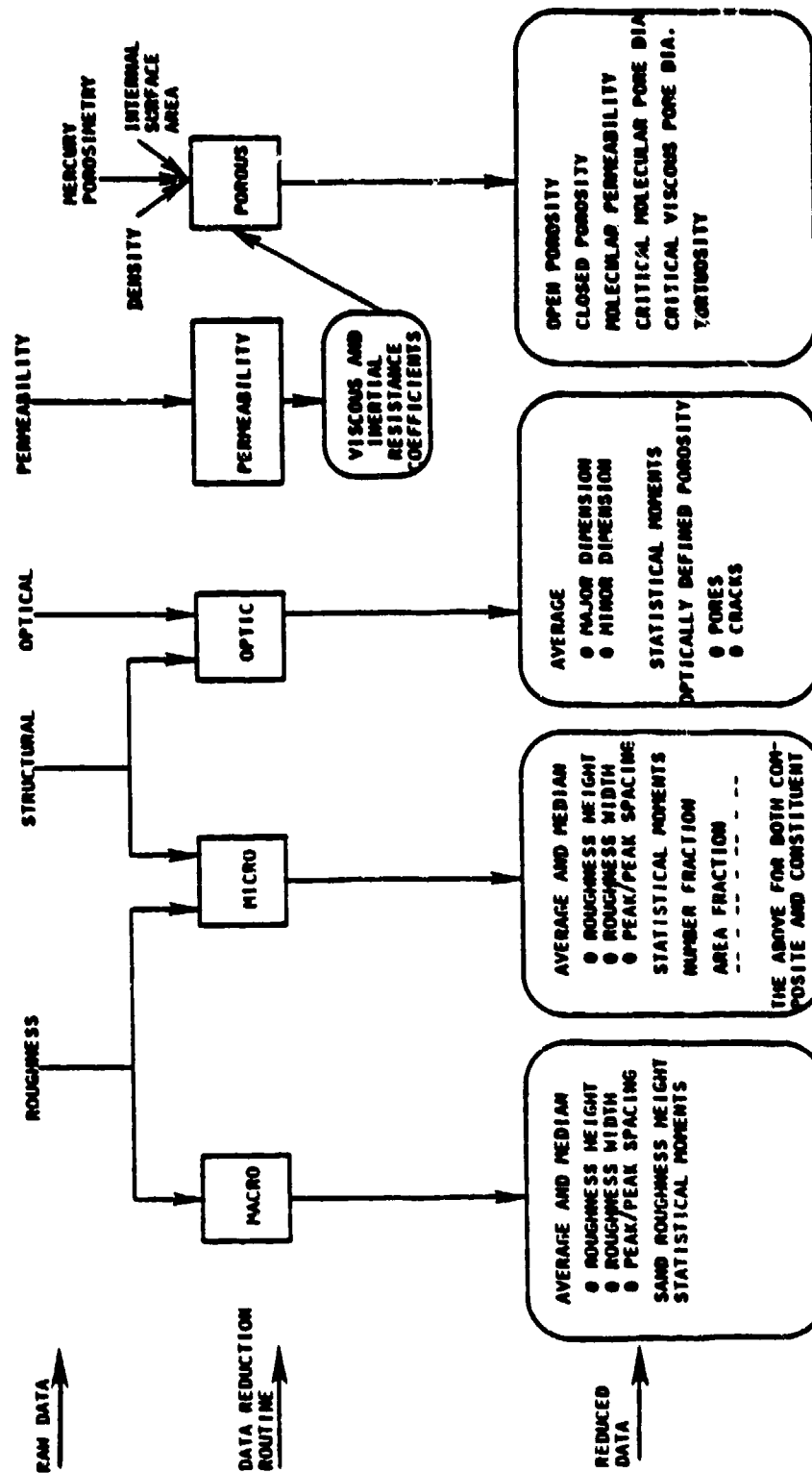


Figure 3. SCHEMATIC OF MATERIAL CHARACTERIZATION DATA REDUCTION

2.1 Description of Characterization Tests

A description of characterization methods being used on this program is presented in the following paragraphs. Data obtained is presented in Sections 2.2 and 2.3.

2.1.1 Microscopy - Following an initial inspection, macrophotographs were taken to characterize the developed shape and symmetry of each ablation model. These photographs included an overall view and sufficient top views (including a stereo pair) to show asymmetries and/or preferential transition locations. The models were then sectioned and vacuum mounted in thermosetting plastic for maximum edge retention during subsequent polishing. Photomicrographs were taken at approximately 25, 50, and 350X (see Section 2.3). Structural parameters and pore sizes were measured optically on the 25X photomicrographs, macroroughness was measured at 50X and microroughness was measured at 350X.

The structural measurements made are shown schematically in Figure 4 and are reported in Section 2.3. This information is used to describe the unit cell geometry for calculating the area of each composite constituent on the ablated surface and for calculating optical pore volumes from measurements made on each cross-section.

Roughness measurements of the height (h), width (w) and peak-to-peak distance (L_p) were made at both 50 and 350X. The roughness height measurements were made from an optically defined mean surface as indicated in Figure 5. This procedure was used to eliminate undue influence of deep pores intersecting the ablation surface. The measured roughness heights, distributions and calculated roughness quantities are reported in Section 2.3.

2.1.2 Density - Composite densities were measured using several different techniques. Dimensions and weights on regularly shaped

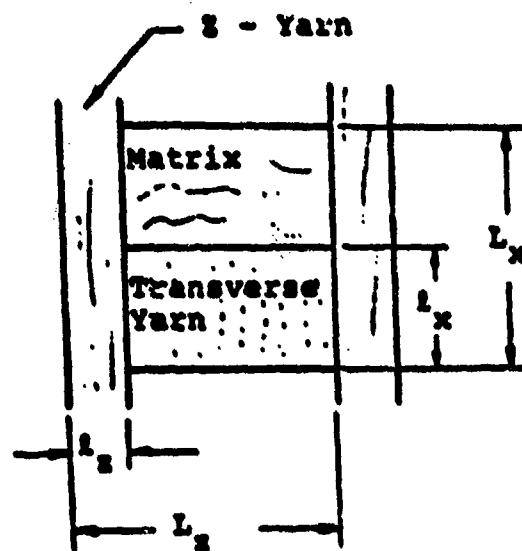


Figure 4. STRUCTURAL MEASUREMENT SCHEMATIC

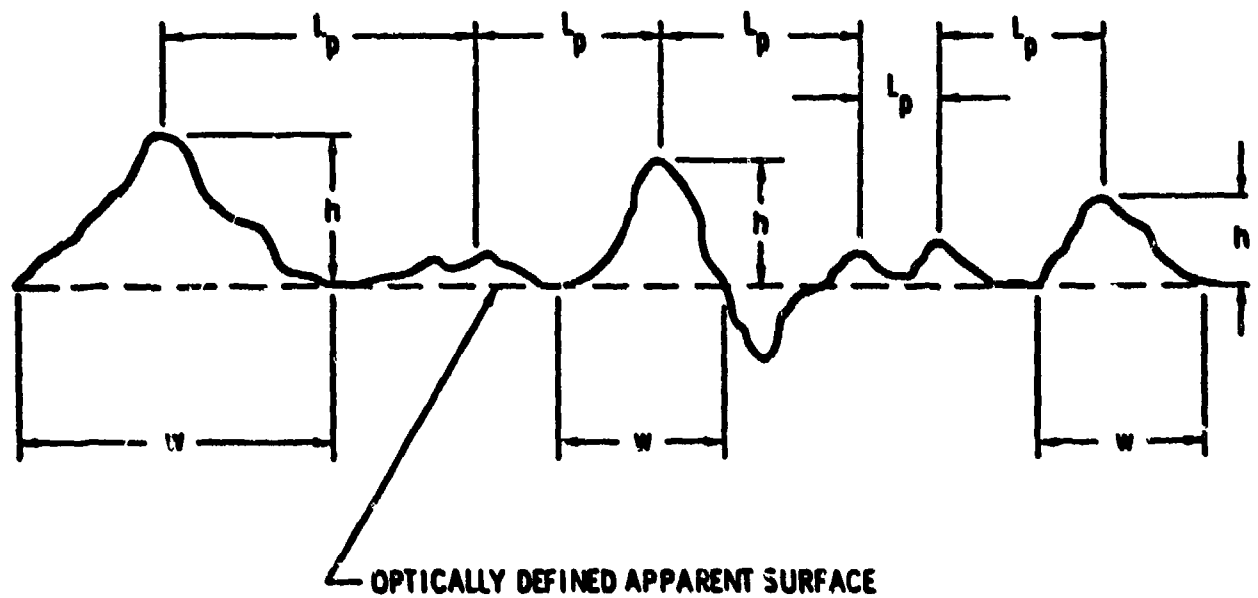


Figure 5. OPTICAL ROUGHNESS MEASUREMENT

specimens were used to determine bulk density (ρ_o). The apparent density was measured using an immersion technique on irregular, large samples. Helium density (ρ_{He}) was determined using a helium-gas pycnometer to measure the volume of helium gas the specimen displaced. Since the helium permeates open pores of a sample, this measurement, combined with the bulk density, gives the open porosity of the composite.

2.1.3 Permeability - Permeability measurements were made on machined samples 0.3 inches diameter by 0.3 inches long. The apparatus is shown schematically in Figure 6. The flowmeters used are capable of measuring flow rates as low as 5×10^{-5} CFM ($1.3 \text{ cm}^3/\text{min.}$).

The permeability test procedure involves measuring the flow rate of nitrogen gas through a sample for selected values of gas pressure incident on the upstream face of the sample. Flow rate was then directly related to pressure differential by the test measurements. The viscous and inertial resistance coefficients of each material were determined from permeability data using plots such as those shown in Figure 7 (Ref. 5). Plotted in this manner, experimental data should fall in a straight line. The intercept on the abscissa is the viscous resistance coefficient, α , while the slope is the inertial resistance coefficient, β .

Additional calculations of the molecular permeability, B , and tortuosity, τ^2 , were made using this data in combination with other information about the pore structure.

2.1.4 Internal Surface Area - The internal open surface area (S_a) was measured using the BET method (Reference 1). This method assumes multilayer adsorption of gases on solid surfaces using a modification of the Langmuir equations. In general, this technique requires measurement of gas adsorption at several different pressures. The type of gas used must also be considered,

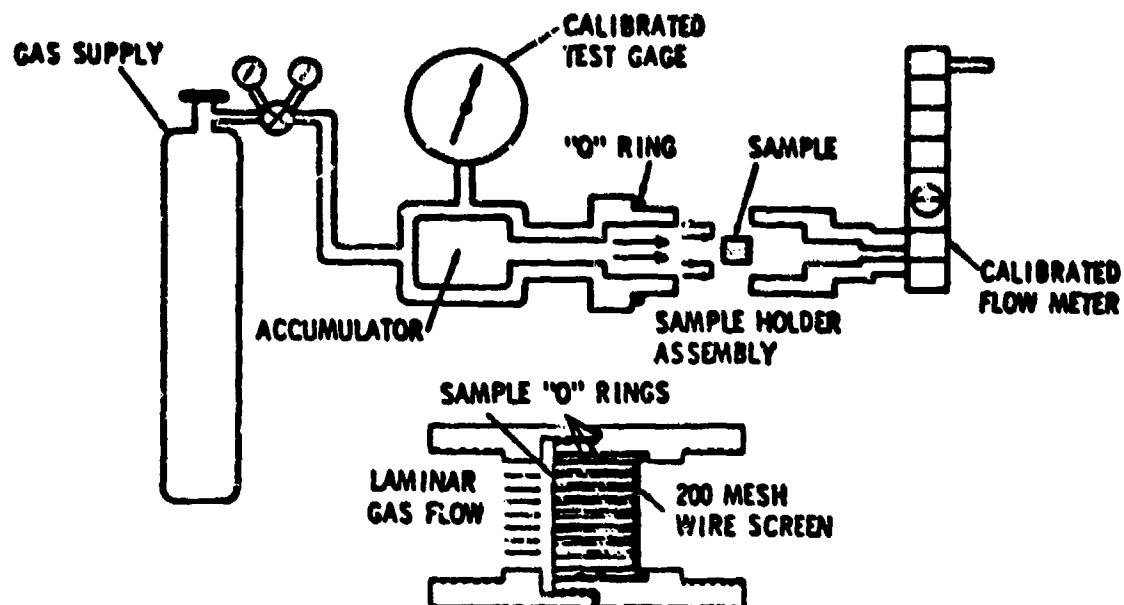


Figure 6. PERMEABILITY APPARATUS SCHEMATIC

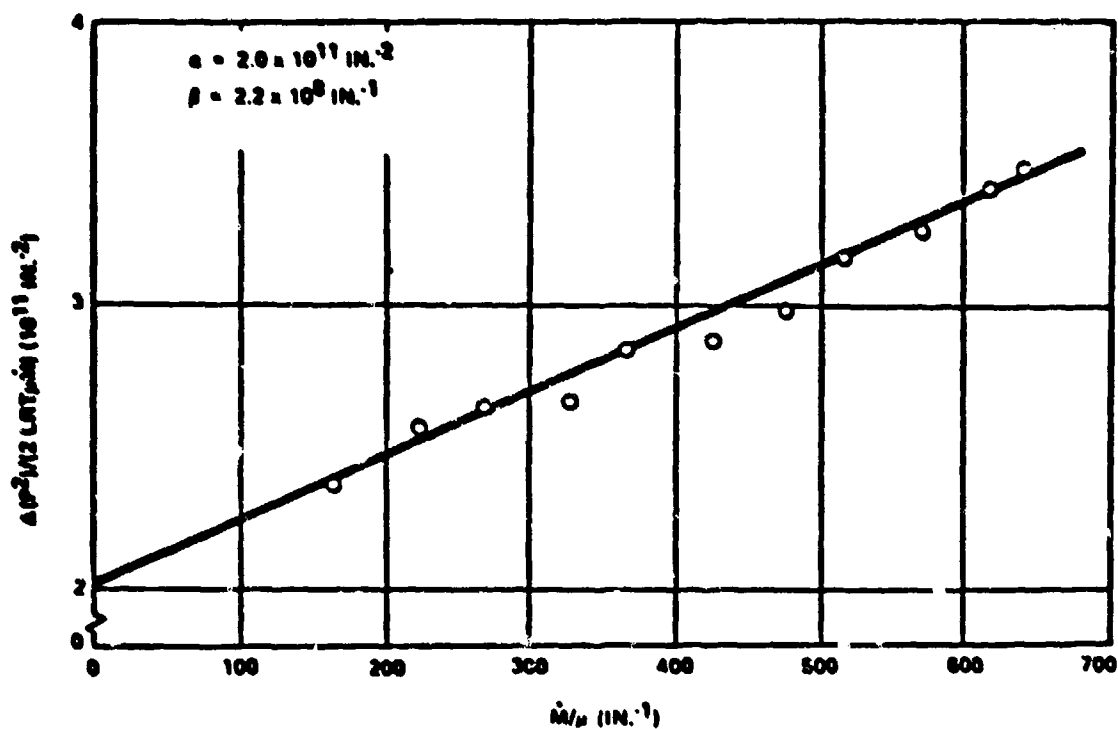


Figure 7. TYPICAL PERMEABILITY DATA FOR L-2 (FMI-221)

since chemisorption and catalytic effects can influence the results. Based on the results reported in Reference 2, krypton gas adsorption was selected for use in determining internal surface area.

2.1.5 Mercury Porosimetry - Mercury porosimetry measurements were made on material from the aft end of most tested ablation models. The technique used was to immerse the sample in a mercury bath and raise the hydrostatic pressure gradually to 60,000 psi (4080 ATM) while recording the volume of mercury intruded. When the mercury volume was corrected for compressibility, a measure of the specific void volume of the sample (V_α) was obtained as a function of apparent pore size. The apparent pore diameter was obtained using the contact angle for mercury and indicates the smallest size of the microporosity connecting the larger pores in the material. This data is used to evaluate the molecular permeability, tortuosity, and mean viscous molecular pore diameters in combination with the permeability data.

2.1.6 Porosity - The total porosity of each composite was determined using several techniques. The open porosity calculation used helium and bulk density data (ρ_{He} and ρ_o respectively.) The closed porosity was calculated by using both the helium density and the final density (ρ_f) of the material obtained in the mercury porosimetry tests. In this case, the assumption was made that 60,000 psi, which corresponds to pore diameters of 0.003 microns, filled virtually all of the closed porosity. The porosity calculations were made as follows:

$$\epsilon_o = 1 - \frac{\rho_o}{\rho_{He}} \quad (\text{Open Porosity})$$

$$\epsilon_c = 1 - \frac{\rho_{He}}{\rho_f} \quad (\text{Closed Porosity})$$

The data from helium density, bulk density and mercury porosimetry tests were then combined with optical pore measurements for an overall description of the porosity. Porosity data is presented in Section 2.2.

2.2 Data Summaries

Data obtained from measurements on photomicrographs and various characterization tests have been reduced and are presented in this section. Some limited analytical considerations which have been applied to improve the utility of the numerical output for modeling are also presented.

A reference page (Table 7) at the end of this report detailing model numbers, ablation environment, and material descriptions is provided for convenient reference while reviewing data presented in this section.

2.2.1 Structural Measurements - The structural measurements made are tabulated in Table 3. Figure 4 is a schematic of a unit cell in a 3-D composite with appropriate labels designating the measurements taken. Since, for 3-D composites, the 2 yarns are either square or, for the case of Fine Weave Pierced Fabric (FWPF), are round in cross-section, these measurements are sufficient to completely describe the composite unit cell. It should be noted that the difference between l_x and $L_x/2$ indicates the degree of transverse yarn billowing ($l_x > L_x/2$) or shrinking ($l_x < L_x/2$).

2.2.2 Permeability and Porosity - Critical tests to define the microstructural characteristics of carbon-carbon composites consist of bulk and helium density measurements, permeability measurements of porosity. Data from these tests and some analytical permeability terms are presented in Table 4. Porosity data is also summarized in Figures 8 through 17.

TABLE 3 UNIT CELL STRUCTURAL MEASUREMENTS

MODEL	MATERIAL	CONDITION	L_x (MILS)	L_x (MILS)	L_z (MILS)	L_z (MILS)
AFML-19R	Jellyroll	Laminar	(8.42 Layer Spacing)			
AFML-23R	FWPF (LOPIC)	Laminar	11.81	22.05	22.00	51.07
GE-01A	GE-223 T-50	Laminar	15.91	33.30	17.30	29.66
GE-02A3	223 T-50 (MDAC)	Laminar	17.32	36.22	17.13	29.53
GE-04A3	223 (PAN, HAT)	Turbulent	15.75	32.48	17.52	29.33
GE-06A3	FWPF (PAN)	Laminar	12.95	19.97	25.40	52.06
SR-07AD	FMI (Pitch)	Laminar	20.87	45.43	17.66	32.56
SR-08AD	FMI (Pitch, CVD)	Laminar	21.30	49.41	15.71	31.72
SR-10D	223 (PAN NO CVD)	Laminar	15.75	36.13	18.47	30.39
SR-12D	223 (PAN NO CVD)	Laminar	15.45	33.75	19.56	30.62
SR-13D	223 (PAN, CVD)	Laminar	15.14	35.40	18.17	29.50
GE-07A	223 T-50	Turbulent	15.75	33.07	16.93	29.53
GE-39A	223 (PAN)	Laminar	16.26	35.00	17.22	28.08
GE-44A	223 (PAN)	Laminar	18.70	42.52	16.93	28.94
AC-02N	FWPF (PAN)	Laminar	13.58	21.46	21.26	50.98
AC-03N	FWPF (PAN)	Laminar	13.98	21.26	24.21	52.56

Table 3 (Cont.) UNIT CELL STRUCTURAL MEASUREMENTS

MODEL	MATERIAL	CONDITION	ℓ_x (MILS)	L_x (MILS)	ℓ_z (MILS)	L_z (MILS)
GE-02PA	FWPF (PAN)	Laminar	12.44	20.79	25.35	52.91
SR-25PA	FWPF (PAN, LOPIC)	Laminar	10.55	20.31	26.77	52.60
HAT 5	223 (PAN)	Turbulent	7.87	12.91	7.87	11.81
427-HS1	223 (PAN,CVD)	Laminar	14.09	35.12	15.75	27.40
427-HS2	223 (PAN,CVD)	Laminar	13.23	33.39	16.85	28.66
PF928- HS2	FWPF (PAN)	Laminar	9.45	17.48	24.25	54.33
PF928- HS3	FWPF (PAN)	Laminar	9.39	14.27	21.54	52.00
668-11- HS2	223 (PAN,CVD)	Laminar	16.94	34.87	16.91	28.79

The items listed in Table 4 are summarized below:

ρ_o = Bulk density

ρ_{He} = Helium density

ϵ_o = % Open porosity

ϵ_c = % Closed porosity

ϵ_{opt} = % Porosity from optical measurements

α = Viscous resistance coefficient

β = Inertial resistance coefficient

D_v = Viscous mean pore diameter

D_M = Molecular mean pore diameter

B = Permeability coefficient

τ^2 = Tortuosity

S_a = Open internal surface area

Table 4 PERMEABILITY AND POROSITY MEASUREMENTS

MODEL	MATERIAL	CONDITION	ρ_o (g/cc)	ρ_{He} (g/cc)	ϵ_o (%)	ϵ_c (%)	ϵ_{opt} (10^{10} in^{-2})	α	β (10^7 in^{-2})	D_v (u)	D_H (μ)	B $\frac{1}{K}$	$\frac{1}{\tau^2}$	S_1 ($\text{m}^2 \cdot \text{g}$)
AFML-19R	Jellyroll	Laminar	1.92	2.035	5.65	2.48	-	-	-	-	-	-	-	0.2037
AFML-23R	FUPF (LOPIC)	Laminar	1.928	2.011	4.13	2.73	4.619	47.7	3.79	2.457	2.010	14.41	11.52	0.2431
GE-01A	GE 223(T-50)	Laminar	1.830	1.940	5.67	5.06	7.545	4.61	3.91	3.743	3.021	96.58	3.547	0.2906
GE-02A3	223(T-50, MDAC)	Laminar	1.827	1.978	7.63	3.67	4.634	6.40	5.62	3.013	1.828	64.94	4.297	0.3203
GE-04A3	223 (PAN, NAT)	Turbulent	1.883	2.032	7.33	3.85	5.587	34.4	218.00	1.426	0.9284	27.37	4.974	0.3460
GE-06A3	FUPF (PAN)	Laminar	1.929	2.079	7.22	4.30	5.568	11.7	57.1	2.909	1.945	40.69	6.899	0.3090
SR-07AD	FMI (Pitch)	Laminar	1.919	2.071	7.34	3.40	4.486	7.65	5.72	2.404	1.574	84.54	2.732	0.3689
SR-08AD	FMI (PITCH, CVD)	Laminar	1.918	2.068	7.25	3.95	3.834	4.87	4.60	2.513	1.649	110.60	2.142	0.3456
SR-10D	223 (PAN, CVD)	Laminar	1.917	2.082	7.93	2.50	3.823	11.40	10.7	2.616	1.621	42.82	5.999	0.2434
SR-12D	223 (PAN, CVD)	Laminar	1.957	2.089	6.32	2.23	7.085	4.46	3.66	5.140	3.497	61.26	7.214	0.2261
SR-13D	223 (PAN, CVD)	Laminar	1.830	1.930	5.18	3.32	5.478	6.88	3.66	5.449	4.334	43.81	10.250	0.2501
GE-07A	223(T-50)	Turbulent	1.837	1.965	6.51	5.59	5.218	5.78	6.87	2.379	1.606	101.40	2.064	0.3367
GE-39A	223 (PAN, CVD)	Laminar	1.849	2.021	8.51	2.60	2.429	17.70	5.50	1.280	0.7789	55.42	2.392	0.3152
GE-44A	223 (PAN, CVD)	Laminar	1.880	2.023	7.07	2.98	2.980	14.60	9.03	1.639	1.205	50.48	3.375	0.3683
AC-02M	FUPF (PAN)	Laminar	-	-	-	-	3.044	-	-	-	-	-	-	-
AC-03M	FUPF (PAN)	Laminar	-	-	-	-	4.930	-	-	-	-	-	-	-
GE-02PA	FUPF (PAN)	Laminar	2.014	2.097	3.96	3.66	3.089	6.61	8.54	5.200	4.900	56.598	6.853	0.2605
SR-25PA	FUPF (PAN, LOPIC)	Laminar	1.892	2.040	7.25	2.22	4.705	13.72	36.05	2.800	2.500	47.983	7.560	0.2265
NAT 5	223 (PAN, NAT)	Turbulent	1.892	2.033	6.94	1.22	4.403	46.38	148.29	2.000	1.700	18.918	12.465	0.2012
427-HS1	223 (PAN, CVD)	Laminar	1.899	2.038	8.97	1.44	3.692	14.47	5.69	1.100	0.900	10.612	1.157	0.4299
427-HS2	223 (PAN, CVD)	Laminar	1.901	2.038	6.72	1.88	3.467	17.6	7.75	1.000	0.800	92.787	1.159	0.3854
PF928-HS2	FUPF (PAN)	Laminar	2.016	2.097	3.86	4.08	3.932	14.1	16.91	2.400	2.300	58.466	1.792	0.2257
PF928-HS3	FUPF (PAN)	Laminar	2.014	2.135	5.67	1.09	3.679	14.06	12.80	1.600	1.400	80.301	2.352	0.2206
668-11-HS2	223 (PAN, CVD)	Laminar	1.921	2.025	5.14	3.39	3.548	20.61	1.25	2.300	2.200	41.659	5.424	0.2866

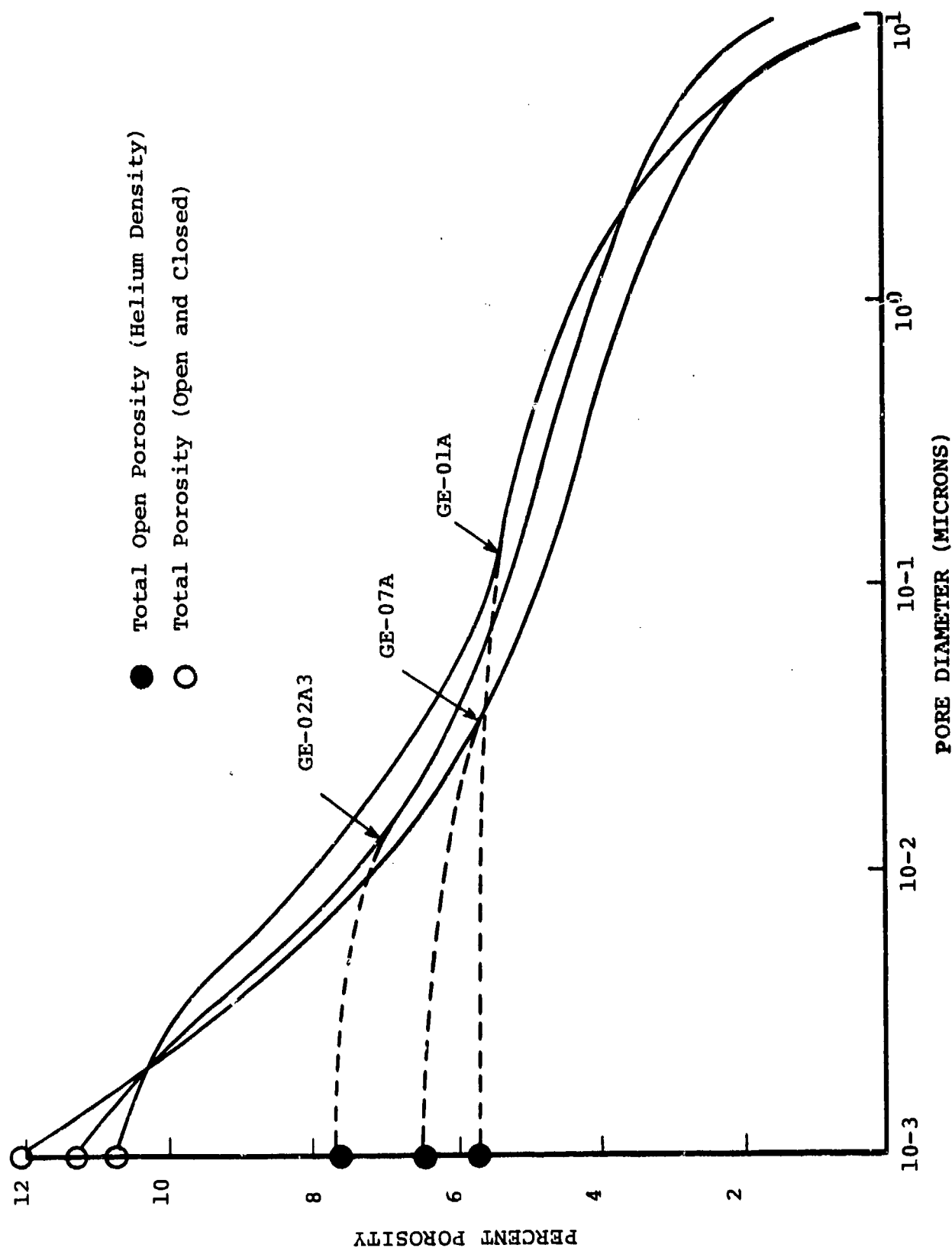


Figure 8. POROSITY DISTRIBUTION FOR 223 T-50 MATERIALS

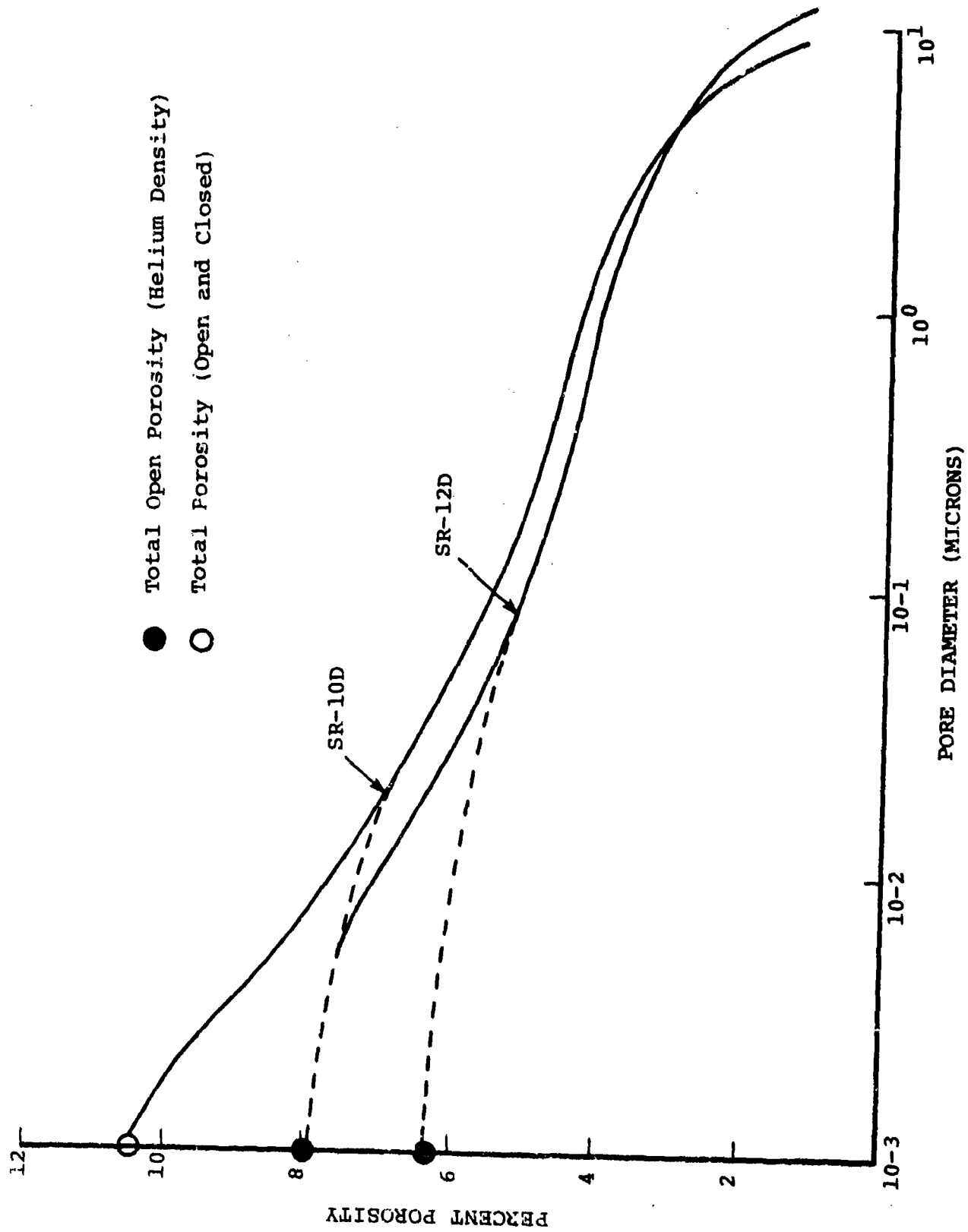


Figure 9. POROSITY DISTRIBUTION FOR 223 PAN MATERIALS

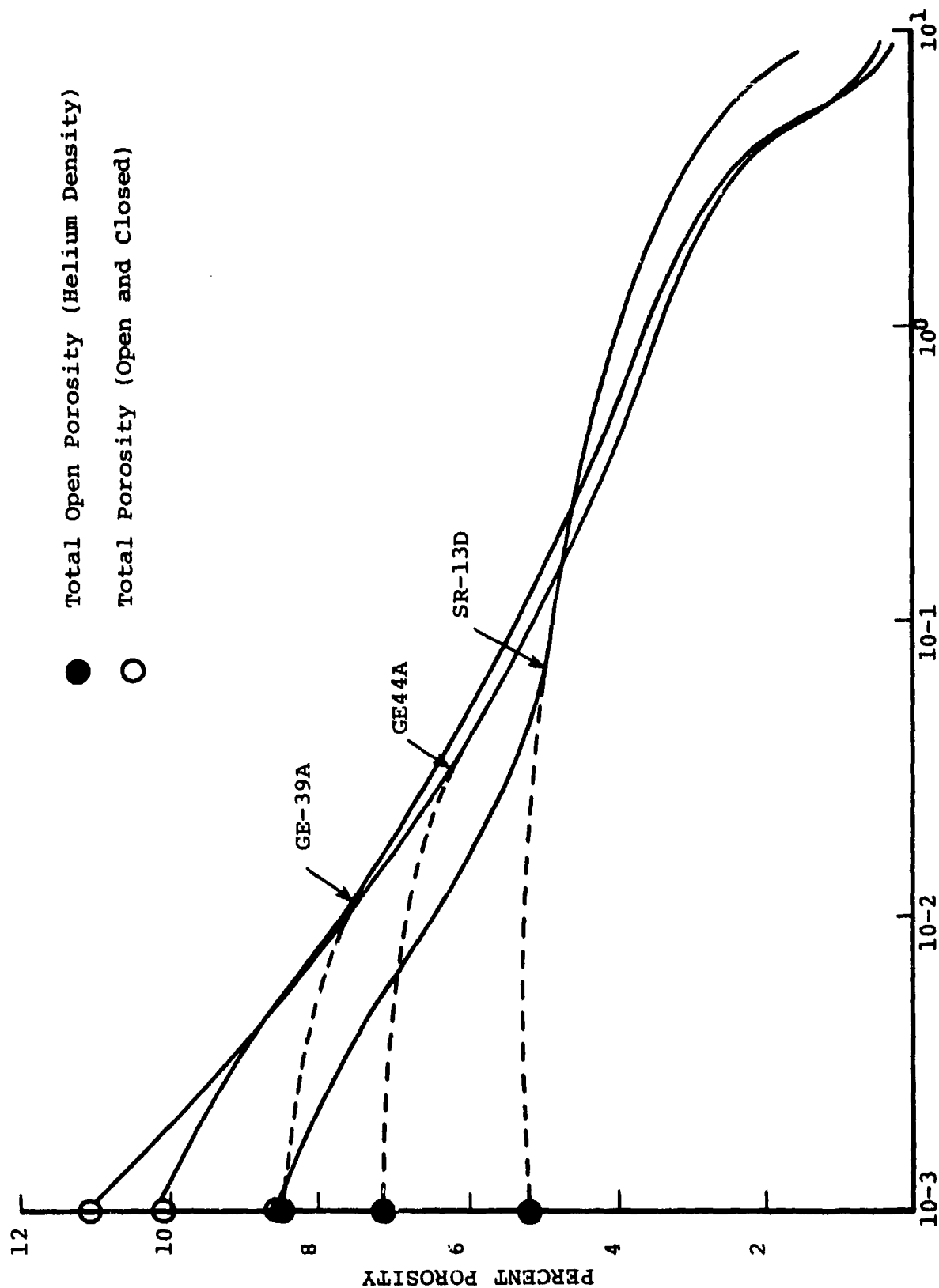


Figure 10. POROSITY DISTRIBUTION FOR 223 PAN, CVD MATERIALS

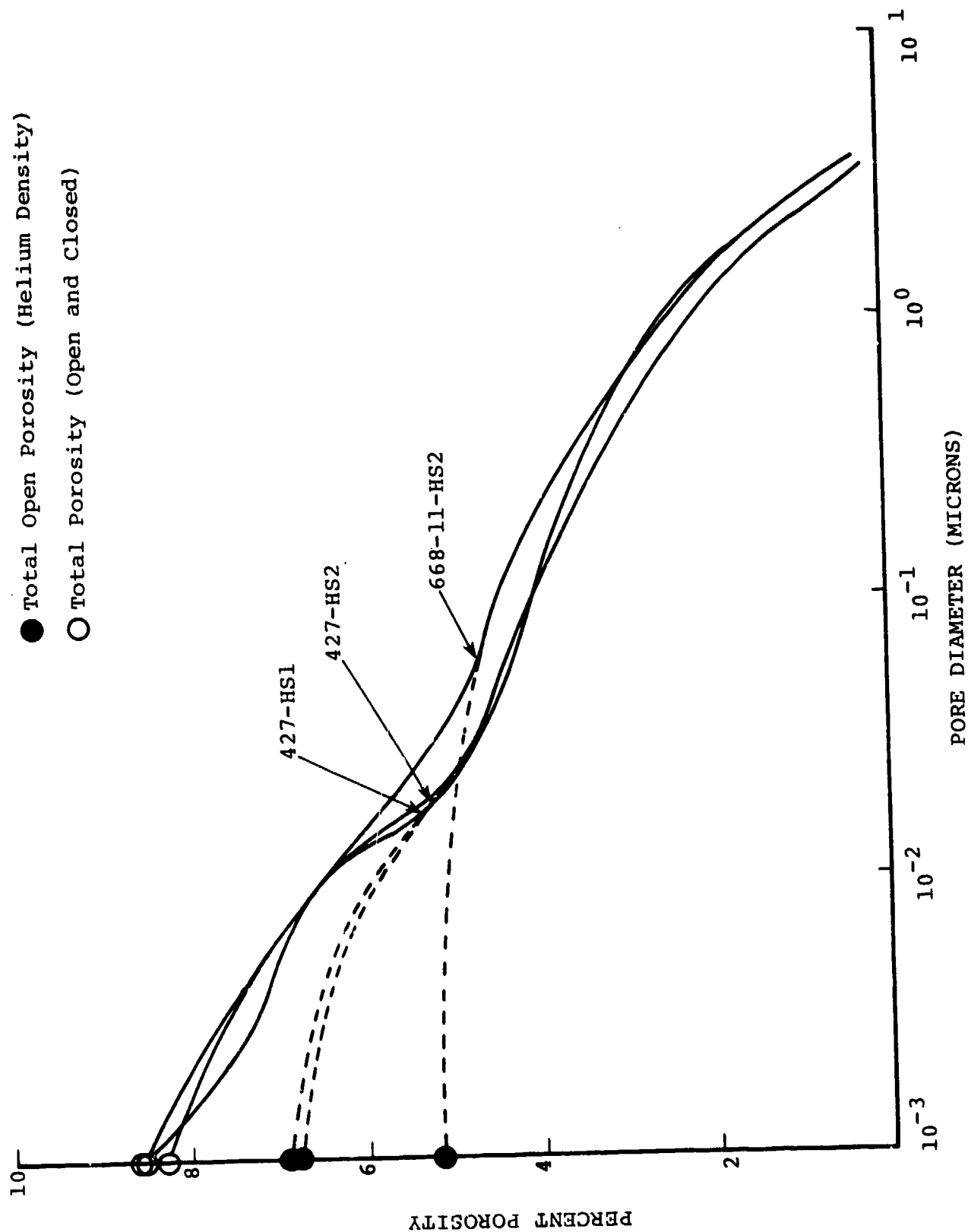


Figure 11. POROSITY DISTRIBUTION FOR 223 PAN, CVD MATERIALS

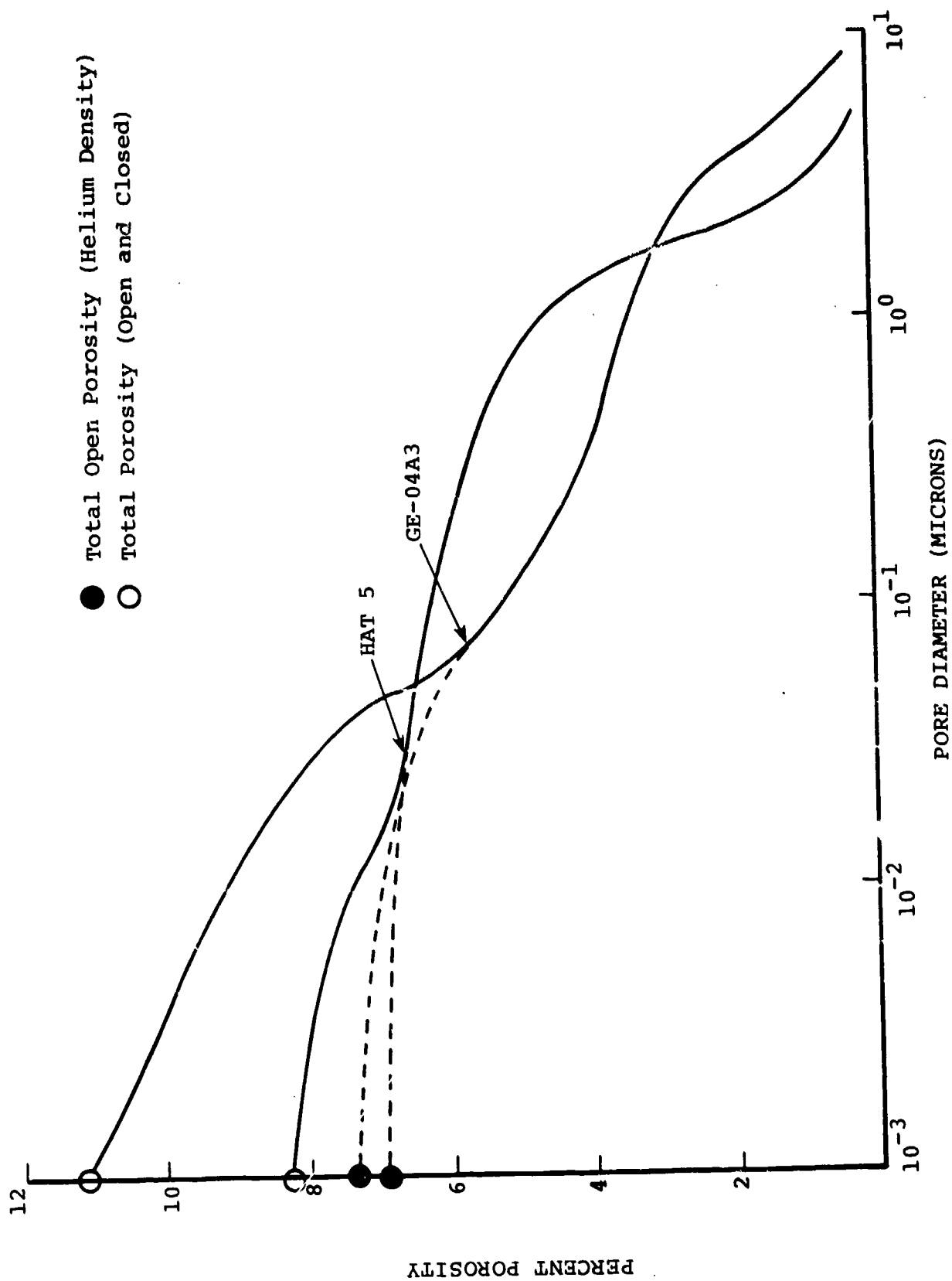


Figure 12. POROSITY DISTRIBUTION FOR 223 PAN, HAT MATERIAL

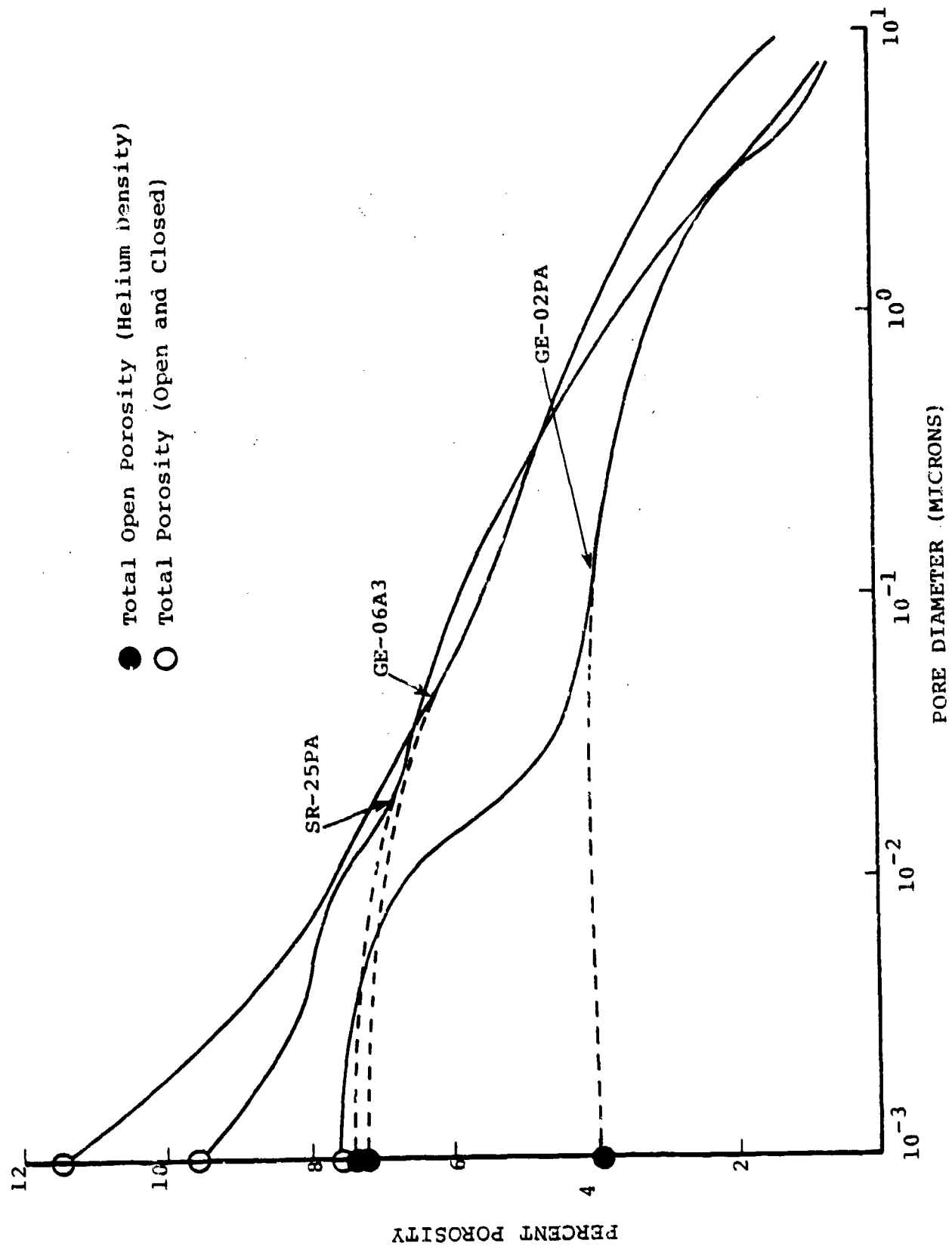


Figure 13. POROSITY DISTRIBUTION FOR FWPF PAN MATERIALS

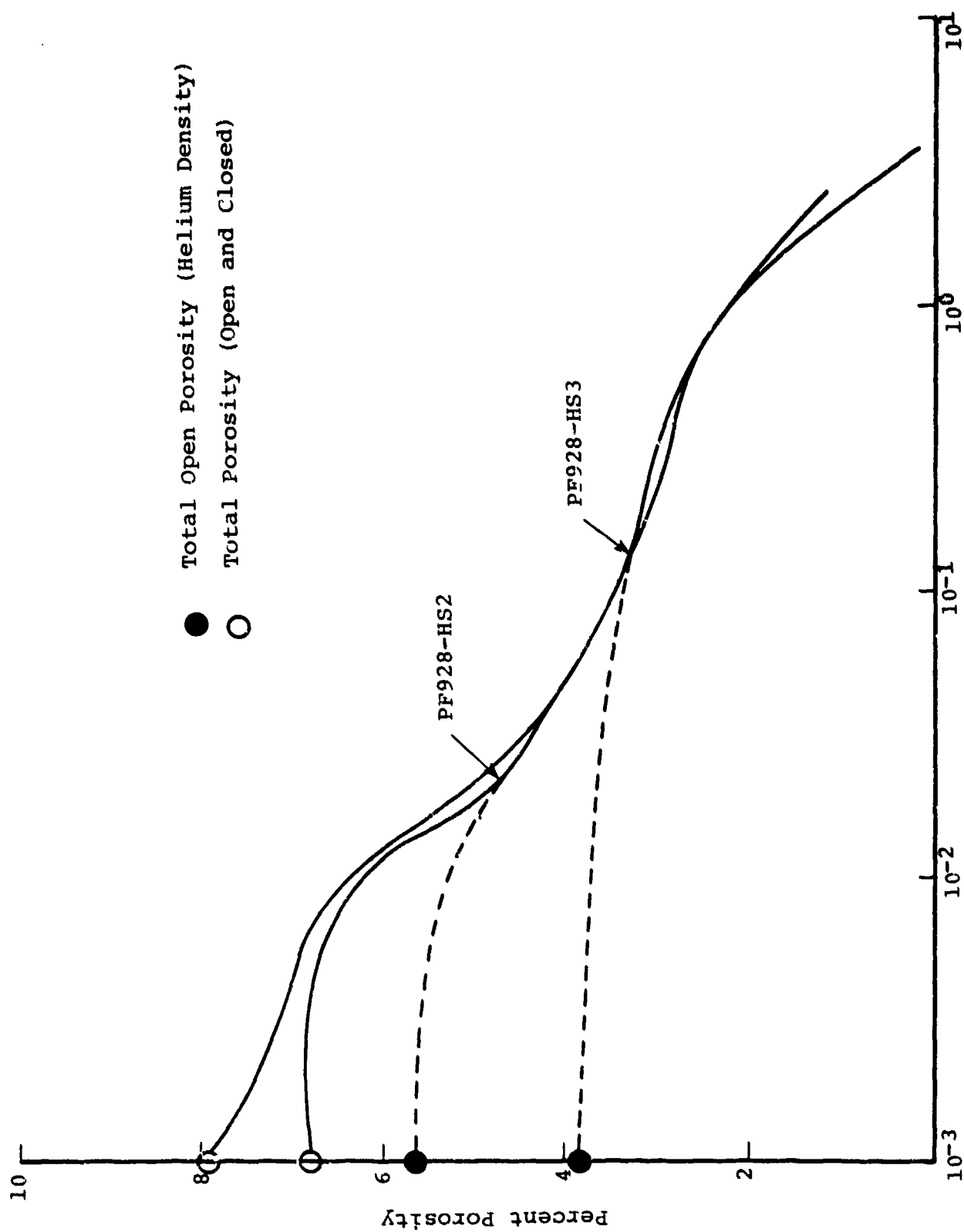


Figure 14. POROSITY DISTRIBUTION FOR FWPF PAN MATERIALS

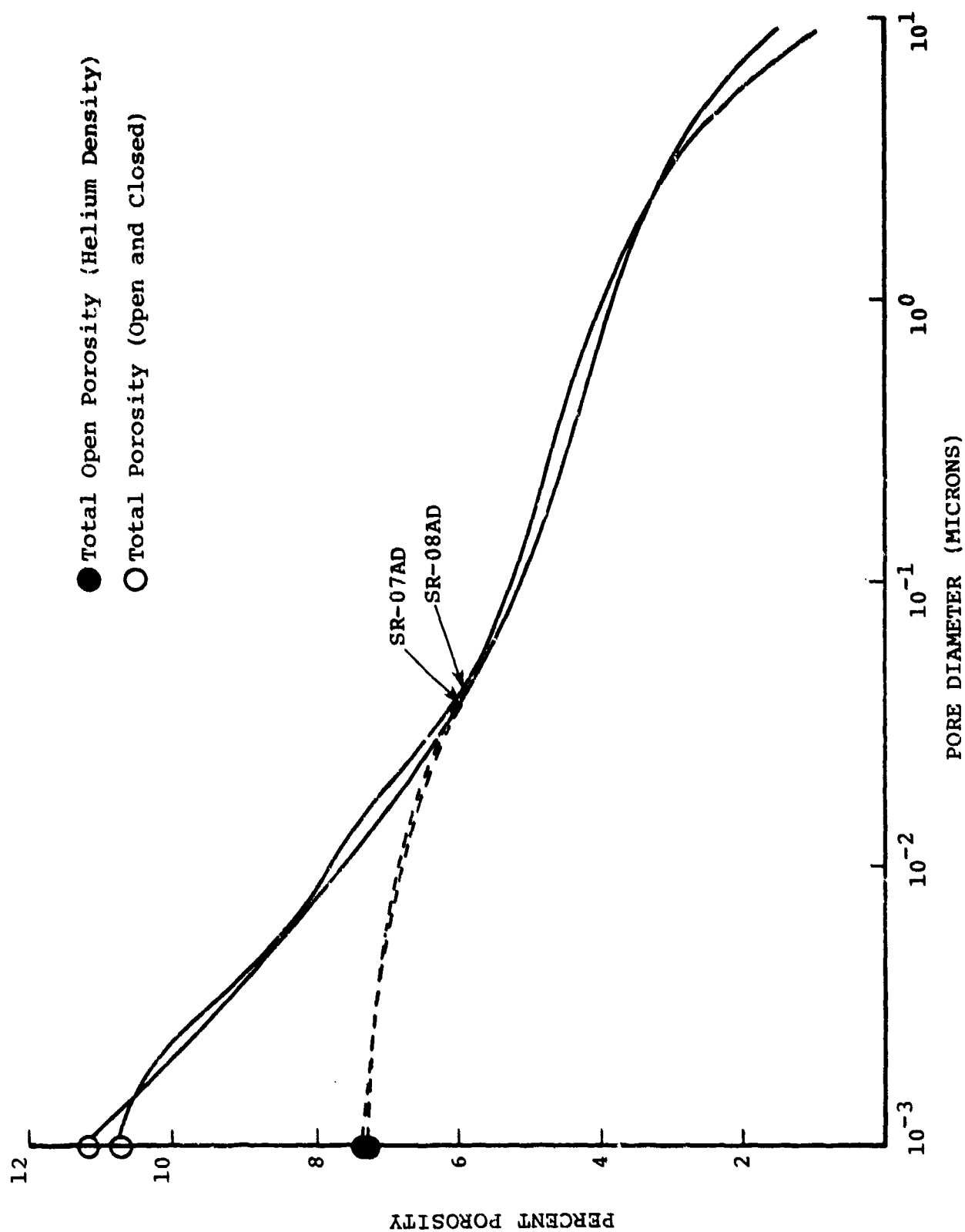
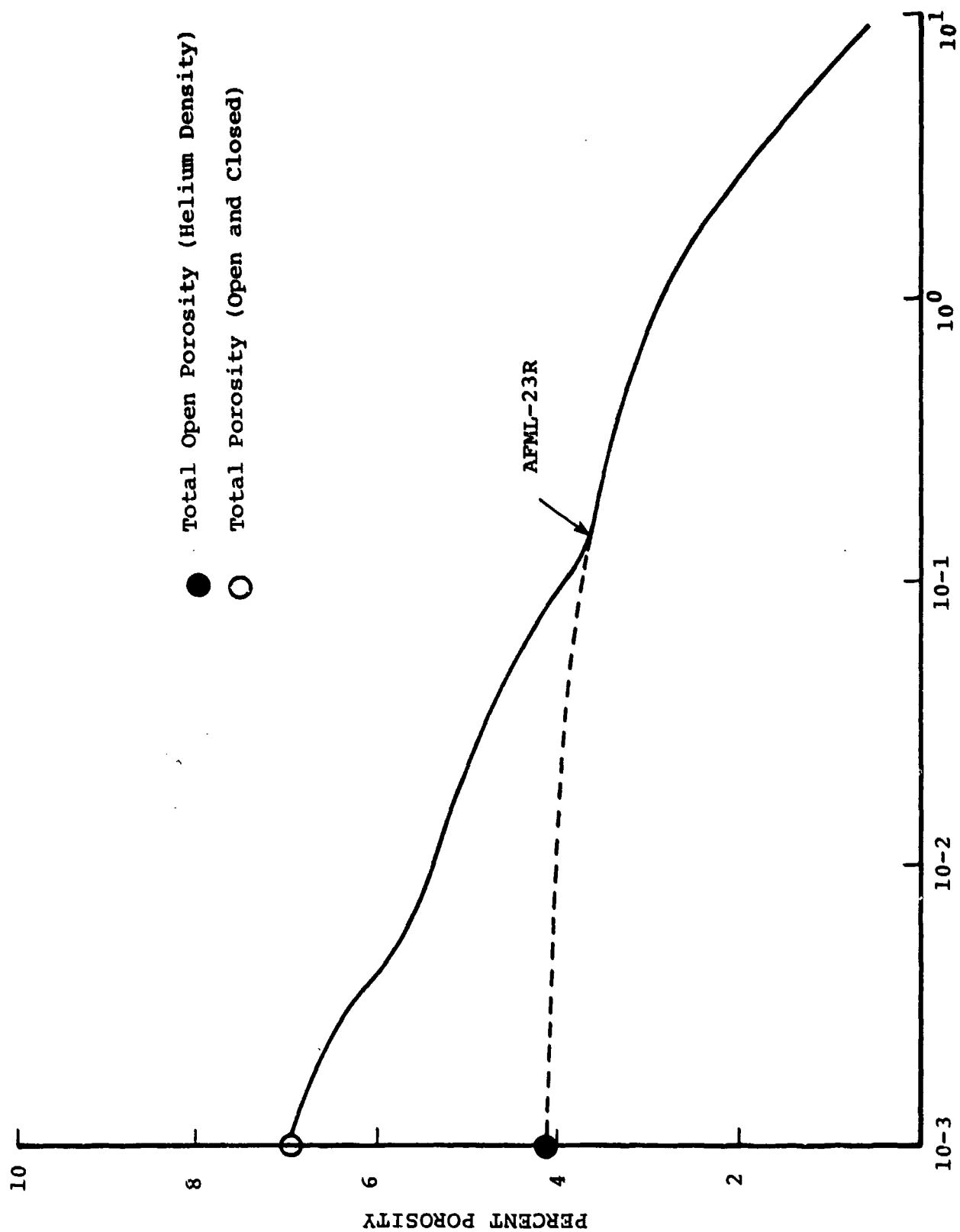


Figure 15. POROSITY DISTRIBUTION FOR PITCH MATERIALS
(Model SR-07AD without CVD, Model SR-08AD with CVD)



PORE DIAMETER (MICRONS)

Figure 16. POROSITY DISTRIBUTION FOR FWPF, LOPIC PROCESSED MATERIAL

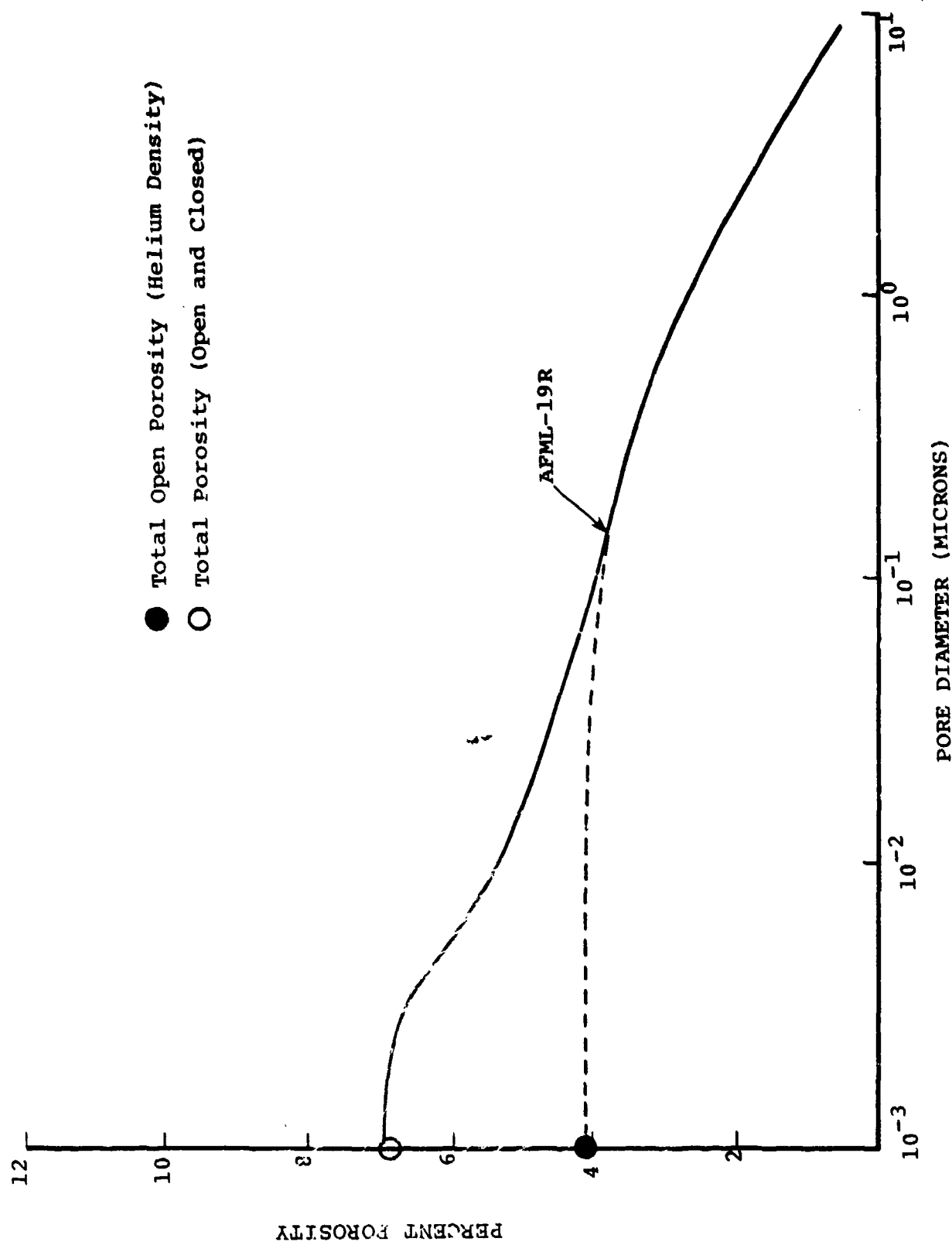


Figure 17. POROSITY DISTRIBUTION FOR JELLYROLL MATERIAL

The bulk density (ρ_o) and helium density (ρ_{He}) were calculated as follows:

$$\rho_o = \frac{m}{V_o} = \text{bulk density}$$

and

$$\rho_{He} = \frac{m}{V_{He}} = \text{helium density}$$

where

m = mass

V_o = bulk volume

V_{He} = volume of helium gas displaced by a specimen.

These measurements were used to calculate the open porosity (ϵ_o) where

$$\epsilon_o = \frac{V_o - V_{He}}{V_o} = 1 - \frac{V_{He}}{V_o} = 1 - \frac{\rho_o}{\rho_{He}}$$

Closed porosity (ϵ_c) was obtained similarly by:

$$\epsilon_c = \frac{V_{He} - V_f}{V_{He}} = 1 - \frac{V_f}{V_{He}} = 1 - \frac{\rho_{He}}{\rho_f}$$

where the subscript f denotes measurements taken on a specimen immersed in mercury at a hydrostatic pressure of 60,000 psi.

Optically measured porosity (ϵ_{opt}) was determined from measurements made on photomicrographs and, since this measurement is restricted to one plane, can be influenced by local variations. These variations, such as an isolated large crack in a Z yarn, were included in the calculated optical porosity values since adjustment for their frequency would require considerably more data than the sections examined. However, where

their influence is large enough for the optical values to exceed those obtained using mercury porosimetry, an indication of variability inherent in the material is suggested.

The permeability test yields the viscous and inertial resistance coefficients α and β respectively using:

$$\frac{\Delta(P^2)}{2 L R T \mu \dot{m}} = \alpha + \beta \frac{\dot{m}}{\mu}$$

where μ and T are the viscosity and temperature of the gas, R is the gas constant, L is the sample thickness, \dot{m} is the flow rate and $\Delta(P^2)$ is the difference in the squares of the upstream and downstream pressures.

Microstructural properties governing molecular permeability (B) and tortuosity (τ^2) were then calculated using the relations:

$$B = 0.2 \epsilon_0 D_M / \tau^2$$

$$\tau^2 = \alpha \epsilon_0 D_V^2 / 16$$

where

D_M = molecular mean pore diameter

D_V = viscous mean pore diameter

D_M and D_V were calculated from the porosity data using a correlation due to Wiggs (Reference 3).

$$\int_0^{\infty} \frac{D^2 - D_V^2}{D^2 + 2 D_V^2} dv_\alpha = 0$$

$$\int_0^{\infty} \frac{D - D_M}{D + 2 D_M} dv_{\alpha} = 0$$

The open internal surface area, S_{α} , was obtained by measuring krypton adsorption as a function of pressure and reducing the data using the BET method (Reference 1). This information, when coupled with permeability considerations, may be of use in modeling efforts to define the relative accessibility of internal surfaces for thermochemical reaction.

2.2.3 Microroughness Measurements - Microroughness measurements for the ablation models are presented in Table 5. These measurements are separated into four groups, the composite (as a system) and the individual components -- Z yarns, transverse yarns, and matrix pockets. The technique for making these measurements has been discussed in Section 2.1.1.

For the composite, values of the average roughness height, $(h)_{av}$, and the median roughness height, $(h)_m$, are shown. The average roughness height for the composite is a weighted average of the three components. Also in Table 5 are the values for the average and median roughness heights for each component along with its second statistical moment.

Statistical moments are used to describe the statistical nature of the roughness height distribution. For each value of the average roughness height, approximately fifty discrete measurements were taken. The average of these individual measurements is the first statistical moment. The second statistical moment, $E [(h-\mu)^2]$, is the variance of the distribution and the square root of the variance is the standard deviation.

These roughness height distributions, in the form of cumulative histograms, are presented in Figures 18 to 38. Each

figure compares the Z yarn contribution to the composite roughness height. This comparison illustrated the dominant behavior of the Z yarn in microroughness measurements.

A summary of the headings on Table 5 are as follows:

$(h)_{av}$	= Average roughness height for composite
$(h)_m$	= Median roughness height for composite
$[(h)_{av}]_z$	= Average roughness height for z-yarn
$[(h)_m]_z$	= Median roughness height for z-yarn
$E[(h)-\mu]^2$	= Second statistical moment for z-yarn roughness height (Variance)
$[(h)_{av}]_{xy}$	= Average roughness height for transverse yarn
$[(h)_m]_{xy}$	= Median roughness height for transverse yarn
$E[(h)-\mu]^2$	= Second statistical moment for transverse yarn roughness height (Variance)
$[(h)_{av}]_M$	= Average roughness height of matrix
$[(h)_m]_M$	= Median roughness height of matrix
$E[(h)-\mu]^2$	= Second statistical moment for matrix roughness height (Variance)

2.2.4 Macroroughness Measurements - The macroroughness measurements as described in Section 2.1.1, are presented in Table 6. The measurements include a complete statistical description of the roughness height (as explained in Section 2.2.3), i.e., average roughness height, median roughness height, and the second, third, and fourth statistical moments. To provide physical insight of these roughness heights, Figures 39 to 60 illustrate the macroroughness height distributions (in the form of cumulative histograms). Also included are the measured

Table 5 MICROROUGHNESS MEASUREMENTS

MODEL	MATERIAL	CONDITION	COMPOSITES			Z YARNS			TRANSVERSE YARNS				MATRIX	
			(Ray MILS)	(Rm MILS)	(h)av/z (MILS)	(h)av/z (MILS)	E((h-z) ²) (MILS) ²	E((h-z) ²) (MILS) ²	(h)av/xy (MILS)	(h)av/xy (MILS)	E((h-z) ²) (MILS) ²	(h)av/z (MILS)	(h)av/z (MILS)	E((h-z) ²) (MILS) ²
AFML-23R	FWPF (LOPIC)	Laminar	0.334	0.301	0.765	0.610	0.196	0.196	0.173	0.148	0.0085	0.328	0.207	0.094
GE-01A	GE-223 (T-50)	Laminar	0.163	0.233	0.297	0.197	0.013	0.013	0.148	0.118	0.0067	0.315	0.177	0.102
GE-02A3	223 (T-50, MDAC)	Laminar	0.321	0.408	0.415	0.394	0.059	0.059	0.169	0.148	0.0056	0.264	0.142	0.052
GE-04A3	223 (PAN, HAT)	Turbulent	0.451	0.574	0.982	1.063	0.220	0.220	0.151	0.148	0.0028	0.975	1.201	0.345
GE-06A3	FWPF (PAN)	Laminar	1.026	1.306	2.023	2.087	0.519	0.519	0.213	0.207	0.0040	0.469	0.394	0.103
SR-07AD	FMI (PITCH)	Laminar	0.248	0.316	0.456	0.354	0.101	0.101	0.152	0.118	0.0088	0.258	0.197	0.026
SR-08AD	FMI (PITCH, CVD)	Laminar	0.242	0.308	0.448	0.374	0.114	0.114	0.169	0.118	0.0095	0.222	0.177	0.023
SR-10D	223 (PAN, No CVD)	Laminar	0.990	1.260	1.462	1.491	0.588	0.588	0.198	0.177	0.0064	0.285	0.236	0.041
SR-12D	223 (PAN, No CVD)	Laminar	1.108	1.411	1.703	1.885	1.190	1.190	0.178	0.177	0.0064	0.285	0.236	0.041
SR-13D	223 (PAN, CVD)	Laminar	1.235	1.573	1.698	1.905	0.317	0.317	0.189	0.148	0.0119	0.459	0.394	0.134
GE-07A	223 (T-50)	Turbulent	0.217	0.315	0.253	0.217	0.015	0.015	0.151	0.148	0.0022	0.913	0.768	0.389
GE-39A	223 (PAN)	Laminar	0.240	0.306	0.392	0.295	0.068	0.068	0.126	0.098	0.0032	0.198	0.148	0.024
GE-44A	223 (PAN)	Laminar	0.374	0.476	0.590	0.472	0.161	0.161	0.196	0.165	0.016	0.348	0.268	0.075
GE-02PA	FWPF (PAN)	Laminar	1.114	1.063	1.447	1.396	0.408	0.408	0.149	0.126	0.00264	0.313	0.252	0.0465
SR-25PA	FWPF (PAN, LoPIC)	Laminar	0.734	0.788	0.888	0.981	0.141	0.141	0.202	0.189	0.00809	0.555	0.421	0.114
HAT 5	223 (PAN, HAT)	Turbulent	1.426	1.450	1.734	1.774	0.627	0.627	0.229	0.226	0.00780	0.923	0.799	0.359
427-HS1	223 (PAN, CVD)	Laminar	0.398	0.389	0.491	0.483	0.0434	0.0434	0.209	0.211	0.00854	1.075	0.631	0.864
427-HS2	223 (PAN, CVD)	Laminar	0.460	0.487	0.808	0.854	0.0565	0.0565	0.228	0.248	0.00837	0.345	0.272	0.0338
PF928-HS2	FWPF (PAN)	Laminar	0.681	0.688	0.865	0.867	0.0644	0.0644	0.215	0.223	0.00481	0.809	0.879	0.246
PF928-HS3	FWPF (PAN)	Laminar	0.440	0.438	0.493	0.487	0.0307	0.0307	0.176	0.177	0.00345	0.223	0.197	0.0119
668-11-HS2	223 (PAN, CVD)	Laminar	0.471	0.455	0.636	0.671	0.0748	0.0748	0.204	0.194	0.00511	0.343	0.194	0.148

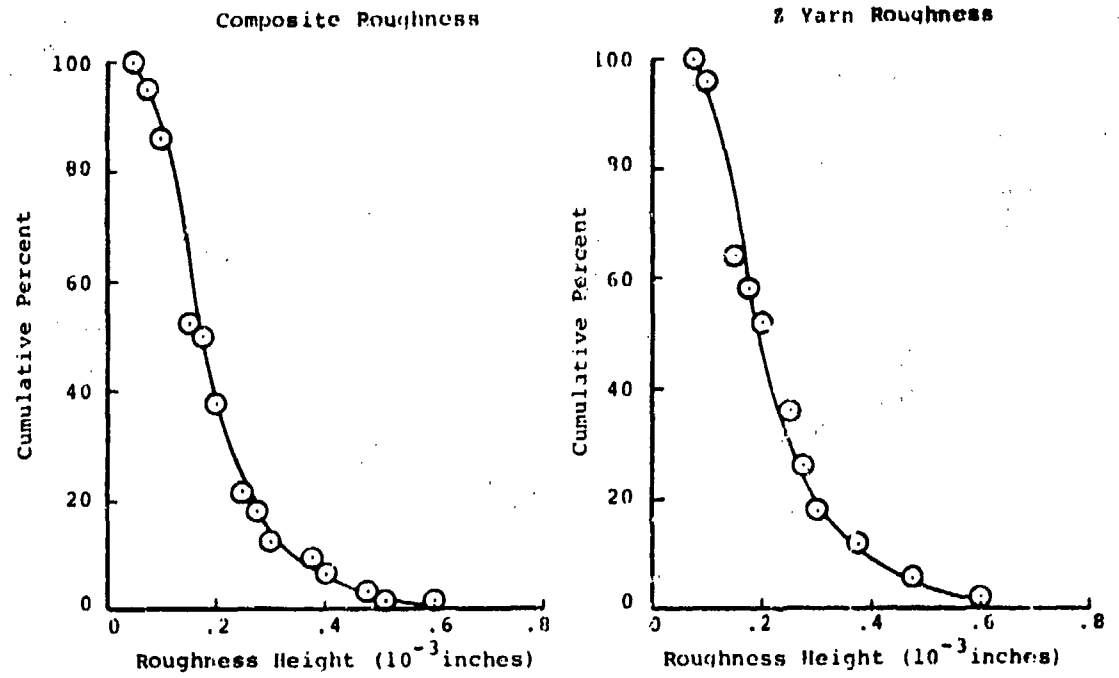


Figure 18 MICROROUGHNESS HEIGHT DISTRIBUTION FOR
GE-01A (GE 223 T-50, Laminar)

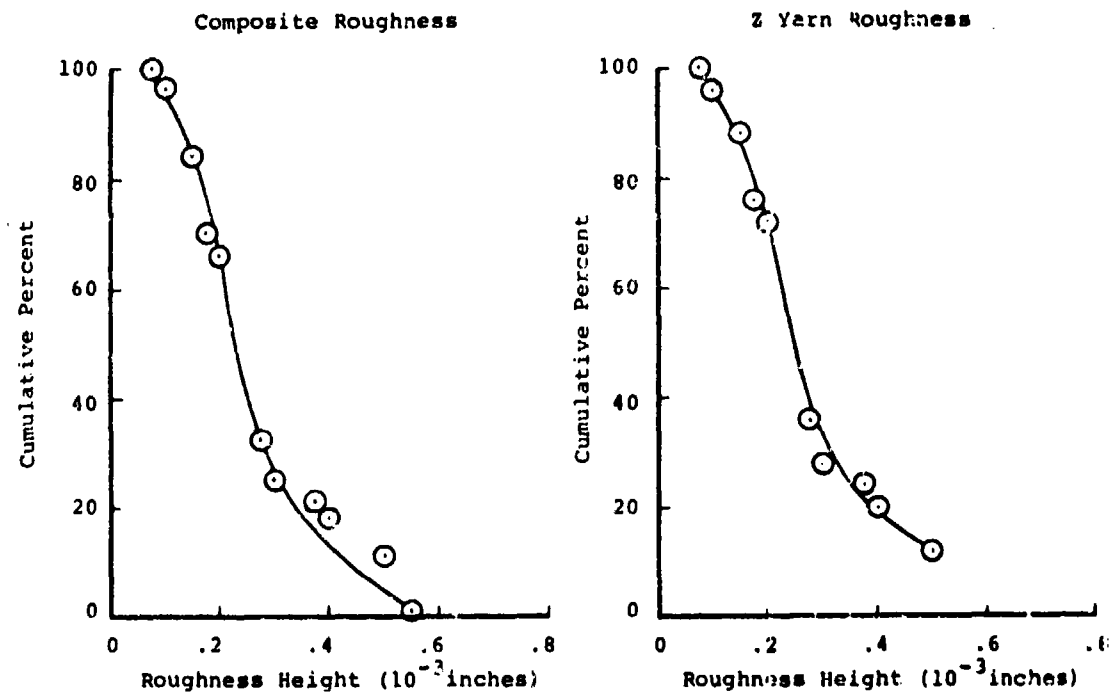


Figure 19 MICROROUGHNESS HEIGHT DISTRIBUTION FOR
GE-07A (223 T-50, Turbulent)

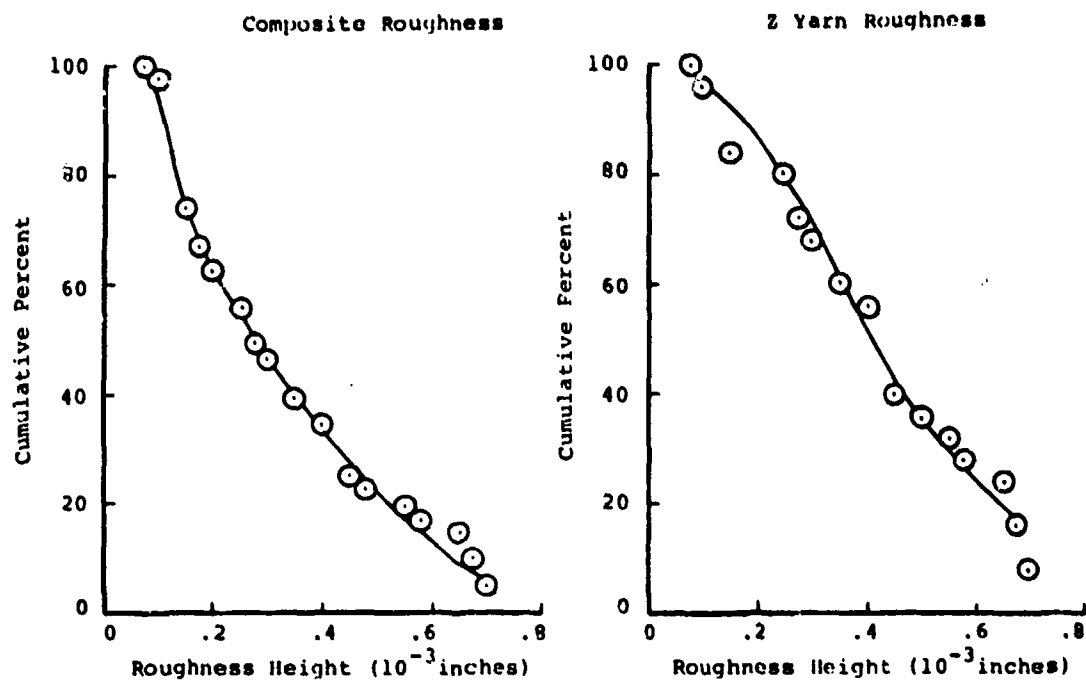


Figure 20 MICROROUGHNESS HEIGHT DISTRIBUTION FOR
GE-02A3 (223 T-50, MDAC, Laminar)

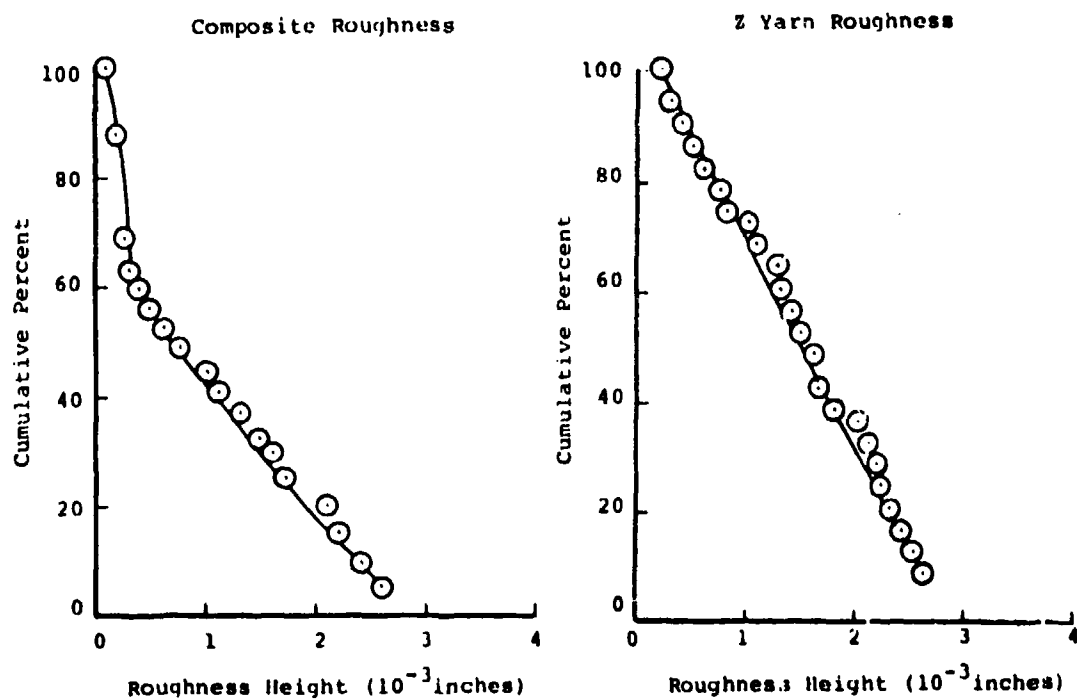


Figure 21 MICROROUGHNESS HEIGHT DISTRIBUTION FOR
SR-10D (223 PAN, No CVD, Laminar)

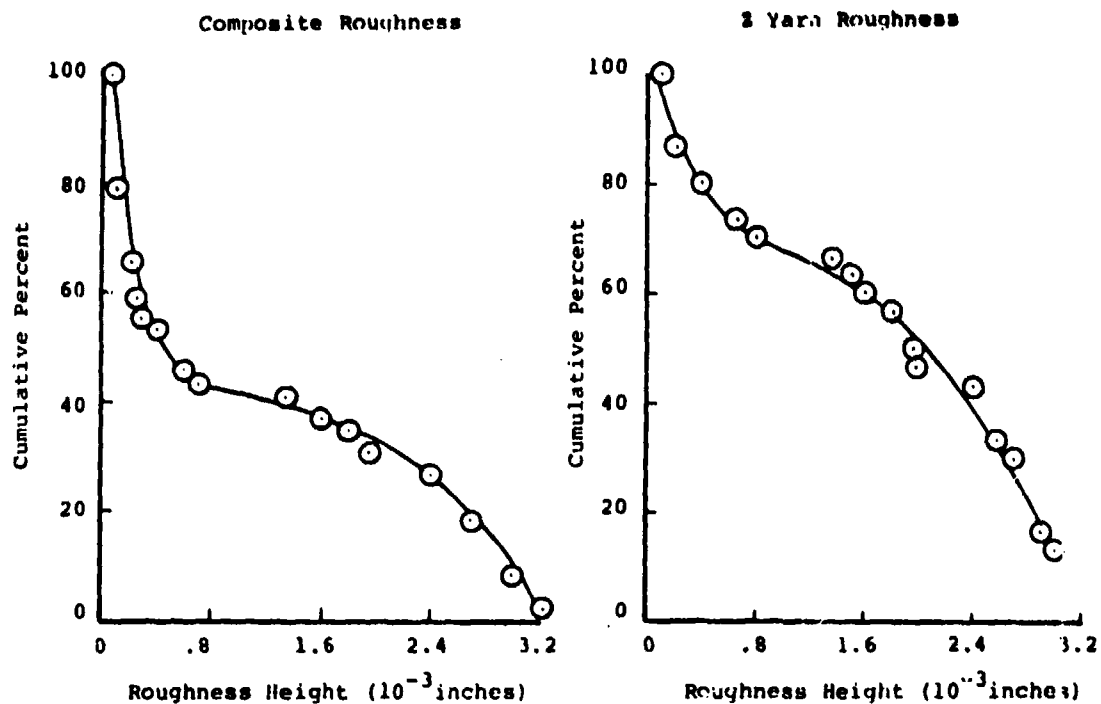


Figure 22 MICROROUGHNESS HEIGHT DISTRIBUTION FOR
SR-12D (223 PAN, No CVD, Initial LoPIC,
Laminar)

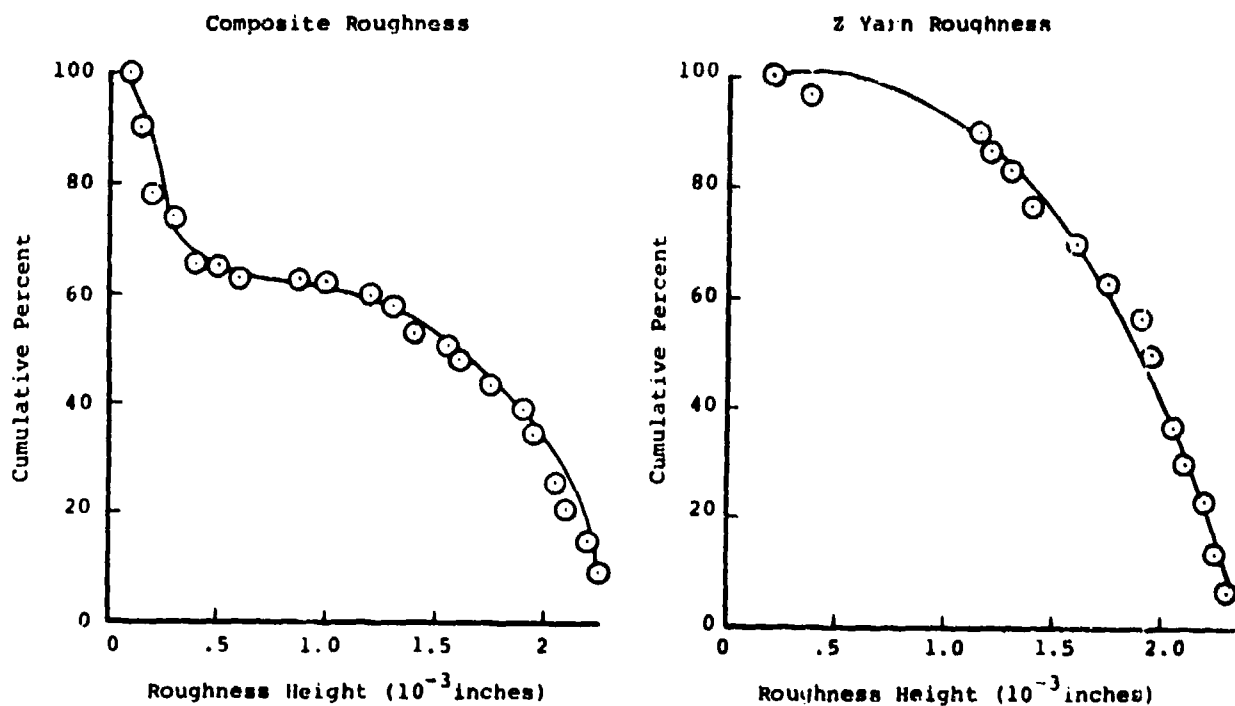


Figure 23 MICROROUGHNESS HEIGHT DISTRIBUTION FOR
SR-13D (223 PAN, CVD, 2300°C Graph, Laminar)

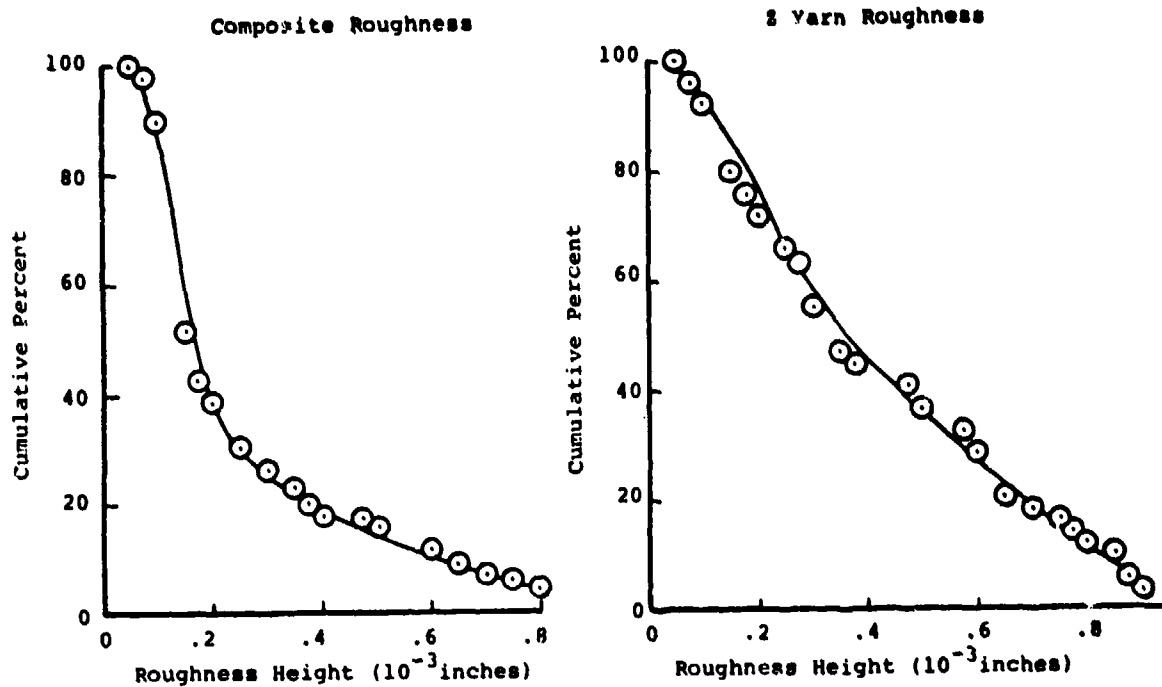


Figure 24 MICROROUGHNESS HEIGHT DISTRIBUTION FOR
GE-39A (223 PAN, CVD, Laminar)

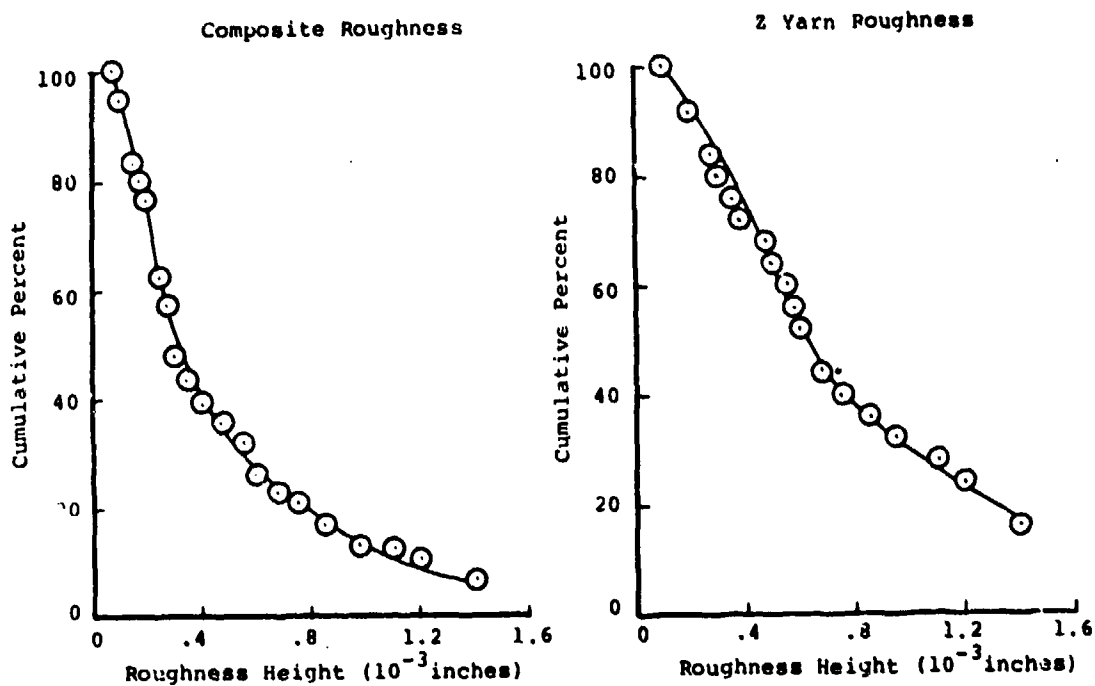


Figure 25 MICROROUGHNESS HEIGHT DISTRIBUTION FOR
GE-44A (223 PAN, CVD, Laminar)

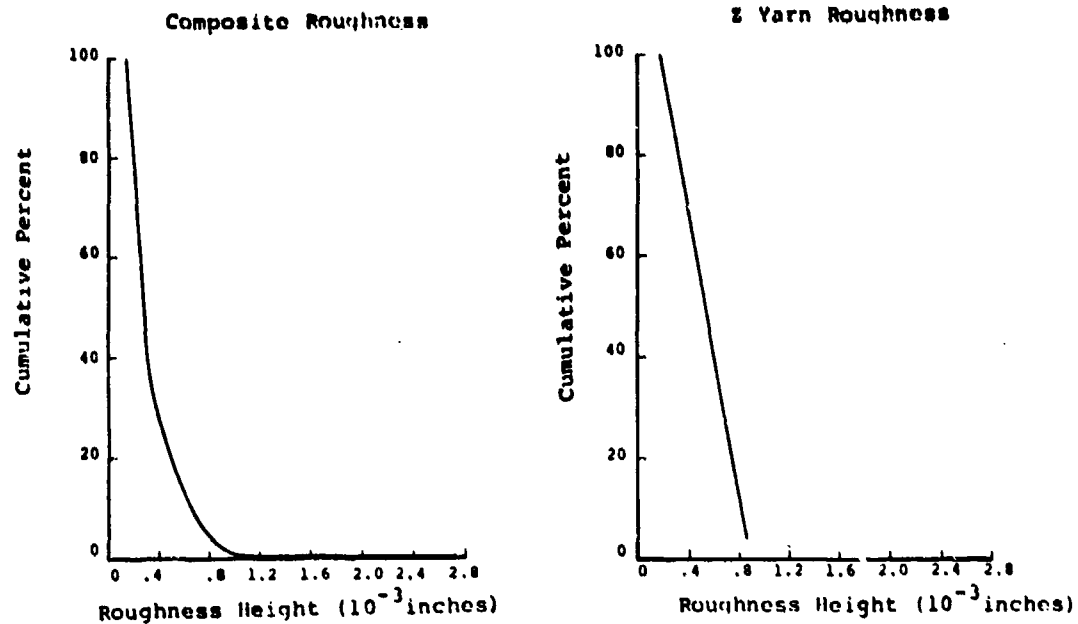


Figure 26 MICROROUGHNESS HEIGHT DISTRIBUTION FOR
427-HS1 (223 PAN, CVD, Laminar)

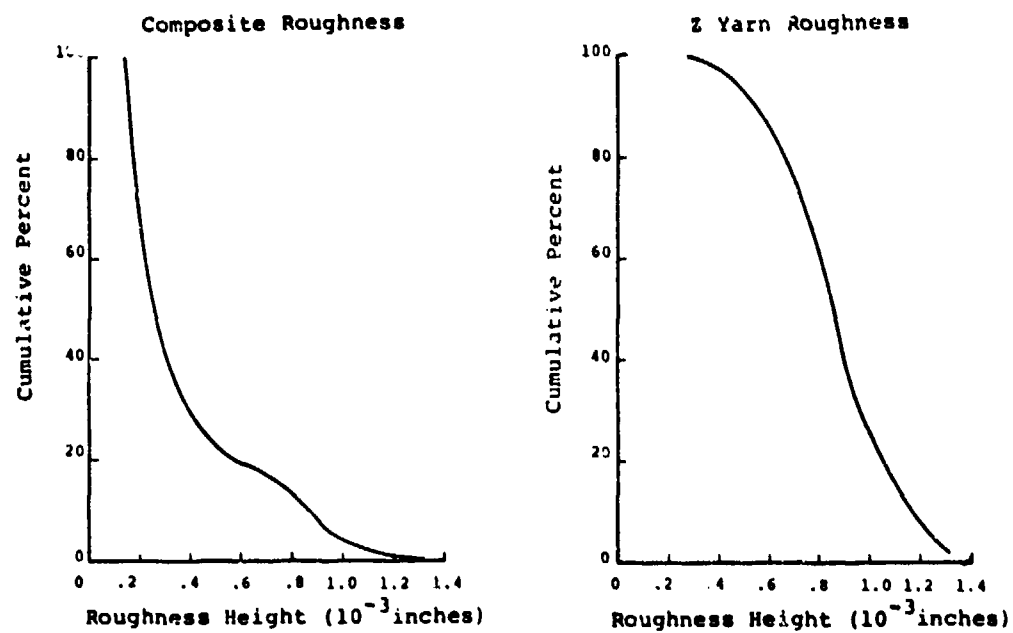


Figure 27 MICROROUGHNESS HEIGHT DISTRIBUTION FOR
427-HS2 (223 PAN, CVD, Laminar)

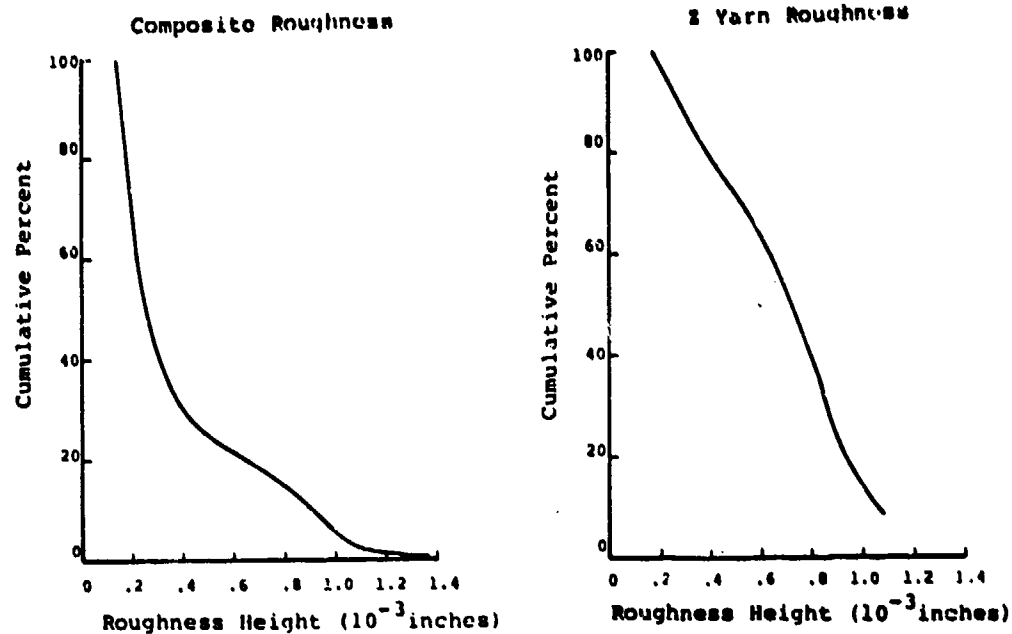


Figure 28 MICROROUGHNESS HEIGHT DISTRIBUTION FOR 668-11-HS2 (223 PAN, CVD, Laminar)

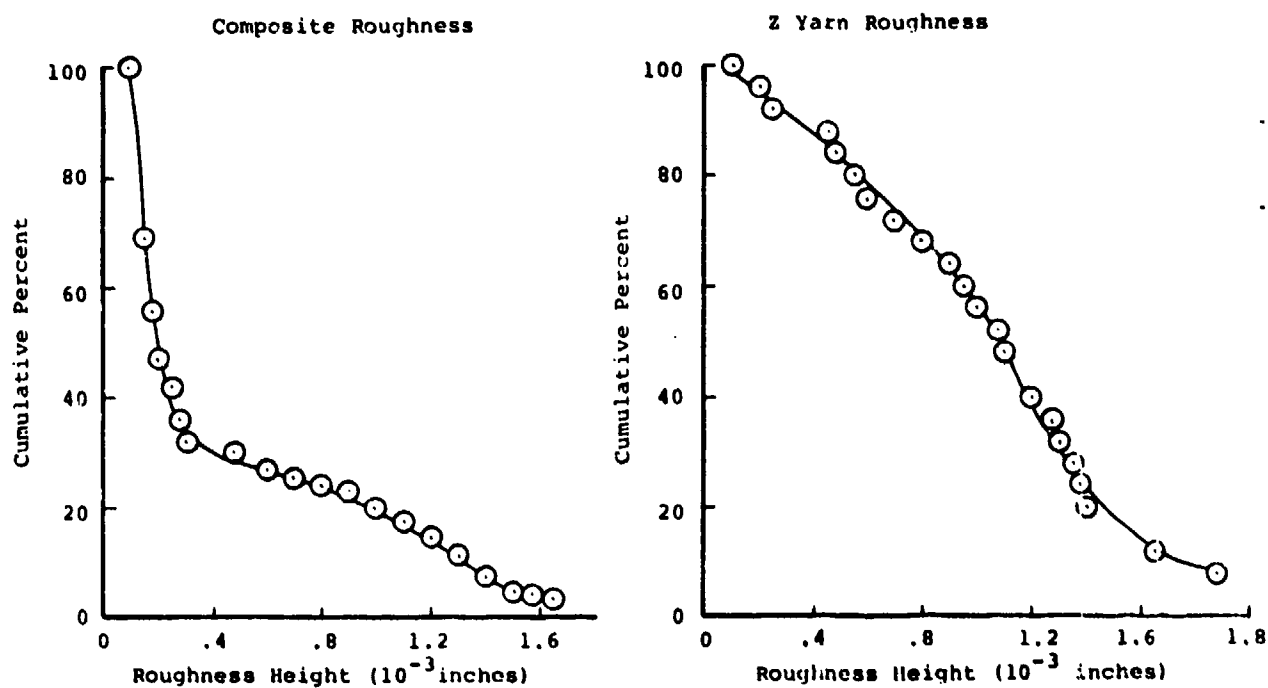


Figure 29 MICROROUGHNESS HEIGHT DISTRIBUTION FOR GE-04A3 (223 PAN, HAT, Turbulent)

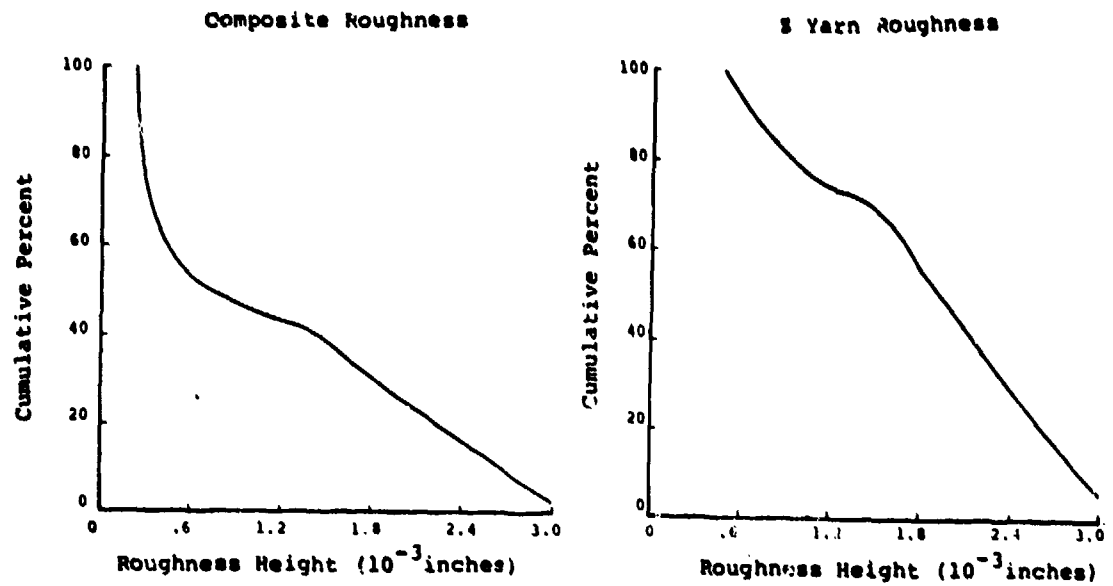


Figure 30 MICROROUGHNESS HEIGHT DIDTRIBUTION FOR
HAT 5 (223 PAN, HAT, Turbulent)

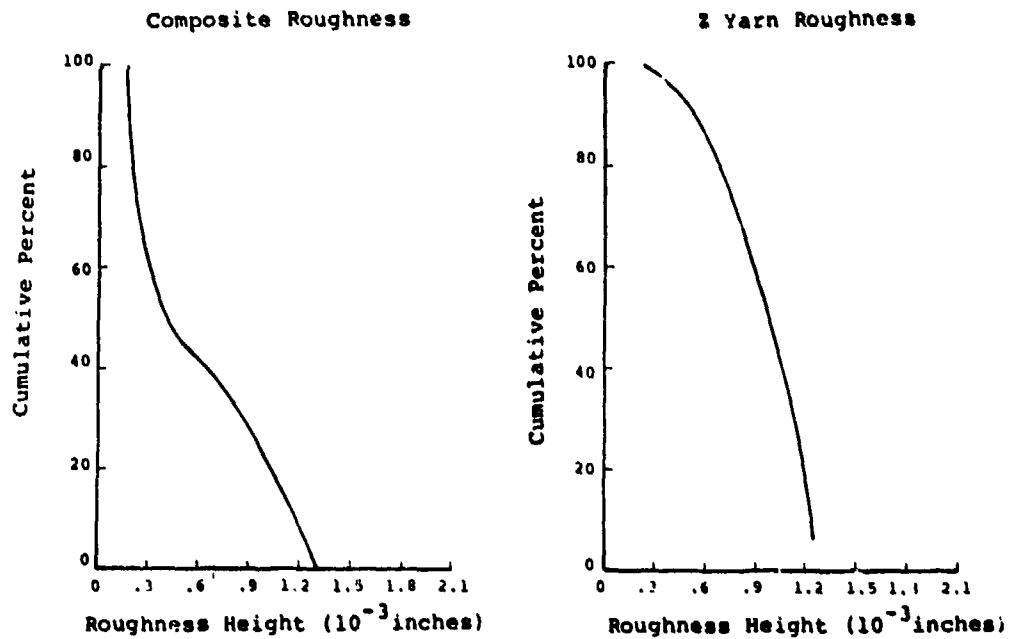


Figure 31 MICROROUGHNESS HEIGHT DISTRIBUTION FOR
PF928-HS2 (FWPF PAN, Laminar)

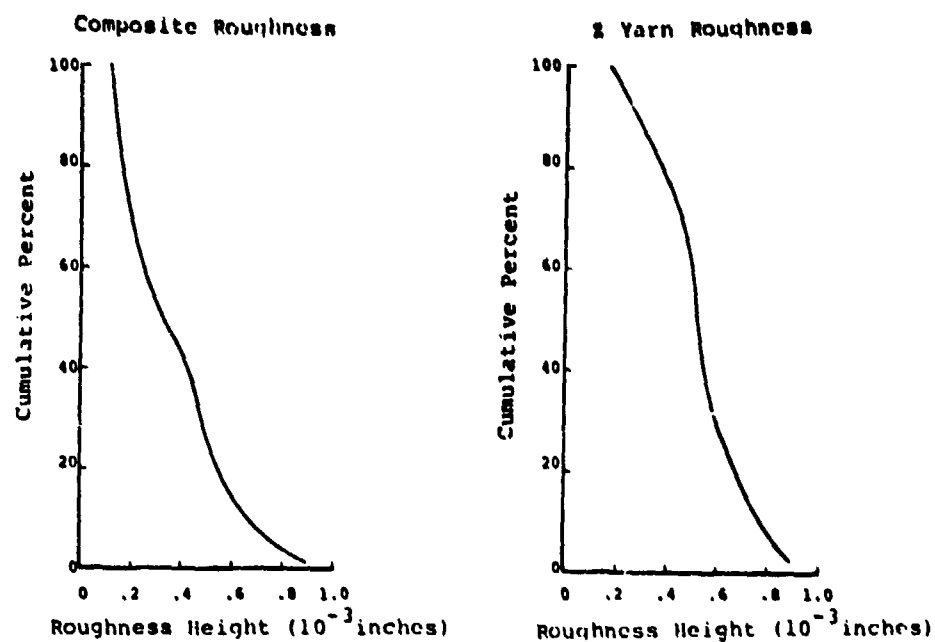


Figure 32 MICROROUGHNESS HEIGHT DISTRIBUTION FOR DF928-HS3 (FWPF PAN, Laminar)

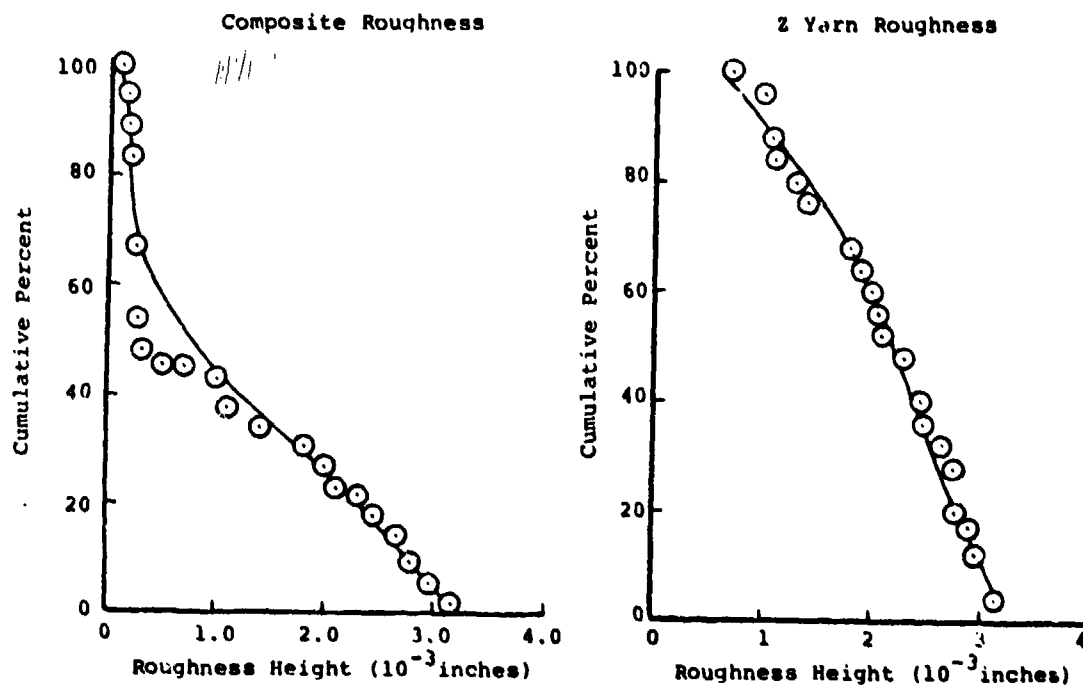


Figure 33 MICROROUGHNESS HEIGHT DISTRIBUTION FOR GE-06A3 (FWPF-PAN, Laminar)

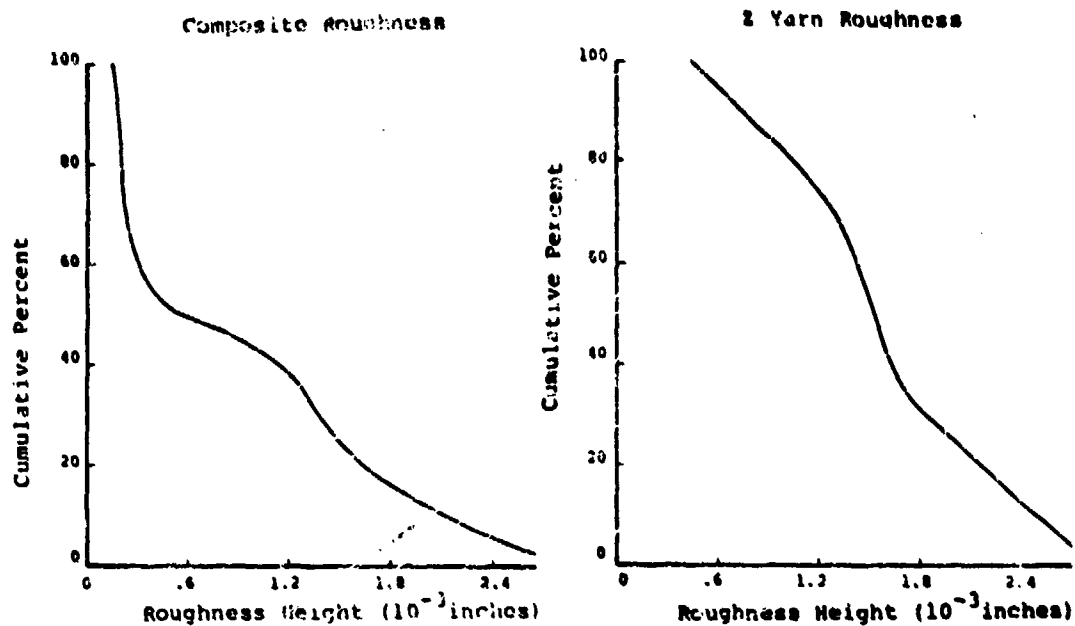


Figure 34 MICROROUGHNESS HEIGHT DISTRIBUTION FOR
GE-02PA (FWPF PAN, Laminar)

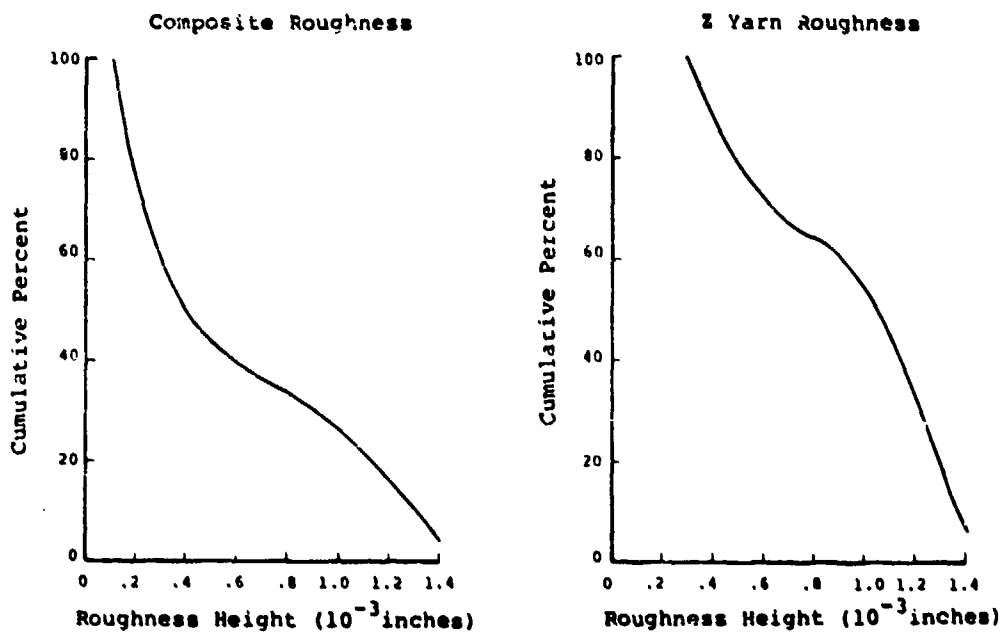


Figure 35 MICROROUGHNESS HEIGHT DISTRIBUTION FOR
SR-25PA (FWPF PAN, LoPIC, Laminar)

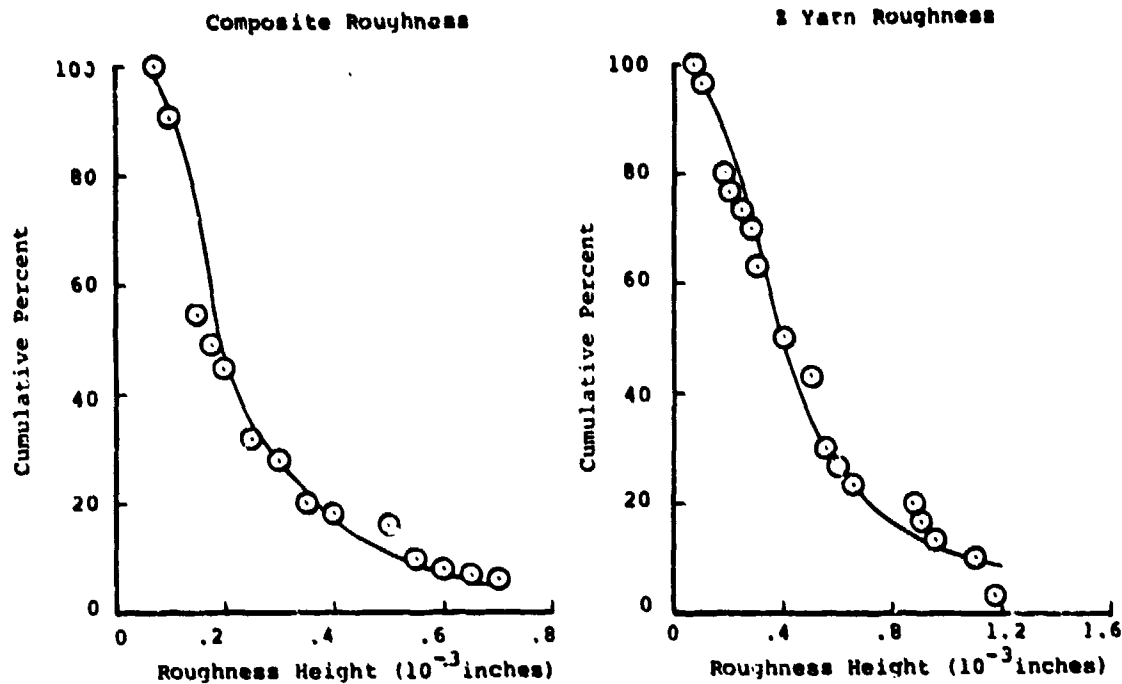


Figure 36 MICROROUGHNESS HEIGHT DISTRIBUTION FOR SR-07AD (Pitch, No CVD, Laminar)

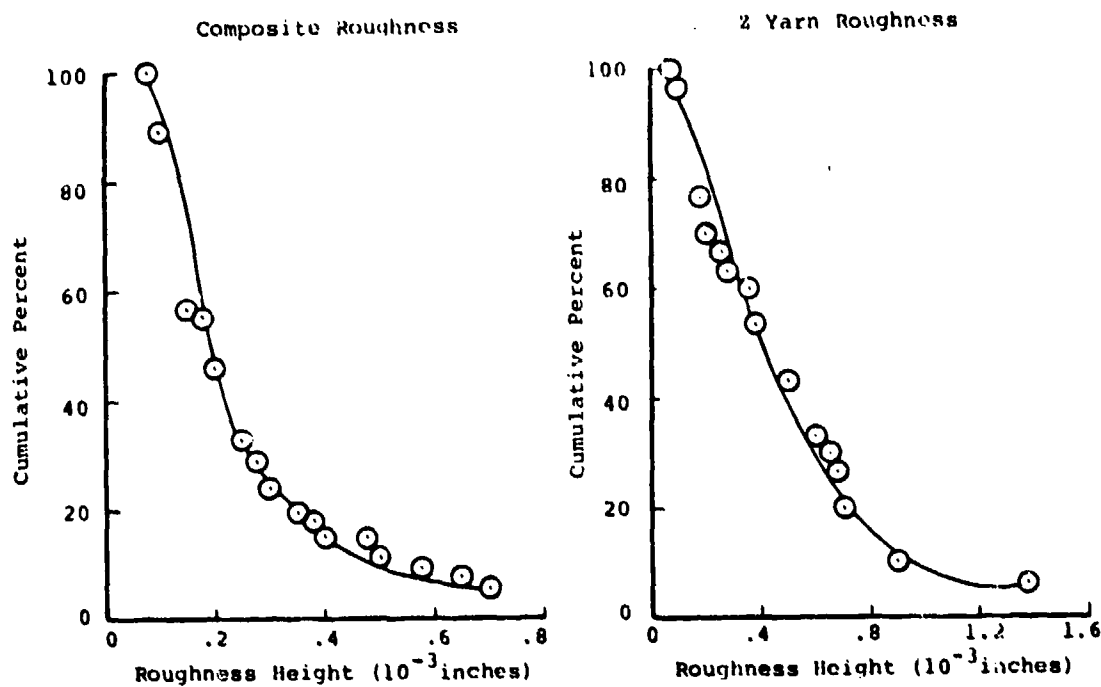


Figure 37 MICROROUGHNESS HEIGHT DISTRIBUTION FOR SR-08AD (Pitch with CVD, Laminar)

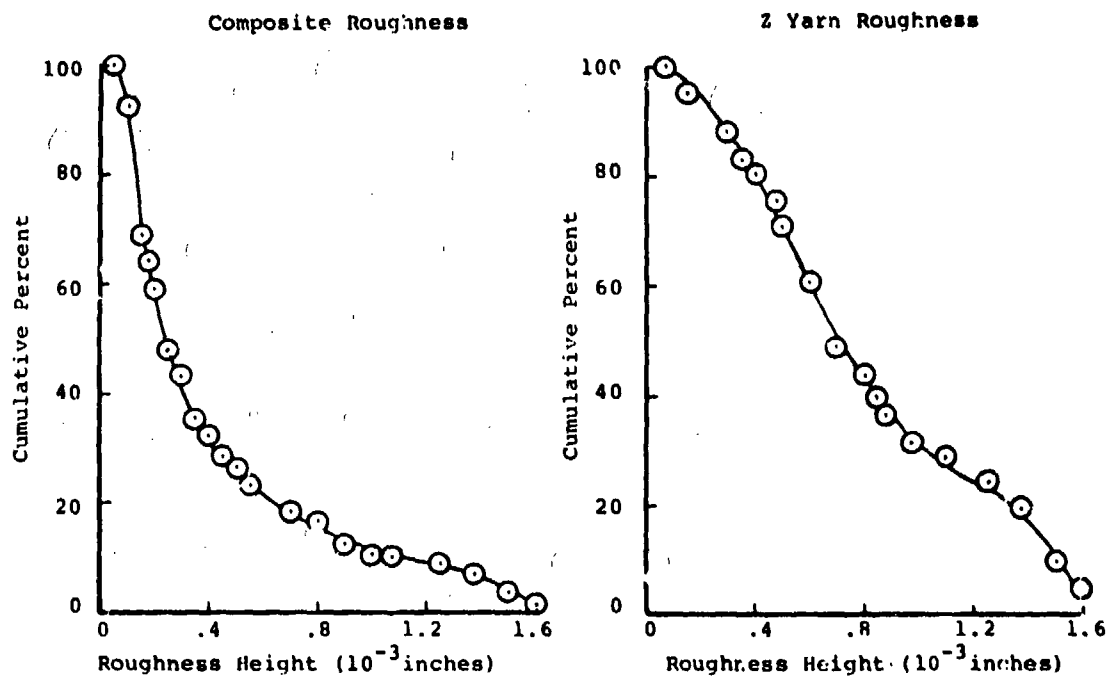


Figure 38 MICROROUGHNESS HEIGHT DISTRIBUTION FOR
AFML-23R (FWPF, LcPIC, Laminar)

values for the average width of the roughness element and the average peak-to-peak spacings between roughness elements.

Two other roughness measurements are presented -- that of adjusted roughness height and equivalent sand roughness height. The adjusted roughness height is given by the formula:

$$(k)_{av} = \frac{4}{\pi} (h)_{av}$$

where, $(h)_{av}$ is the average measured roughness height. The $\frac{4}{\pi}$ factor, from a probabilistic view, accounts for the failure of a plane cross-section to pass through the peak of a hemispherical roughness element. The equivalent sand roughness height is determined from Figure 61, (Reference 4). The equivalent sand roughness height is k_s , where k is the adjusted macroroughness height, (A_p/A_s) is a shape factor given by the ratio of element surface areas projected normal to the flow, A_p and actual windward surface area, A_s (for this case, $A_p/A_s = 0.45$), and the spacing defined as:

$$D = \left[\frac{3\pi}{8} (L_p)_{av} \frac{(w^2)_{av}}{(w)_{av}} \right]^{\frac{1}{2}}$$

where $(L_p)_{av}$ is the average peak-to-peak spacing between roughness elements and $(w)_{av}$ is the average width of a roughness element as shown in Figure 5.

A summary of the data presented in Table 6 is:

$(h)_{av}$	= Average roughness height
$(h)_m$	= Median roughness height
$E[(h-u)^2]$	= Second statistical moment for Macroroughness height (Variance)
$E[(h-u)^3]$	= Third statistical moment for Macroroughness height (Skewness)
$E[(h-u)^4]$	= Fourth statistical moment for Macroroughness height (Peakedness)
$(w)_{av}$	= Average width of roughness element
$(L_p)_{av}$	= Average peak-to-peak spacing between roughness elements
$(k)_{av}$	= Average adjusted roughness height
k_s	= Equivalent sand roughness height

Table 6. MACROROUGHNESS MEASUREMENTS

MODEL	MATERIAL	CONDITION	(h) _{av} (MILS)	(h) _m (MILS)	E(h-m) ² (MILS) ²	E(h-m) ³ (MILS) ³	E(h-m) ⁴ (MILS) ⁴	(w) _{av} (MILS)	(L) _{p av} (MILS)	(K) _{av} (MILS)	K _s (MILS)
AFML-19R	Jellyroll	Laminar	3.892	4.632	2.857	-3.025	16.136	5.10	15.75	4.955	21.34
AFML-23R	FMPF (LoPIC)	Laminar	4.749	4.701	0.479	0.031	0.424	18.09	38.80	6.047	5.089
GE-01A	GE 223 (T-50)	Laminar	6.459	6.581	1.996	-1.575	11.31	10.80	30.05	8.224	28.85
GE-02A3	223 (T-50, MDAC)	Laminar	2.807	2.605	0.460	0.018	0.487	9.767	29.11	3.574	2.898
GE-04A3	223 (PAN, HAT)	Turbulent	2.289	2.316	0.582	0.199	0.734	10.22	25.57	2.914	1.592
CF-06A2	FMPF (PAN)	Laminar	2.148	1.822	1.070	0.412	2.062	8.700	22.35	2.736	1.276
SR-07AD	FMI (Pitch)	Laminar	2.484	2.258	2.093	1.903	9.302	9.069	28.80	3.162	2.071
SR-08AD	FMI (Pitch, CVD)	Laminar	3.382	3.474	1.298	0.849	5.363	10.466	27.60	4.306	4.665
SR-10B	223 (PAN, No CVD)	Laminar	3.902	3.936	0.446	0.039	0.451	9.034	27.07	4.968	8.333
SR-12D	223 (PAN, No CVD)	Laminar	4.644	4.632	0.667	0.079	1.196	10.943	30.48	5.913	10.763
SR-13D	223 (PAN, CVD)	Laminar	2.524	2.432	0.290	0.105	0.218	8.974	28.67	3.213	2.191
GE-07A	223 (T-50)	Turbulent	1.824	1.679	0.194	0.067	0.088	9.130	29.69	2.322	0.830
GE-39A	223 (PAN, CVD)	Laminar	3.301	2.997	1.236	1.717	6.681	9.249	29.09	4.203	4.571
GE-44A	223 (PAN, CVD)	Laminar	3.745	4.053	0.398	-0.072	0.306	11.17	29.38	4.768	5.892
GE-02PA	FMPF (PAN)	Laminar	2.687	2.520	0.607	0.084	0.80	14.436	33.441	3.421	1.174
SR-25PA	FMPF (PAN, LoPIC)	Laminar	3.011	2.992	1.024	0.70	3.140	14.246	30.925	3.834	1.791
HAT 5	223 (PAN, HAT)	Turbulent	4.409	4.325	4.666	14.613	146.099	10.722	33.918	5.614	7.434
427-HS1	223 (PAN, CVD)	Laminar	2.051	1.853	0.467	0.106	0.3914	6.571	19.232	2.611	2.082
427-HS2	223 (PAN, CVD)	Laminar	1.423	1.274	0.338	0.025	0.230	3.190	10.309	1.811	1.988
PF928-HS2	FMPF (PAN)	Laminar	1.550	1.245	0.529	0.319	0.702	7.121	9.677	1.974	1.360
PF928-HS3	FMPF (PAN)	Laminar	1.014	0.954	0.098	0.007	0.018	7.075	11.381	1.291	0.227
668-11-HS2	223 (PAN, CVD)	Laminar	1.489	1.352	0.1831	-0.007	0.137	5.868	13.954	1.895	1.029

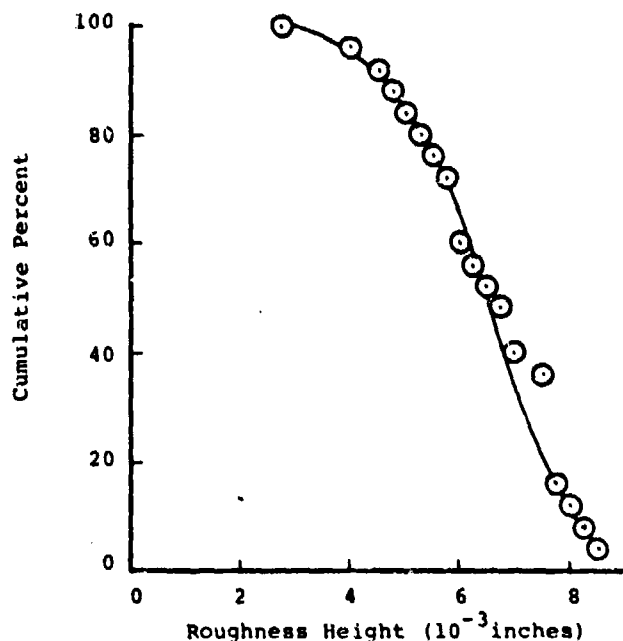


Figure 39 MACROROUGHNESS HEIGHT DISTRIBUTION FOR GE-01A (GE-223 T-50, Laminar)

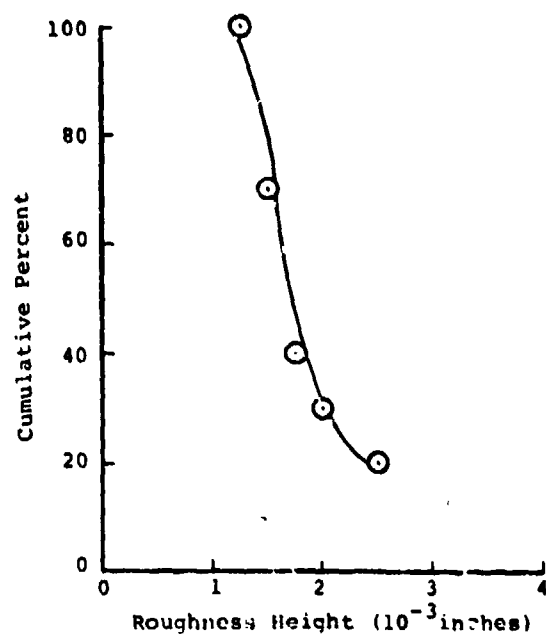


Figure 40 MACROROUGHNESS HEIGHT DISTRIBUTION FOR GE-07A (223 T-50, Turbulent)

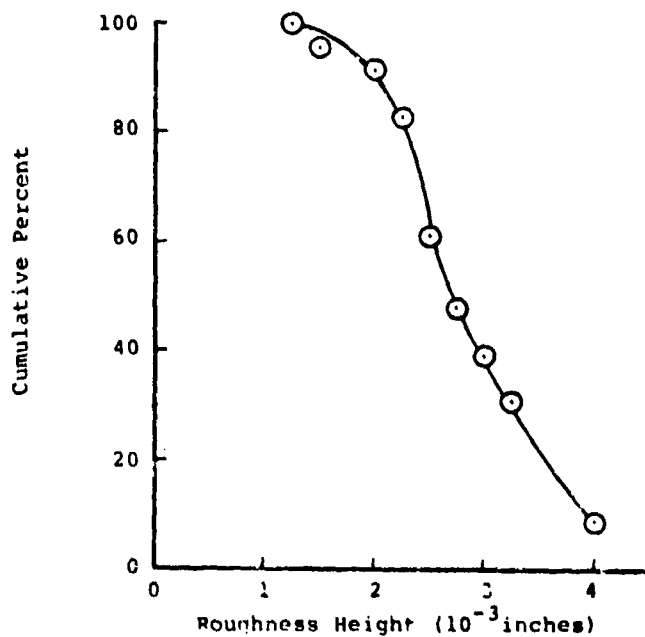


Figure 41 MACROROUGHNESS HEIGHT DISTRIBUTION FOR GE-07A3 (223 T-50, MDAC, Laminar)

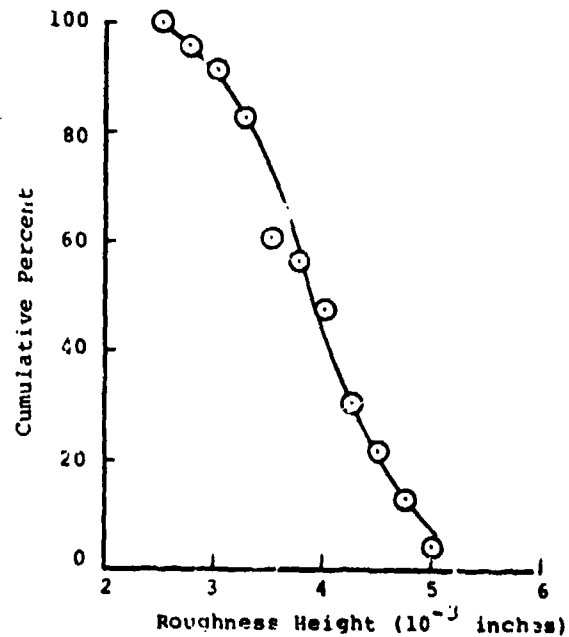


Figure 42 MACROROUGHNESS HEIGHT DISTRIBUTION FOR SR-10D (223 PAN, No CVD, Laminar)

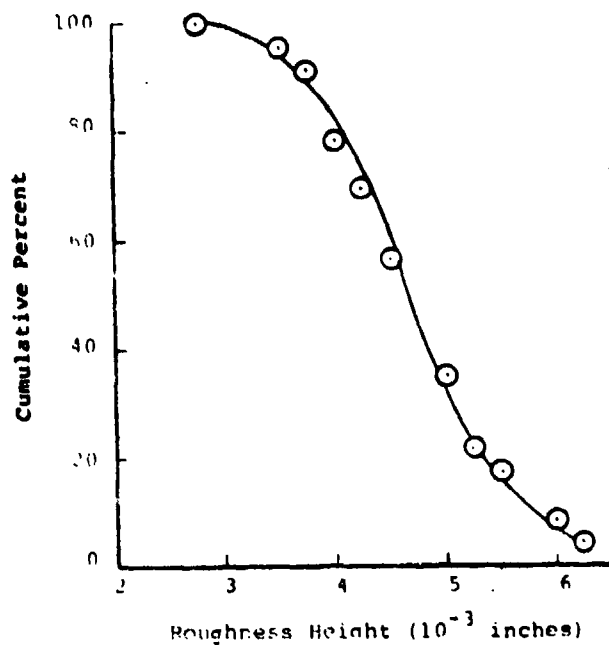


Figure 43 MACROROUGHNESS HEIGHT DISTRIBUTION FOR SR-12D (223 PAN, Nb CVD, Initial LOPIC, Laminar)

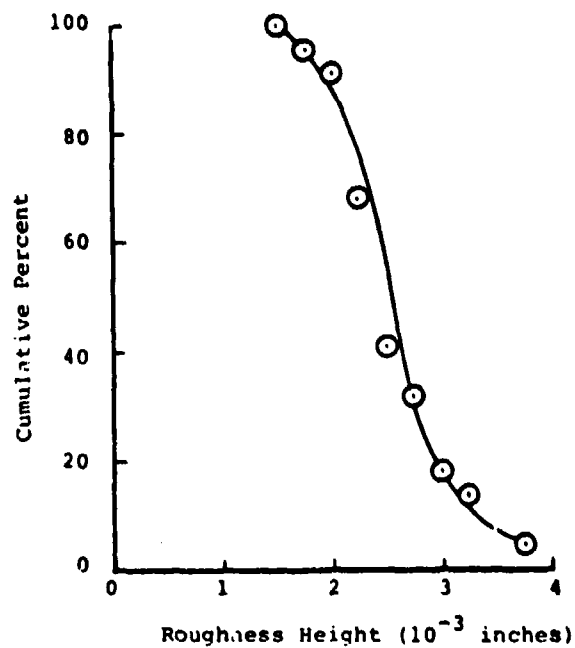


Figure 44 MACROROUGHNESS HEIGHT DISTRIBUTION FOR SR-13D (223 PAN, CVD, 2300°C Graph, Laminar)

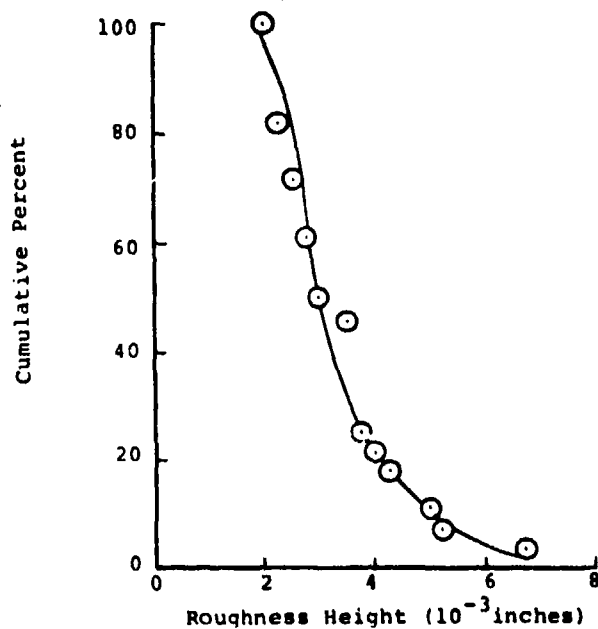


Figure 45 MACROROUGHNESS HEIGHT DISTRIBUTION FOR GE-39A (223 PAN, CVD, Laminar)

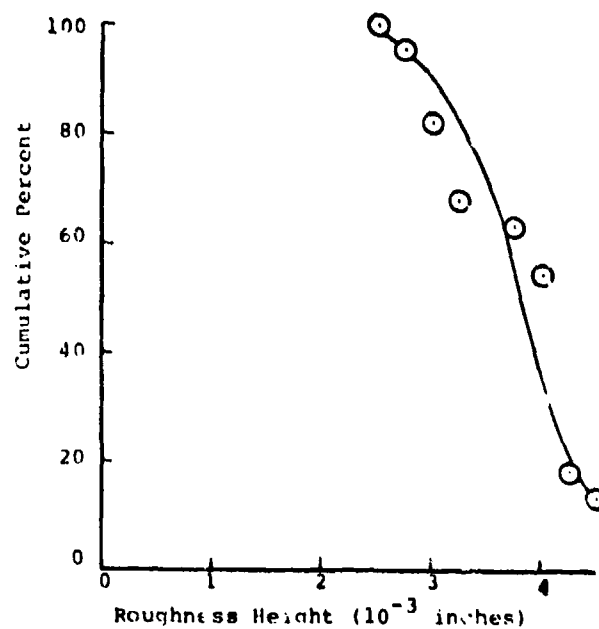


Figure 46 MACROROUGHNESS HEIGHT DISTRIBUTION FOR GE-44A (223 PAN, CVD, Laminar)

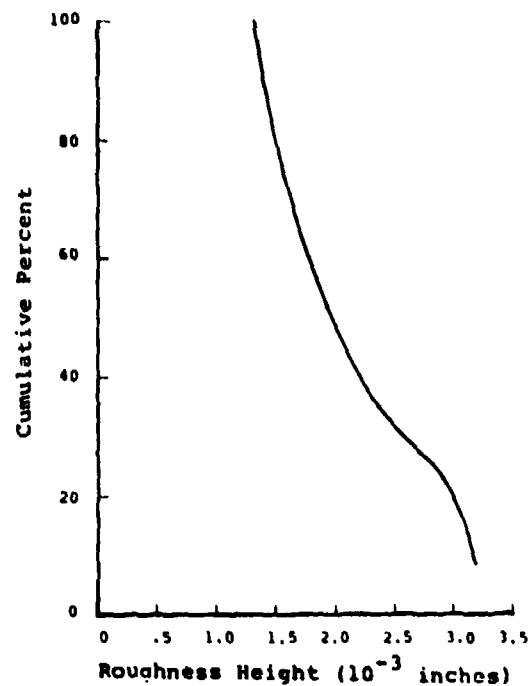


Figure 47 MACROROUGHNESS HEIGHT DISTRIBUTION FOR 427-HS1 (223 PAN, CVD, Laminar)

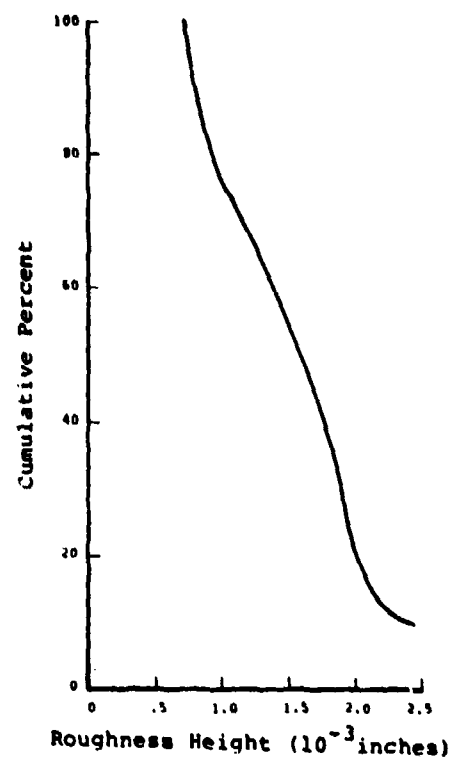


Figure 48 MACROROUGHNESS HEIGHT DISTRIBUTION FOR 427-HS2 (223 PAN, CVD, Laminar)

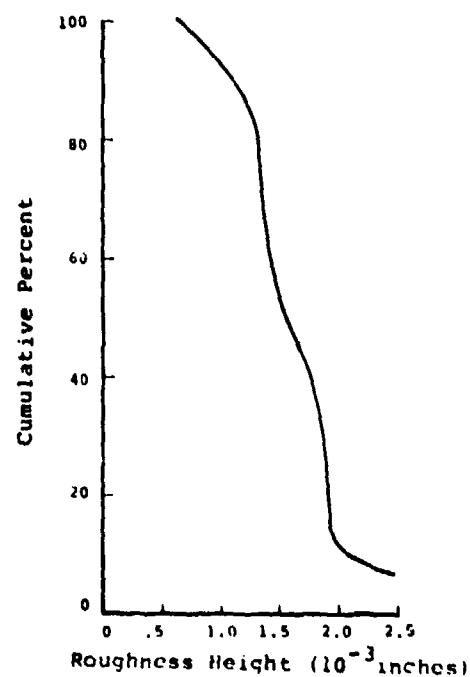


Figure 49 MACROROUGHNESS HEIGHT DISTRIBUTION FOR 668-11-HS2 (223 PAN, CVD, Laminar)

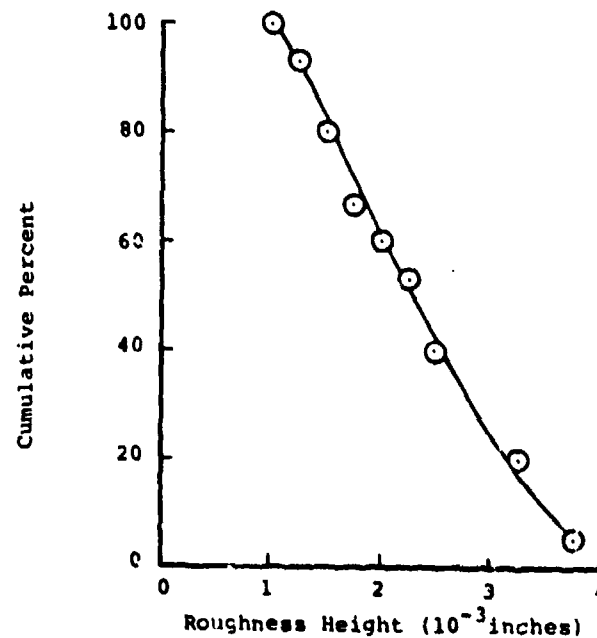


Figure 50 MACROROUGHNESS HEIGHT DISTRIBUTION FOR GE-04A3 (223-PAN, HAT, Turbulent)

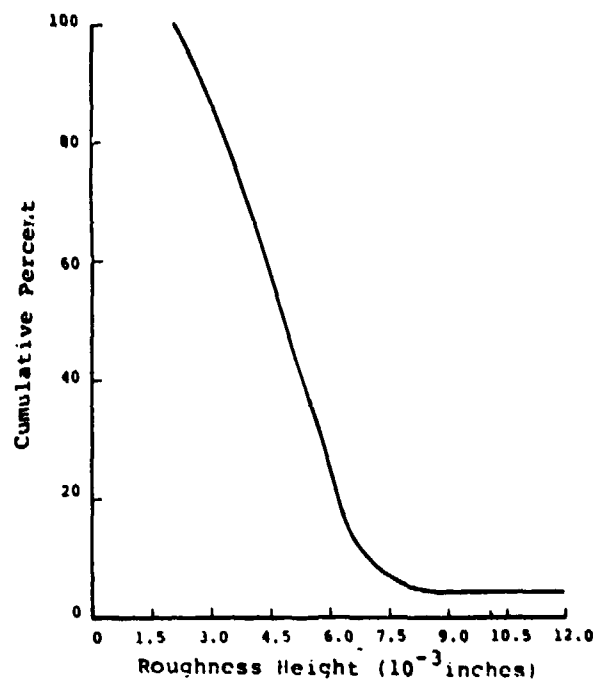


Figure 51 MACROROUGHNESS HEIGHT DISTRIBUTION FOR HAT 5 (223 PAN, HAT, Turbulent)

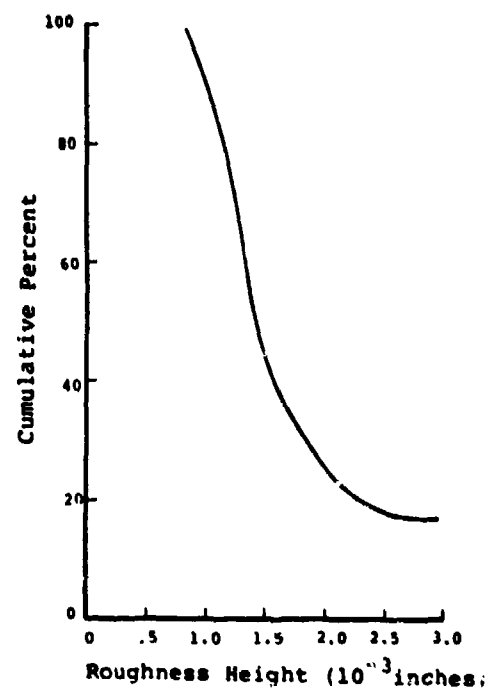


Figure 52 MACROROUGHNESS HEIGHT DISTRIBUTION FOR PF928-HS2 (FWPF PAN, Laminar)

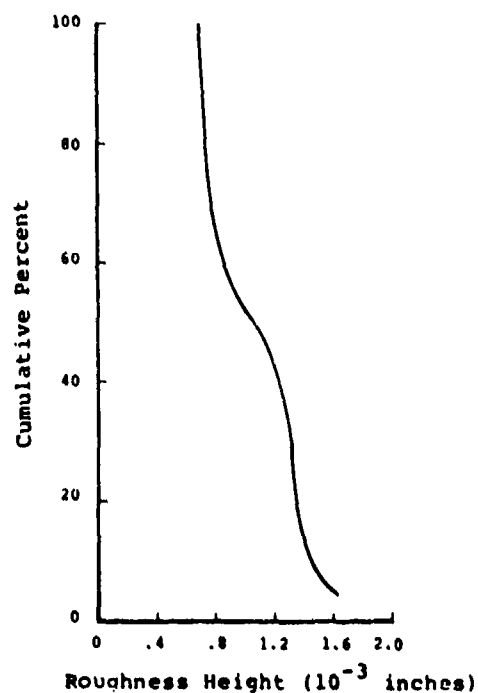


Figure 53 MACROROUGHNESS HEIGHT DISTRIBUTION FOR PF-928-HS3 (FWPF PAN, Laminar)

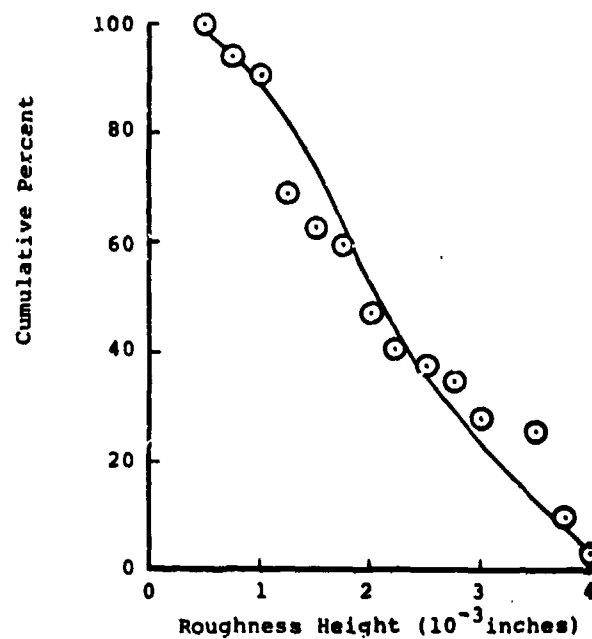


Figure 54 MACROROUGHNESS HEIGHT DISTRIBUTION FOR GE-06A3 (FWPF PAN, Laminar)

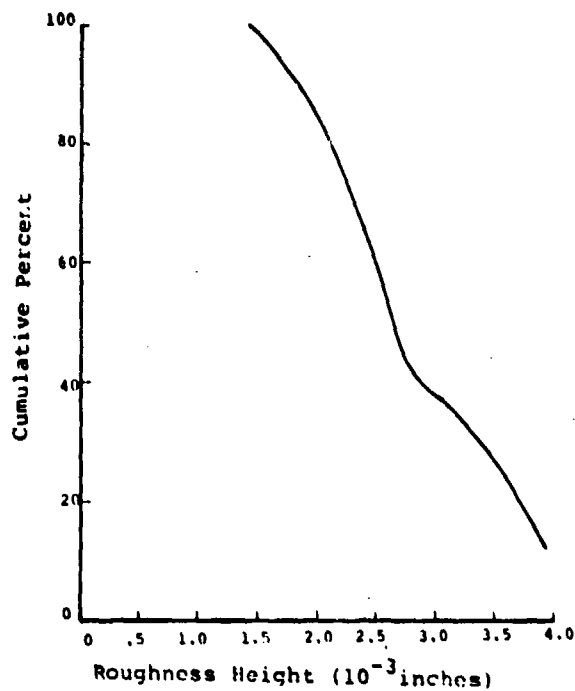


Figure 55 MACROROUGHNESS HEIGHT DISTRIBUTION FOR GE-02PA (FWPF PAN, Laminar)

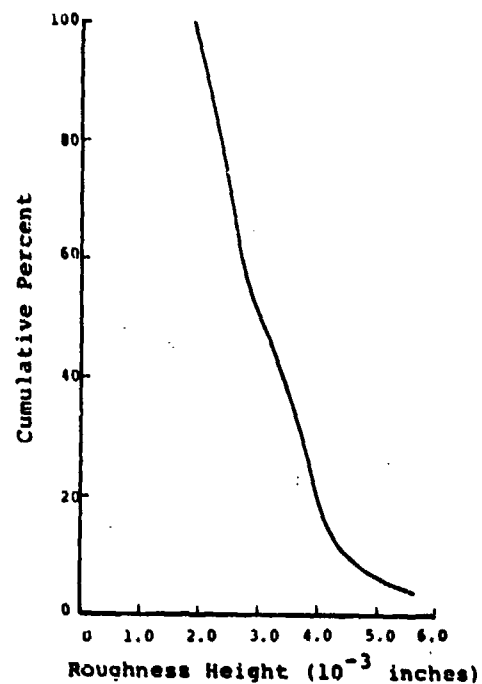


Figure 56 MACROROUGHNESS HEIGHT DISTRIBUTION FOR SR-25PA (FWPF PAN, LoPIC, Laminar)

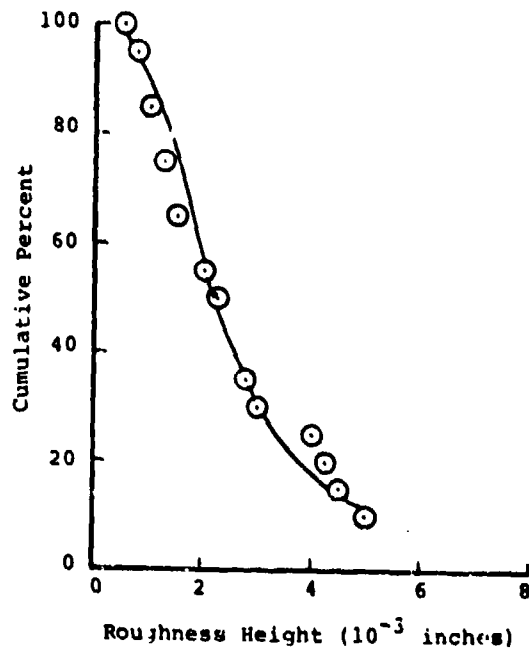


Figure 57 MACROROUGHNESS HEIGHT DISTRIBUTION FOR SR-07AD (Pitch-No CVD, Laminar)

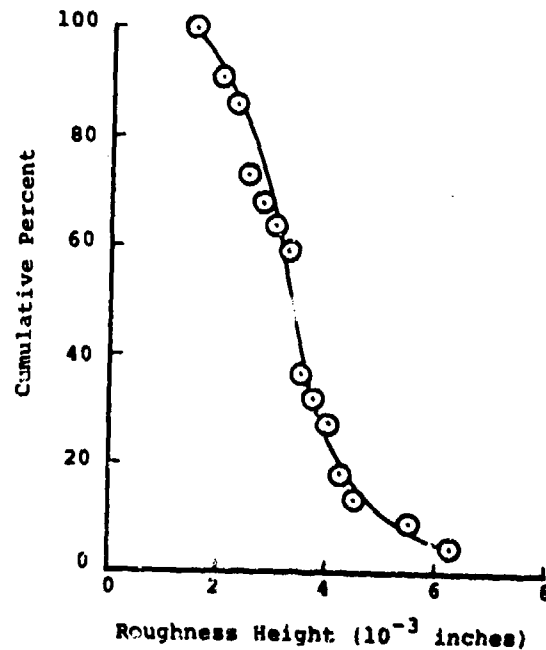


Figure 58 MACROROUGHNESS HEIGHT DISTRIBUTION FOR SR-08AD (Pitch with CVD, Laminar)

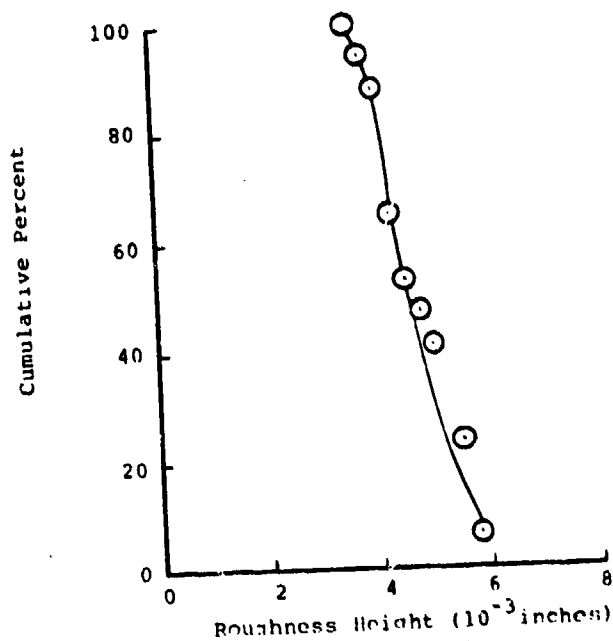


Figure 59 MACROROUGHNESS HEIGHT DISTRIBUTION FOR AFML-23R (FWPF, LoPIC, Laminar)

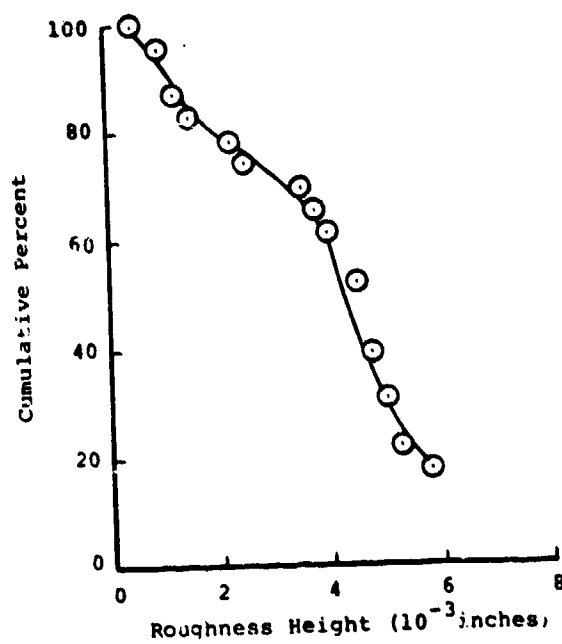


Figure 60 MACROROUGHNESS HEIGHT DISTRIBUTION FOR AFML-19R (Jellyroll, Laminar)

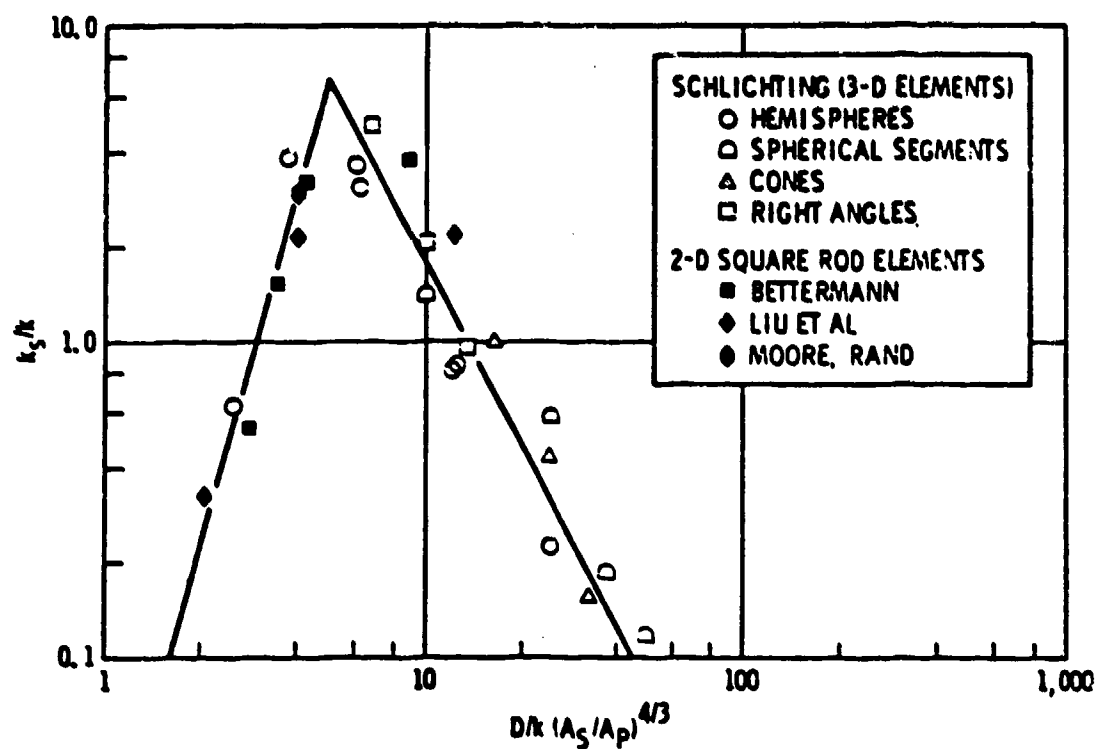
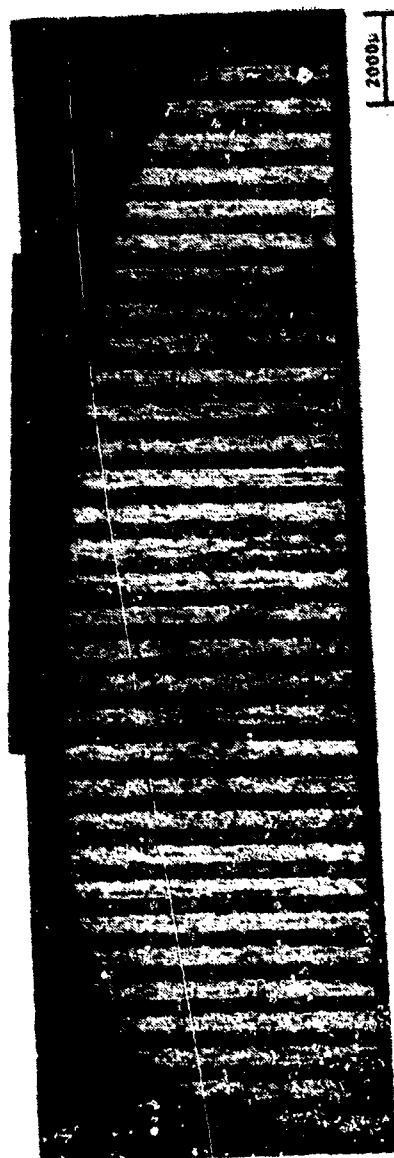


Figure 61 EFFECT OF ROUGHNESS ELEMENT SPACING AND SHAPE IN EQUIVALENT SAND ROUGHNESS

It should be noted that while k_s values are reported in Table 6 for laminar models, the utility of equivalent sand roughness values for describing laminar flow phenomena has not been established.

2.3 Microscopy

Macro - and microphotographs of each ablation model are presented in this section. Descriptive information regarding the material, test conditions and model number is contained on each sheet.



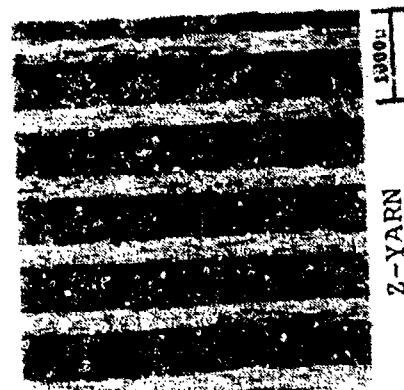
CROSS SECTION



SIDE VIEW



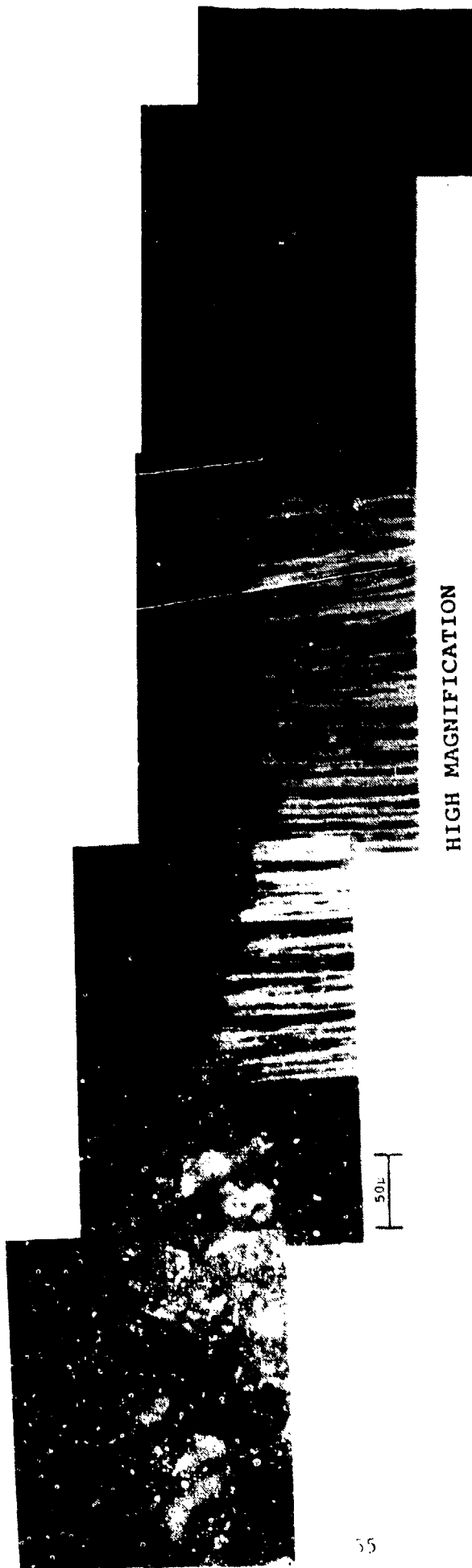
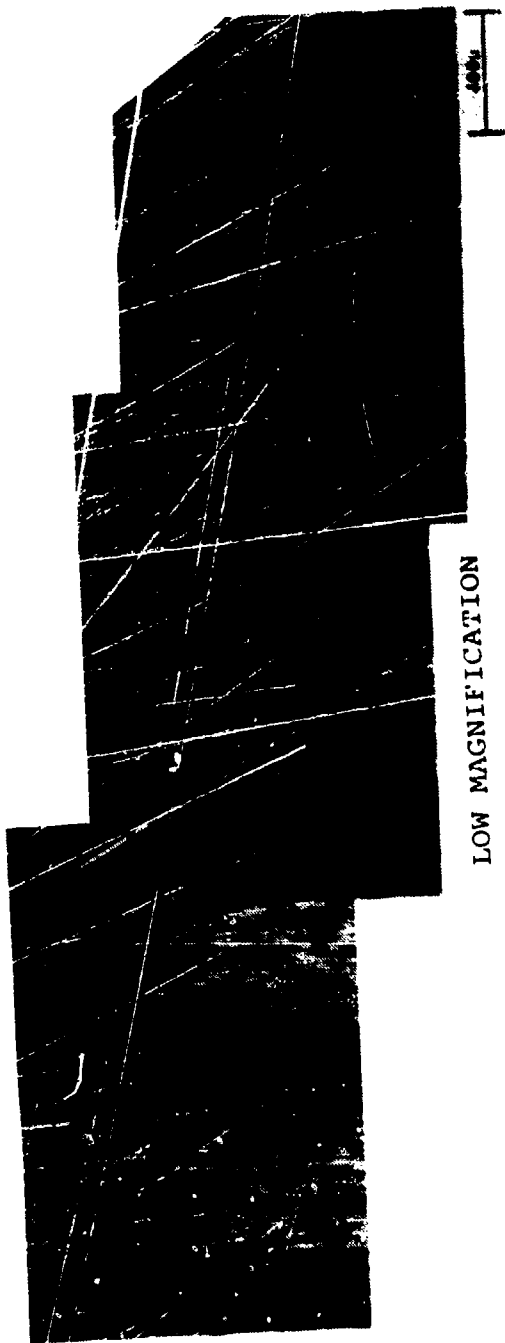
STEREO VIEW



Z-YARN

AFFDL 50 MW - 76 ATM
RAMP, PEAKED ENTHALPY
BILLET 399-R1 - 0.97 INCH DIAMETER

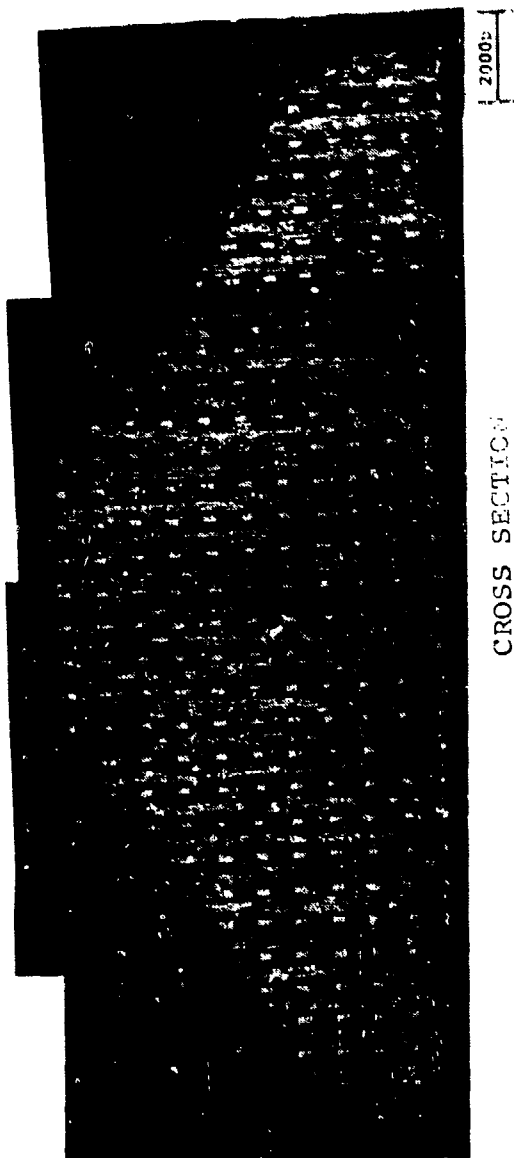
Figure 62 PHOTOMICROGRAPHS OF GE 223 T-50 GE-01A



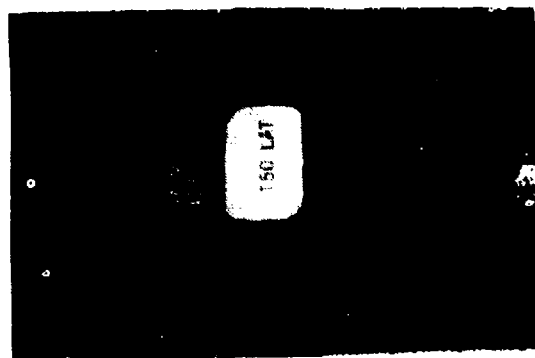
AFFDL 50 MW - 76 ATM
RAMP, PEAKED ENTHALPY

BILLET 399-R1 - 0.97 INCH DIAMETER

Figure 62 (continued) PHOTOMICROGRAPHS OF GE 223 T-50 GE-01A



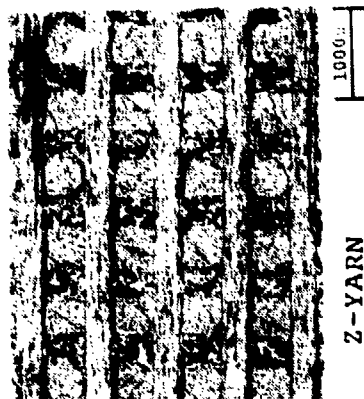
CROSS SECTION



SIDE VIEW



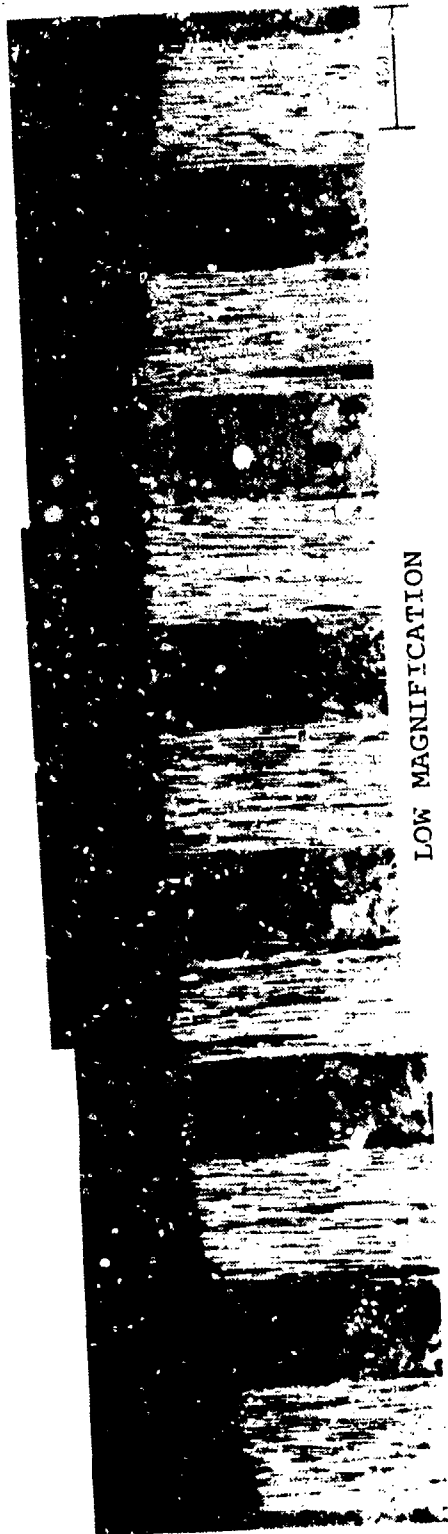
STEREO VIEW



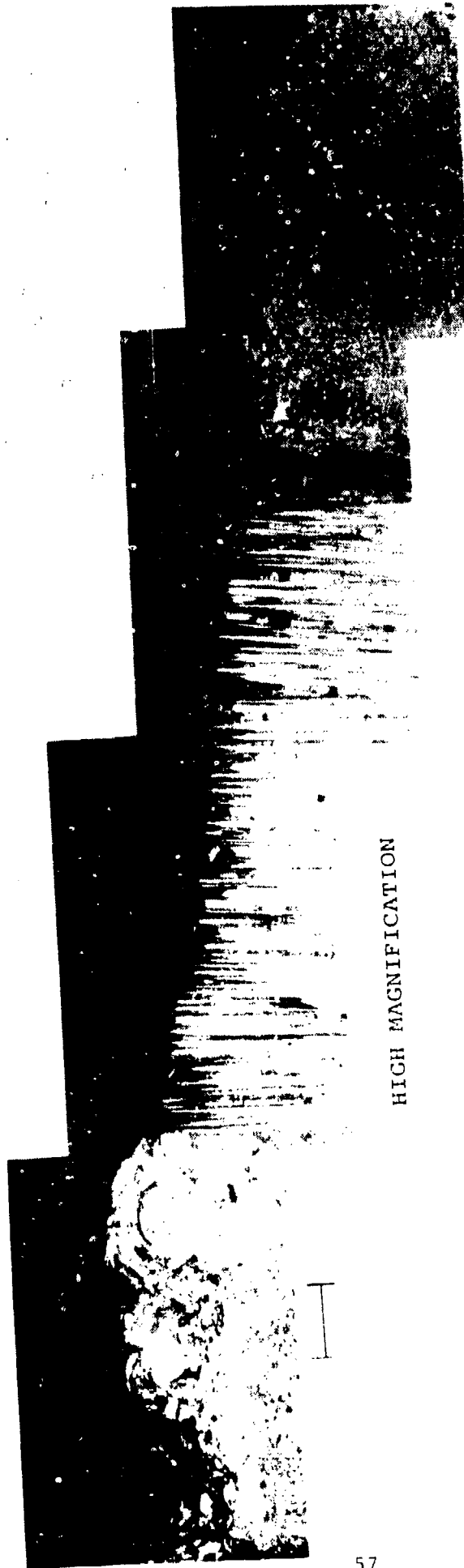
Z-YARN

AFFDL 50 MW - 76 ATM
RAMP, PEAKED ENTHALPY
BILLET 425-R3 - 1.00 INCH DIAMETER

Figure 63 (continued) PHOTOMICROGRAPHS OF 223 T-50 GE-07A

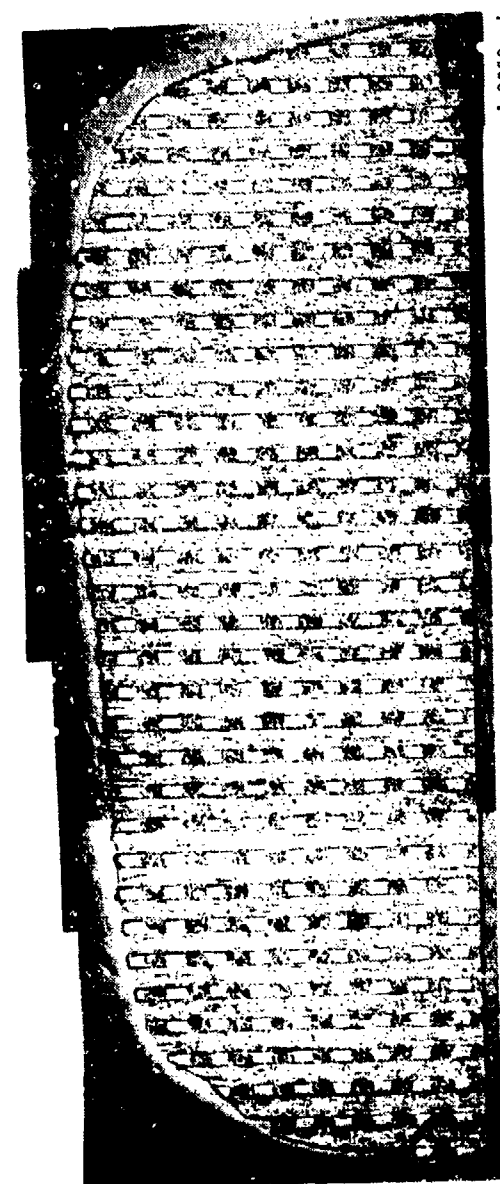


LOW MAGNIFICATION

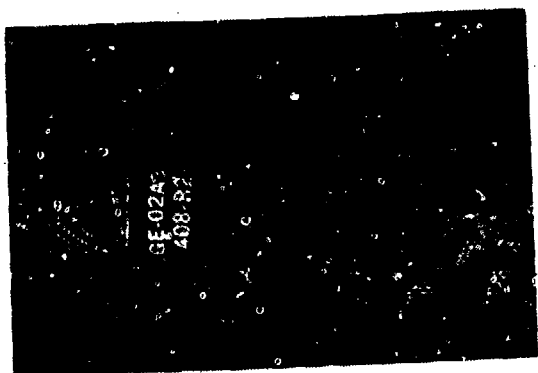


HIGH MAGNIFICATION

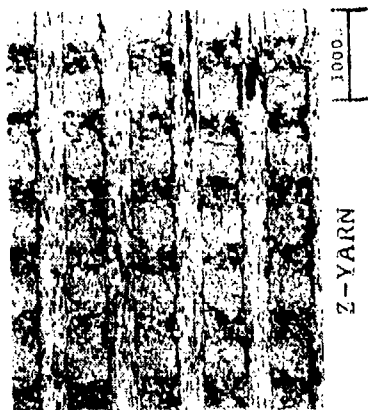
AFFDL 50 MW · 76 ATM
 RAMP, PEAKED ENTHALPY
 BILLET 425-R3 · 1.00 INCH DIAMETER



CROSS SECTION



SIDE VIEW



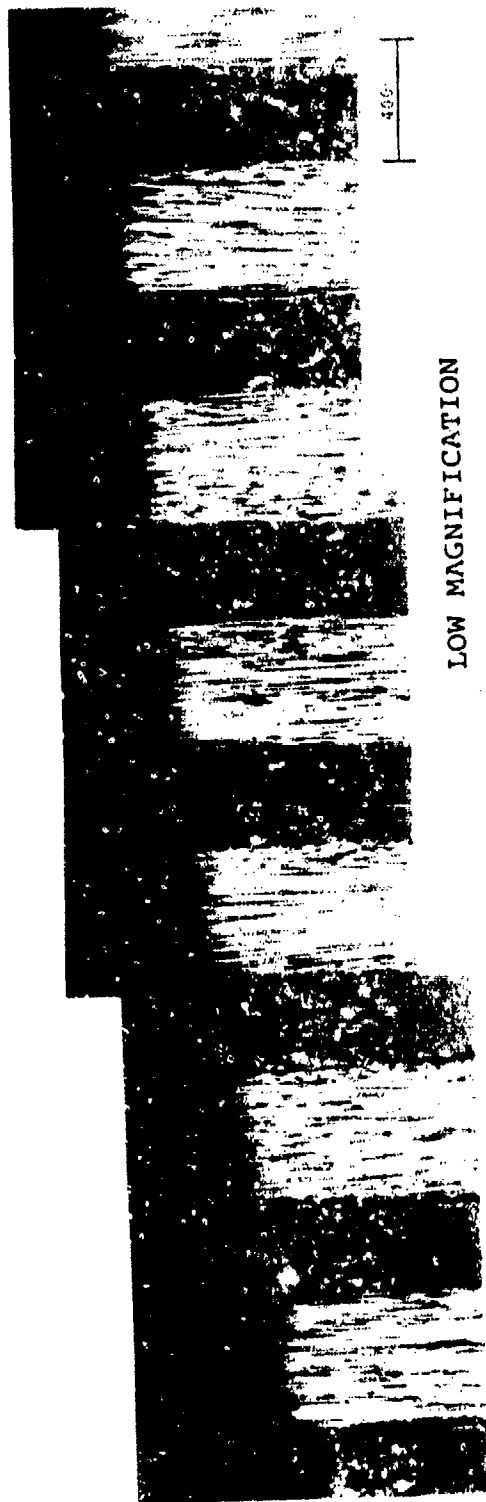
Z-YARN



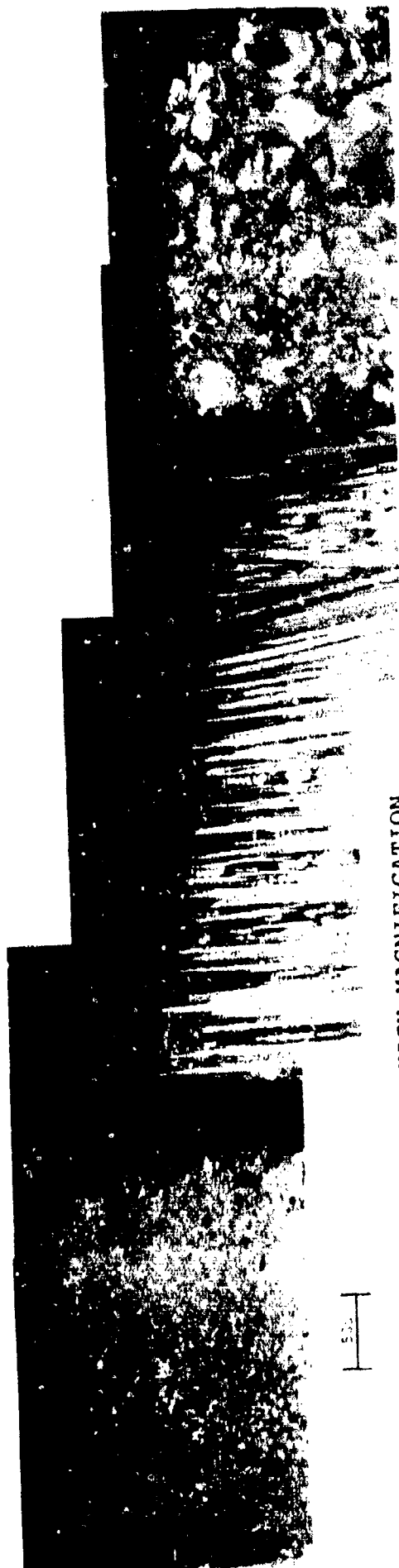
STEREO VIEW

AFFDL 50 MW · 76 ATM
RAMP, PEAKED ENTHALPY
BILLET 408-R2 · 1.03 INCH DIAMETER

Figure 64 PHOTOMICROGRAPHS OF 223 T-50, MDAC GE-02A3



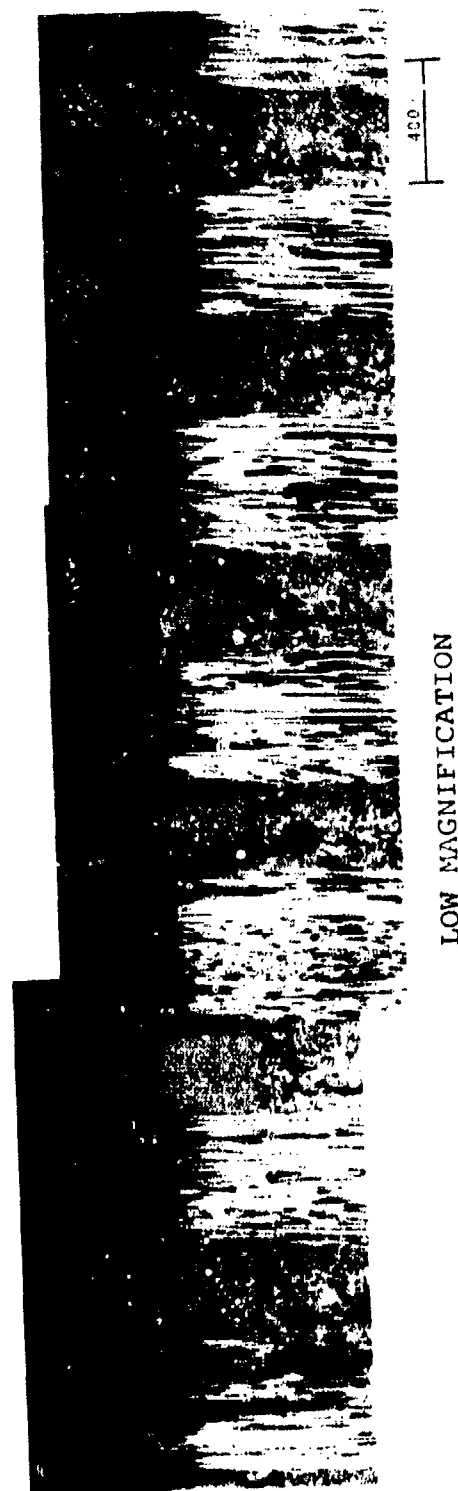
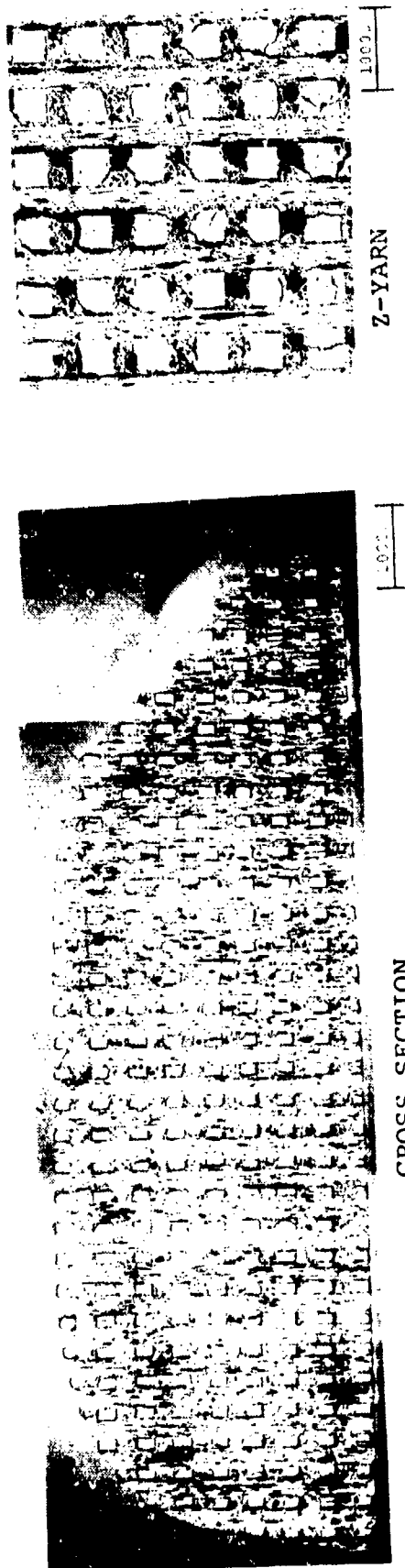
LOW MAGNIFICATION



HIGH MAGNIFICATION

AFFDL 50 MW · 76 ATM
 RAMP, PEAKED ENTHALPY
 BILLET 408-R2 · 1.03 INCH DIAMETER

Figure 64 (continued) PHOTOMICROGRAPHS OF 223 T-5C, MDAC GE-02A3



AFEDL 50 MW . 76 ATM
 RAMP, PEAKED ENTHALPY
 BILLET 1819-3-R2 . 0.98 INCH DIAMETER

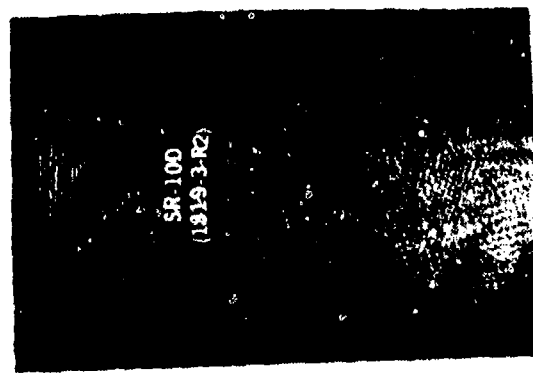
Figure 65 PHOTOMICROGRAPHS OF 223 PAN, no CVD SR-10D



HIGH MAGNIFICATION



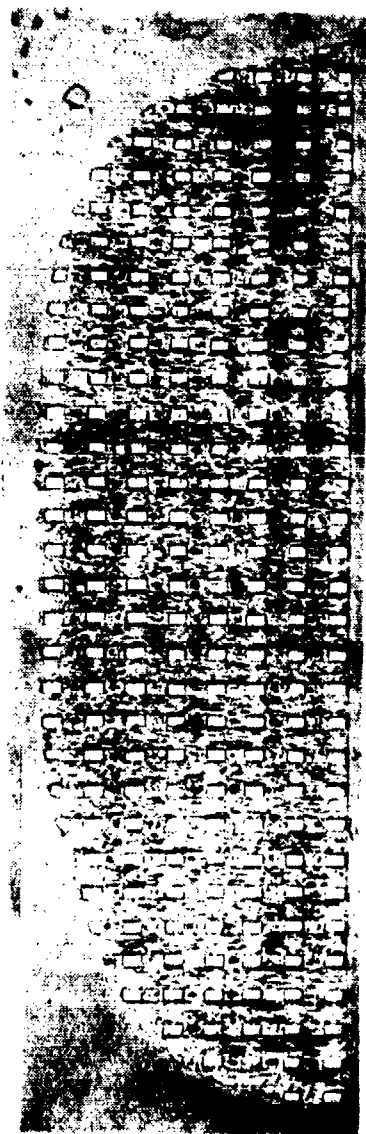
STEREO VIEW



SIDE VIEW

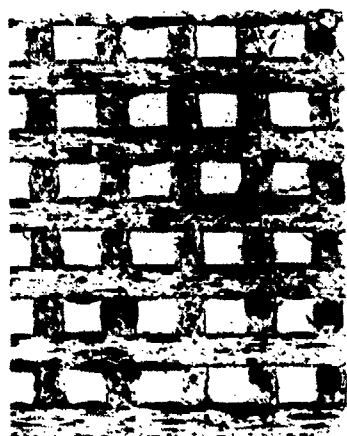
AFFDL 50 MW - 76 ATM
RAMP, PEAKED ENTHALPY
BILLET 1819-3-R2 - 0.98 INCH DIAMETER

Figure 65 (continued) PHOTOMICROGRAPHS OF 223 PAN, no CVD SR-10D



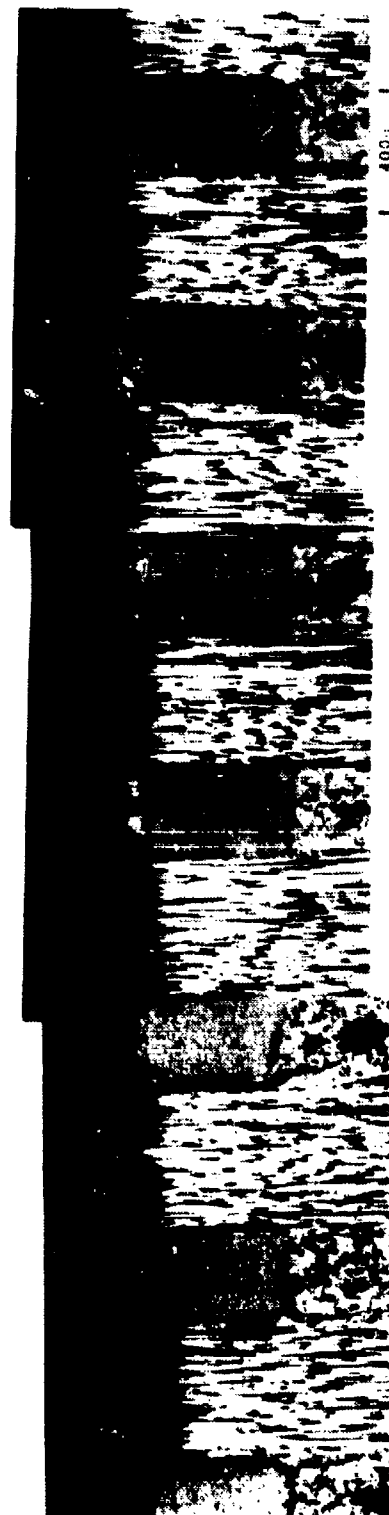
CROSS SECTION

2000.



Z-YARN

1000.



LOW MAGNIFICATION

400.

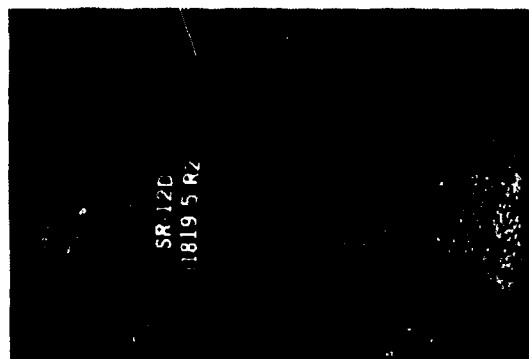
AFFDL 50 MW · 76 ATM
RAMP, PEAKED ENTHALPY

BILLET 1819-5-R2 · 0.98 INCH DIAMETER

Figure 66 PHOTOMICROGRAPHS OF 223 PAN, no CVD, initial LOPIC SR-12D.



STEREO VIEW



SIDE VIEW

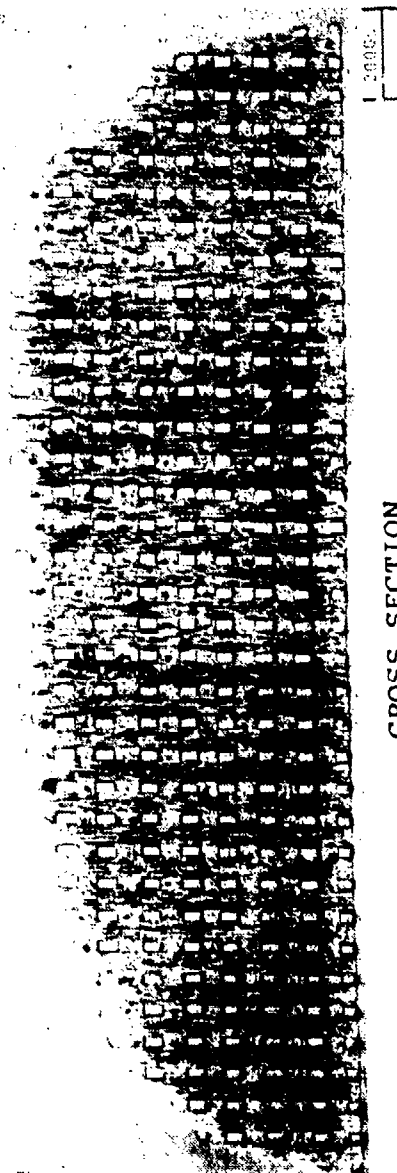


50-

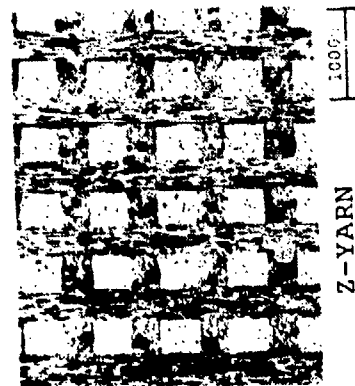
HIGH MAGNIFICATION



AFFDL 50 MW - 76 ATM
RAMP, PEAKED ENTHALPY
BILLET 1819-5-R2 - 0.98 INCH DIAMETER



CROSS SECTION



Z-YARN



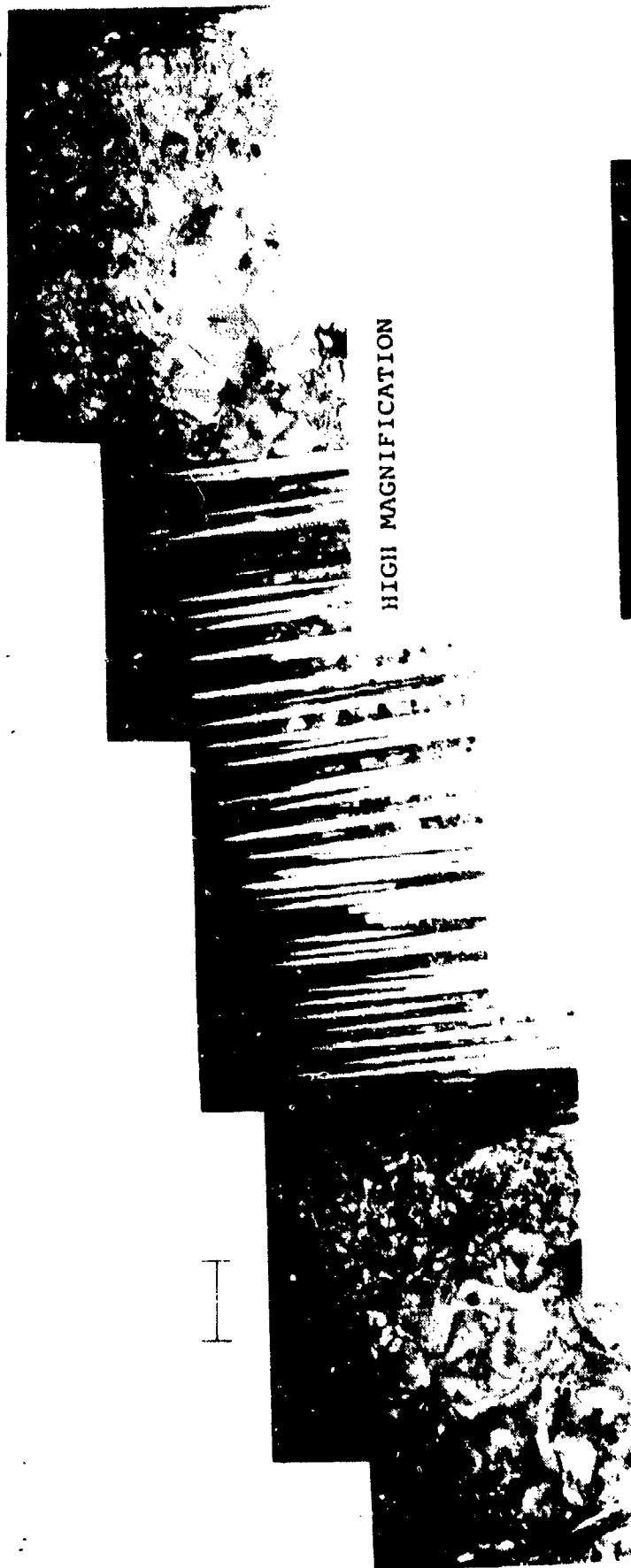
STEREO VIEW



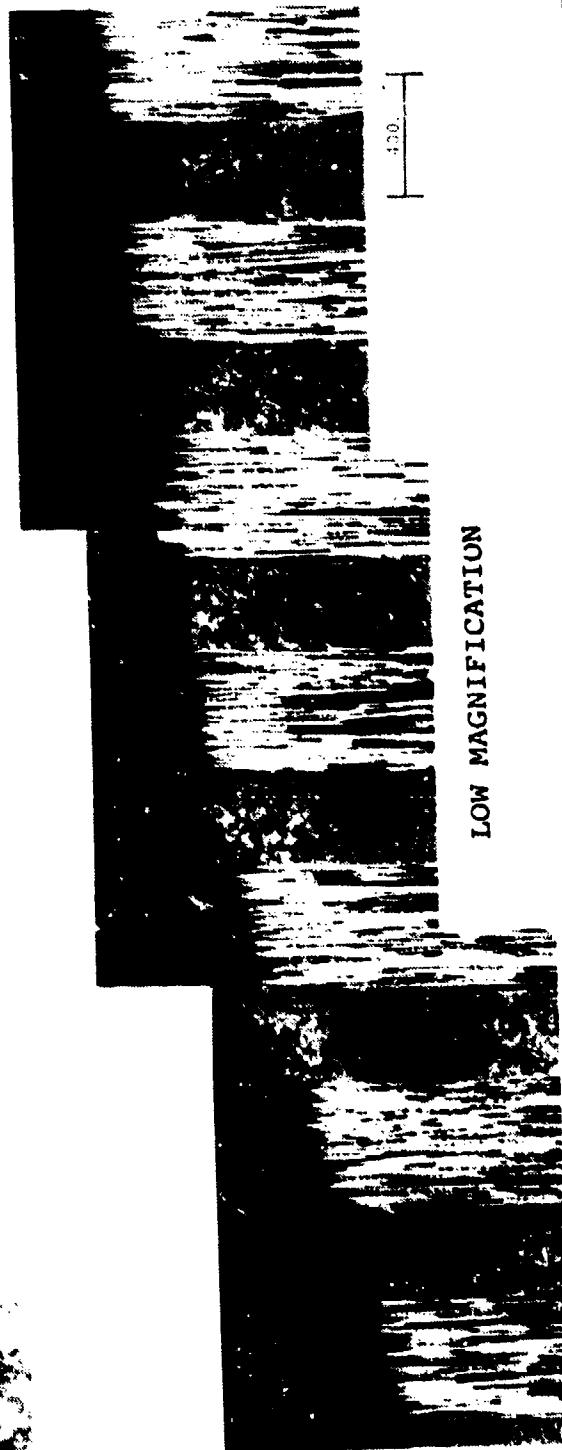
SIDE VIEW

AFFDL 50 MW • 76 ATM
RAMP, PEAKED ENTHALPY
BILLET 1819-2-RZ1 • 1.03 INCH DIAMETER

Figure 67 PHOTOMICROGRAPHS OF 223 PAN, CVD SR-13D



HIGH MAGNIFICATION



LOW MAGNIFICATION

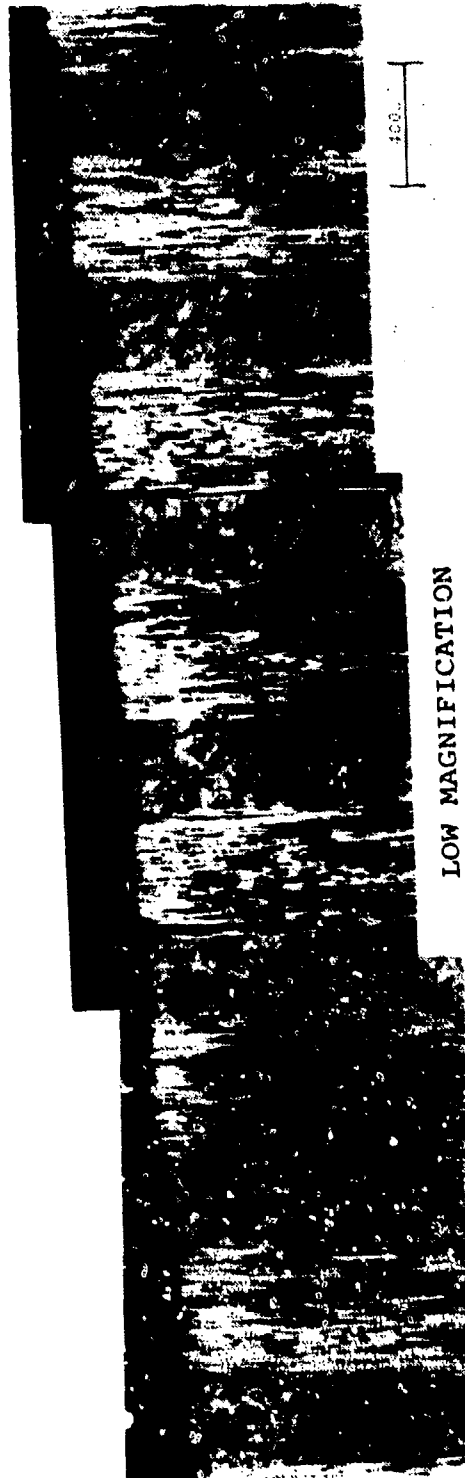
AFDDL 50 MW - 76 ATM
RAMP, PEAKED ENTHALPY
BILLET 1819-2-KZ1 - 1.03 INCH DIAMETER



CROSS SECTION



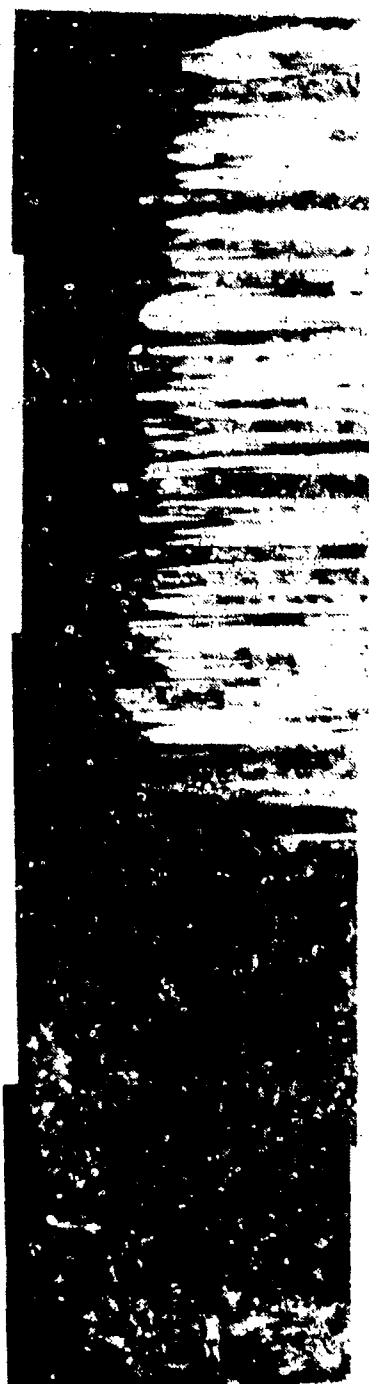
Z-YARN



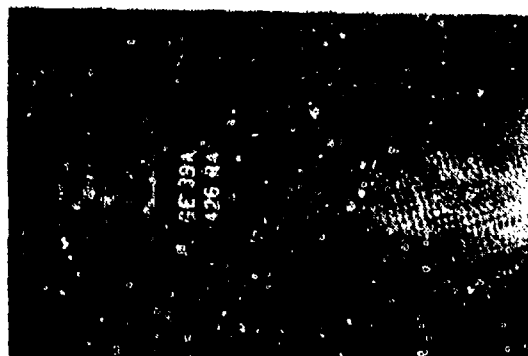
LOW MAGNIFICATION

AFFDL 50 MW - 76 ATM
RAMP, PEAKED ENTHALPY
BILLET 426-R4 - 1.03 INCH DIAMETER

Figure 68 PHOTOMICROGRAPHS OF 223 PAN, CVD GE-39A



HIGH MAGNIFICATION



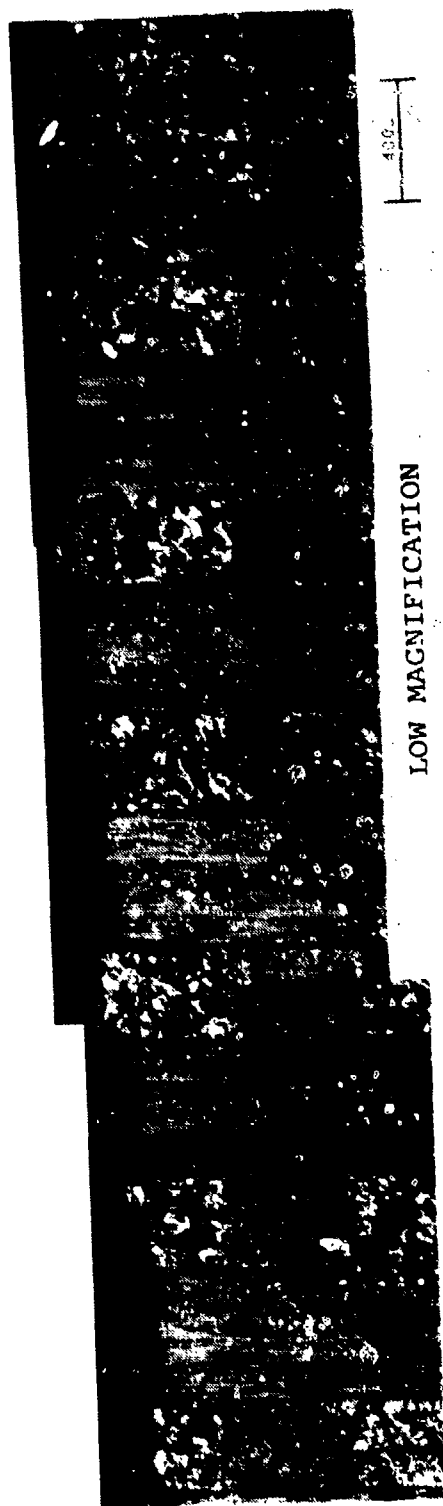
SIDE VIEW



STEREO VIEW

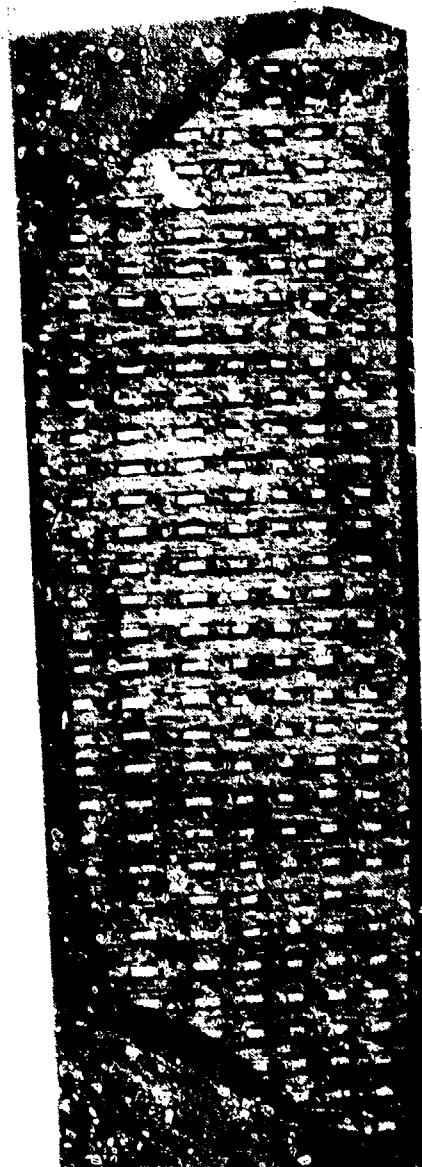
AFFDL 50 MW - 76 ATM
RAMT, PEAKED ENTHALEY
BILLET 426-R4 - 1.03 INCH DIAMETER

Figure 68 (continued) PHOTOMICROGRAPHS OF 223 PAN, CVD GE-39A



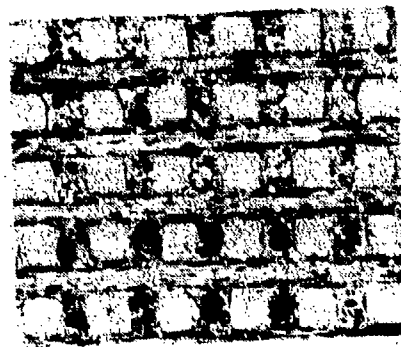
LOW MAGNIFICATION

400



CROSS SECTION

200



Z-YARN

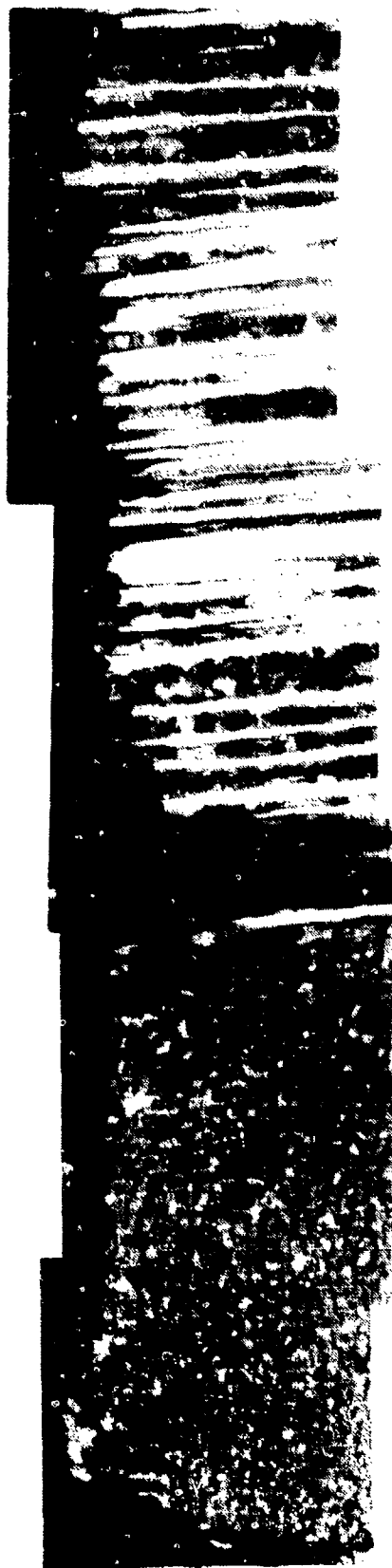
100

AFFDL 50 MW · 76 ATM

RAMP, PEAKED ENTHALPY

BILLET 427-R4 · 1.00 INCH DIAMETER

Figure 69 PHOTOMICROGRAPHS OF 223 PAN, CVD GE-44A



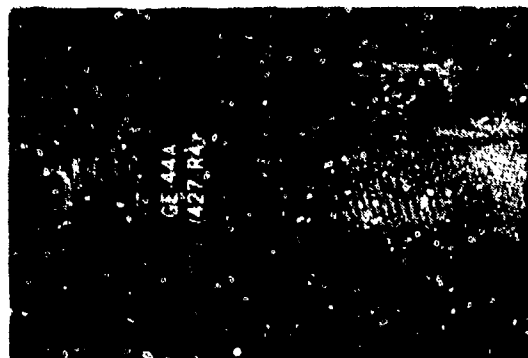
HIGH MAGNIFICATION



50

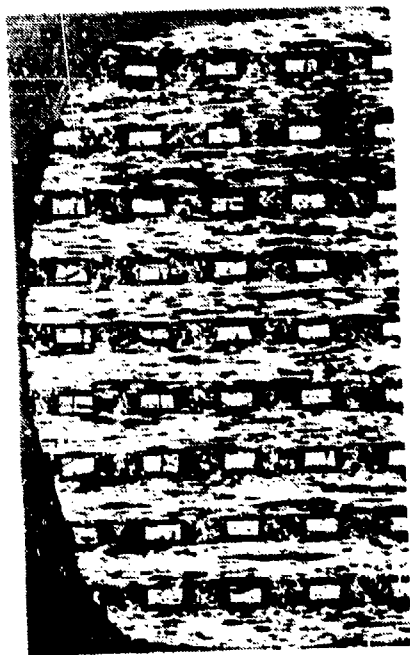


STEREO VIEW



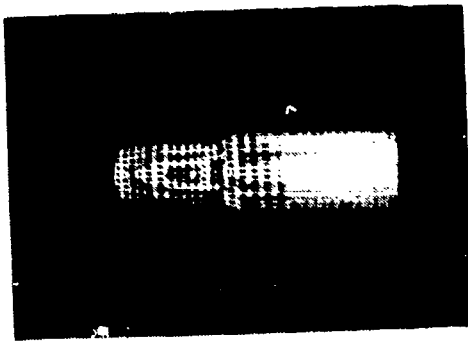
SIDE VIEW

AFFDL 50 MW - 76 ATN
RAMP, PEAKED ENTHALPY
BILLET 427-R4 - 1.00 INCH DIAMETER



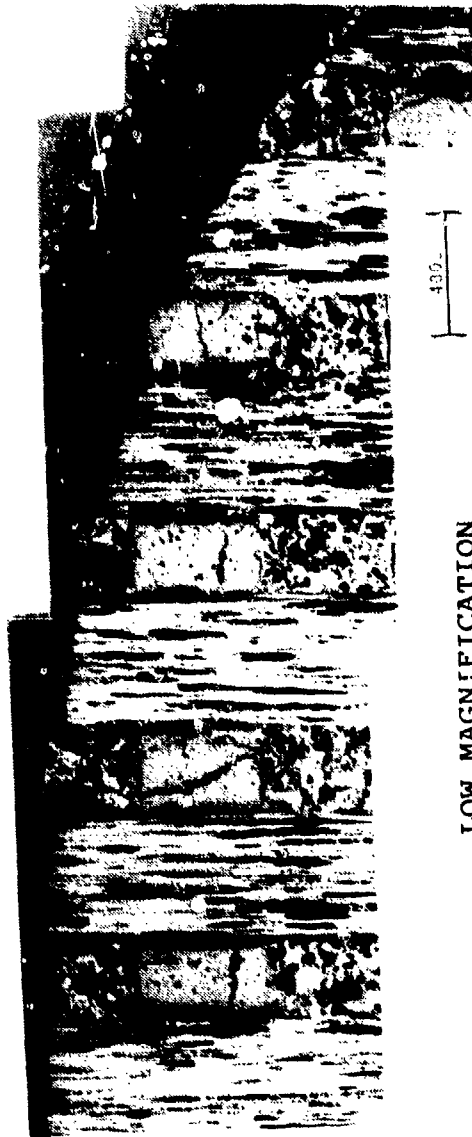
CROSS SECTION

100μ



SIDE VIEW

430μ



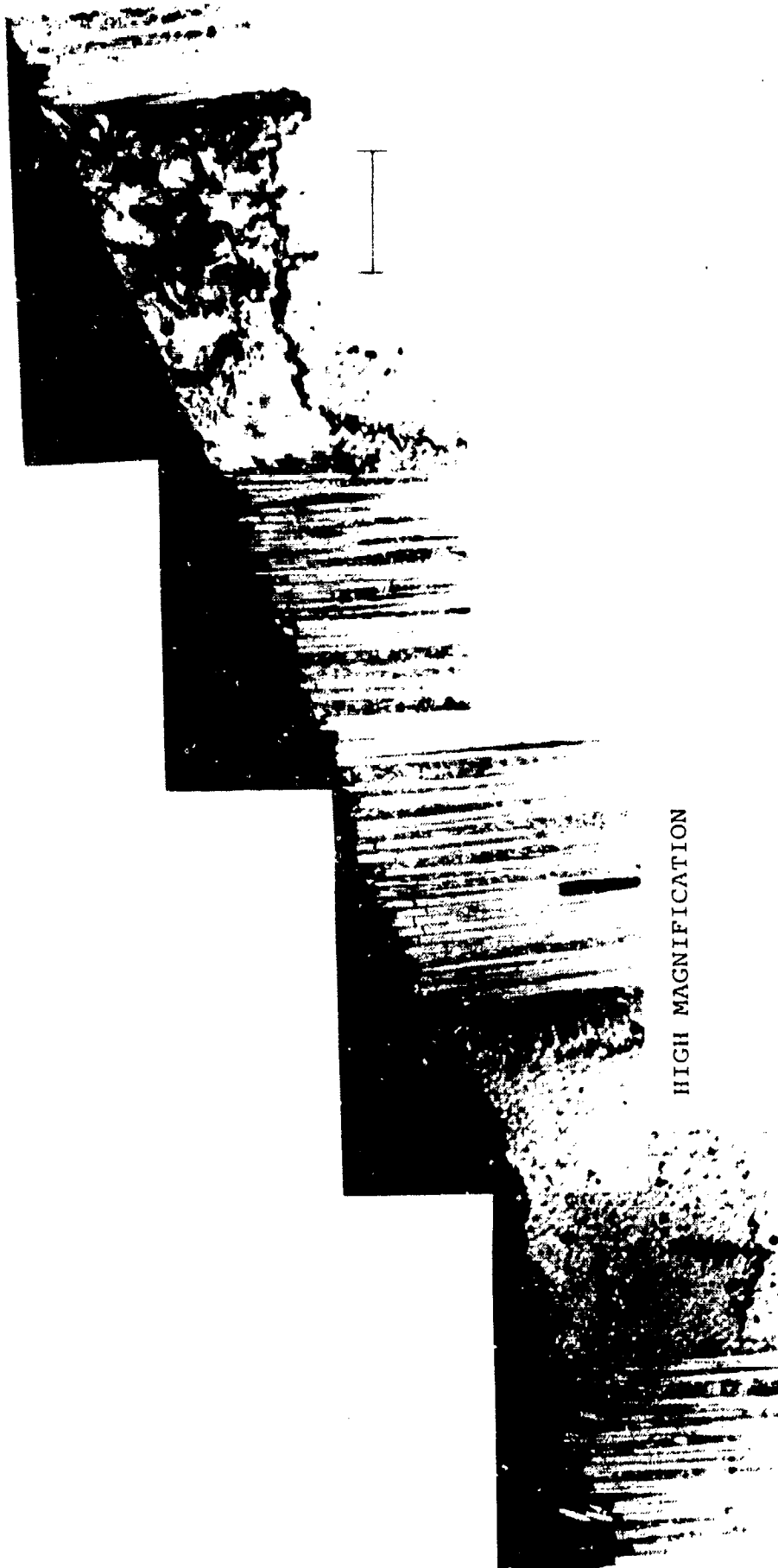
LOW MAGNIFICATION

MDAC HIP FACILITY - 7ATM

STEADY STATE

BILLET 427 - 0.28 INCH DIAMETER

Figure 70 PHOTOMICROGRAPHS OF 223 PAN, CVD 427-HS1



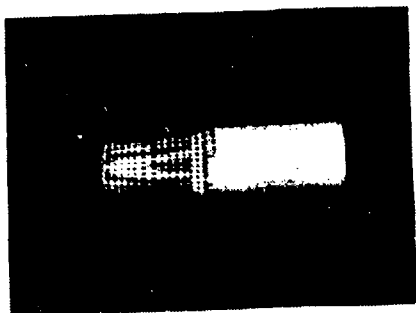
HIGH MAGNIFICATION

MDAC HIP FACILITY • 7ATM

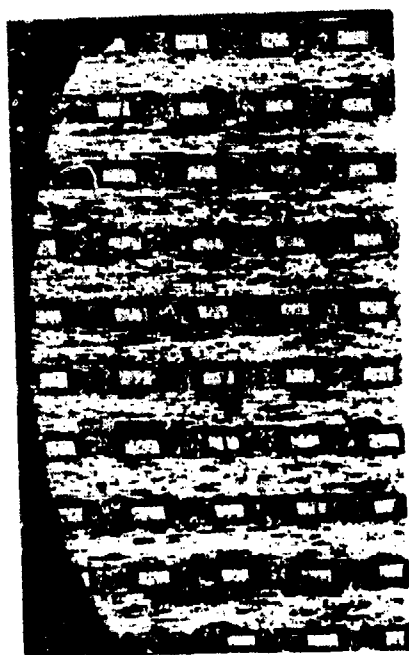
STEADY STATE

BILLET 427 • 0.28 INCH DIAMETER

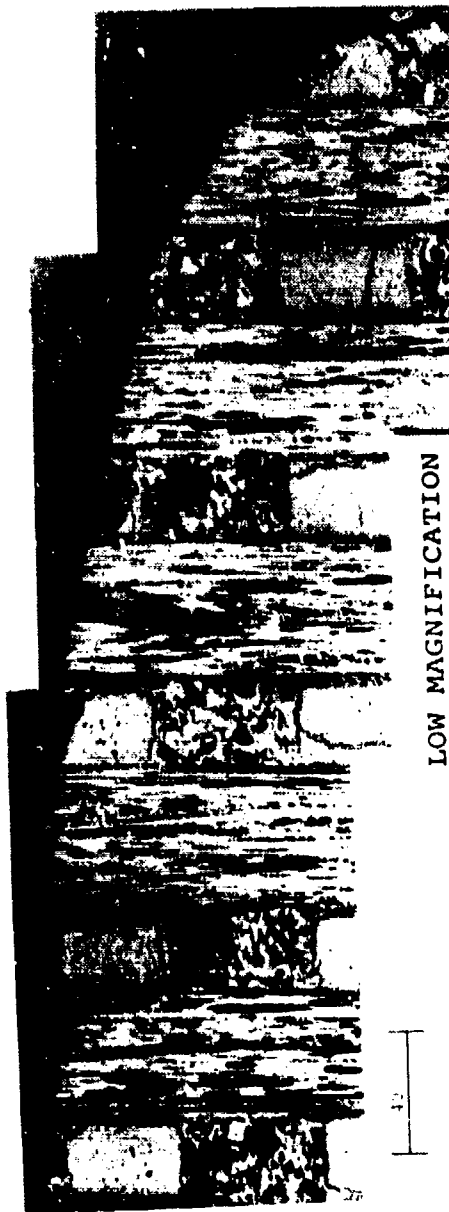
Figure 70 (continued) PHOTOMICROGRAPHS OF 223 PAN, CVD 427-HS1



SIDE VIEW



CROSS SECTION



LOW MAGNIFICATION

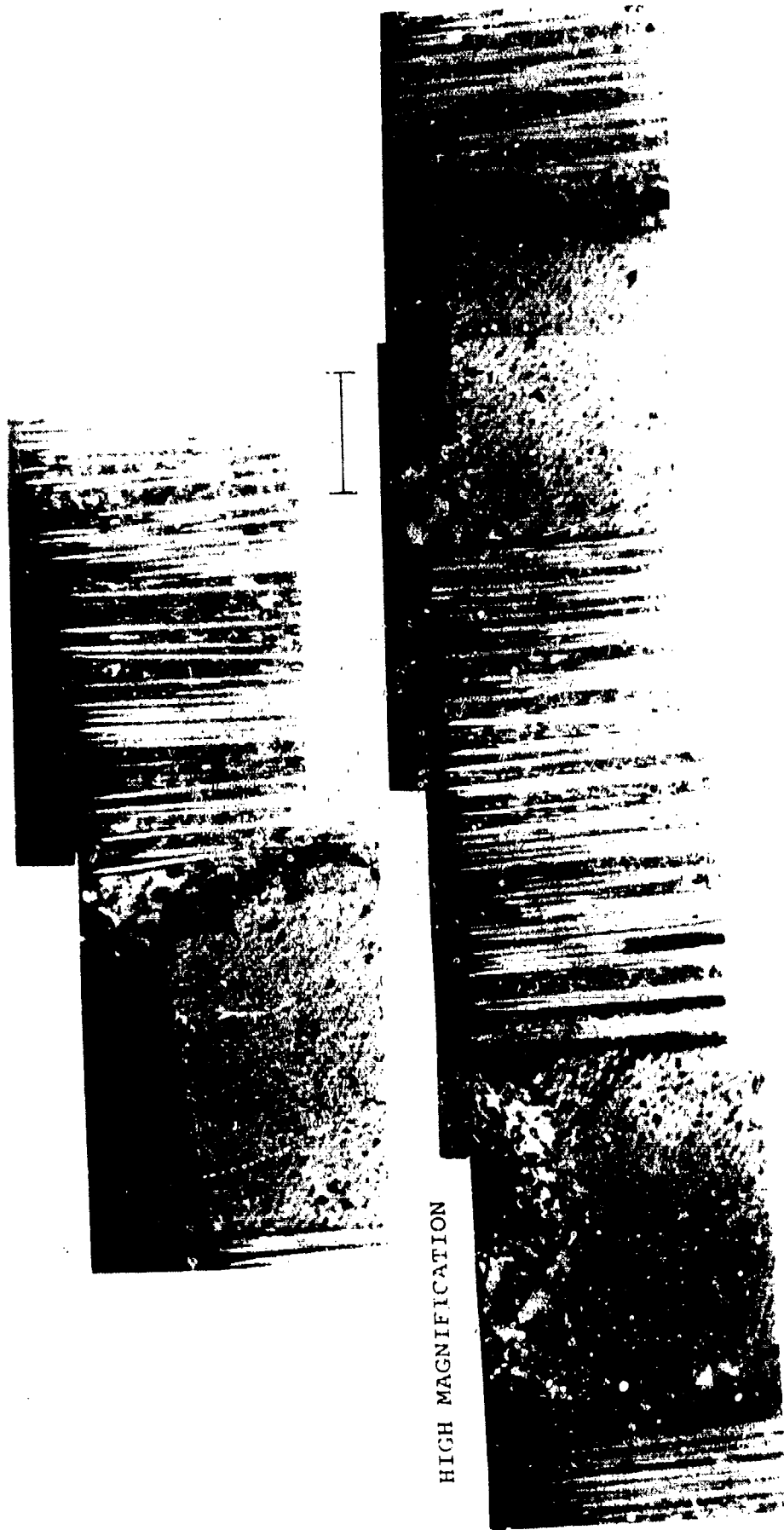


MDAC HIP FACILITY • 7ATM

STEADY STATE

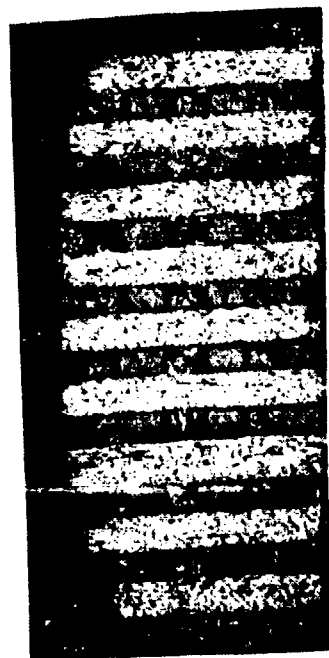
BILLET 427 • 0.28 INCH DIAMETER

Figure 71 PHOTOMICROGRAPHS OF 223 PAN, CVD 427-HS2

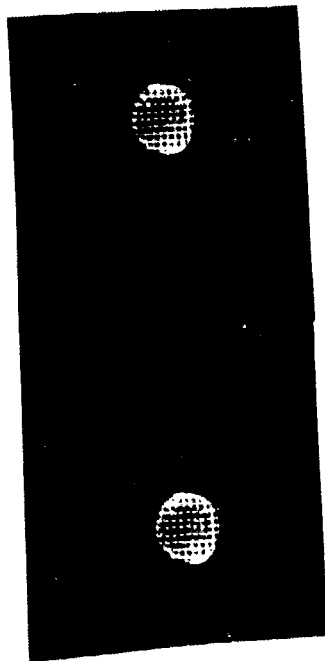


HIGH MAGNIFICATION

MDAC HIP FACILITY • 7ATM
STEADY STATE
BILLET 427 • 0.28 INCH DIAMETER



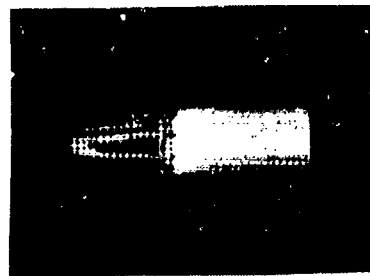
CROSS SECTION



STEREO VIEW



LOW MAGNIFICATION



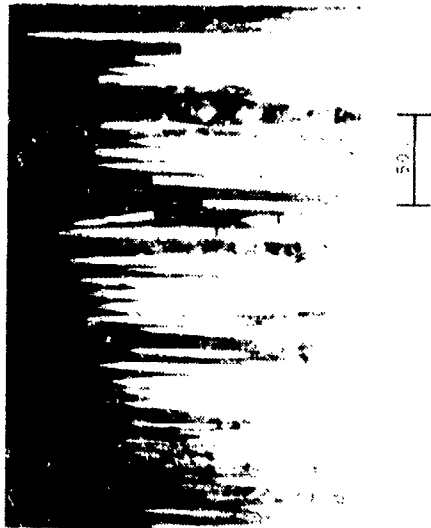
SIDE VIEW

MDAC HIP FACILITY • 7ATM

STEADY STATE

BILLET 668-11 • 0.28 INCH DIAMETER

Figure 72 PHOTOMICROGRAPHS OF 223 PAN,CVD 668-11-HS2



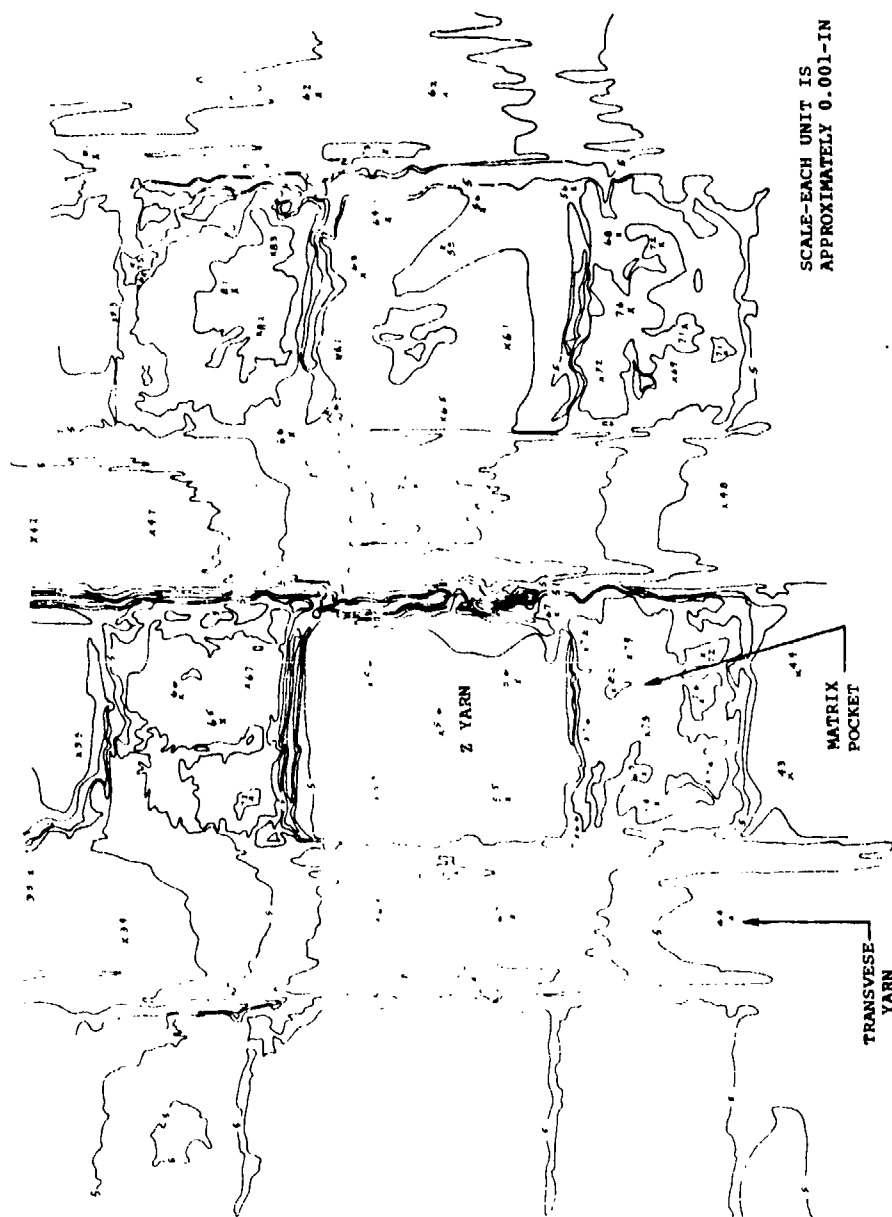
HIGH MAGNIFICATION



MDAC HIP FACILITY • 7ATM

STEADY STATE

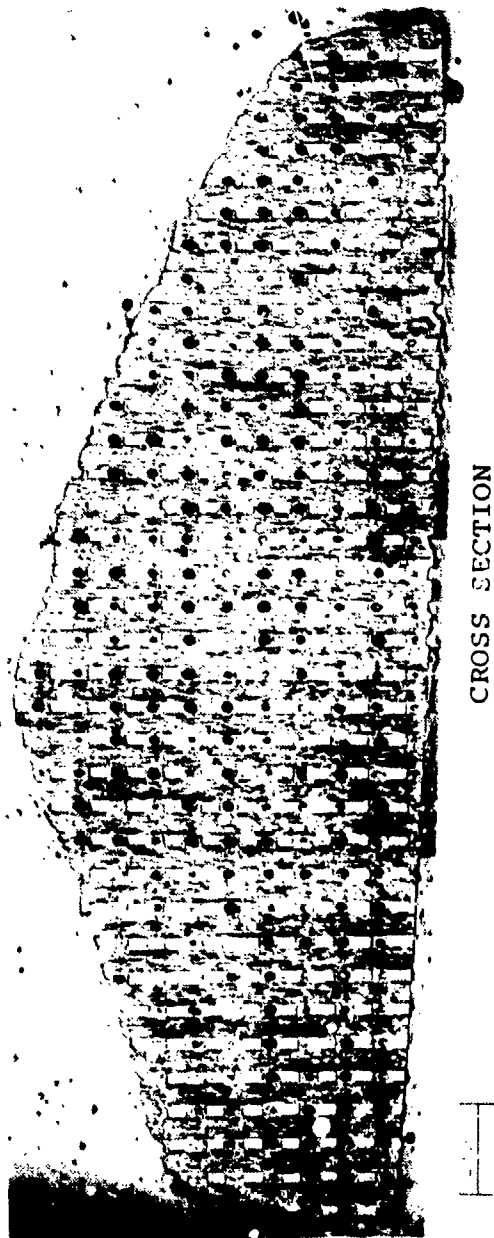
BILLET 668-11 • 0.28 INCH DIAMETER



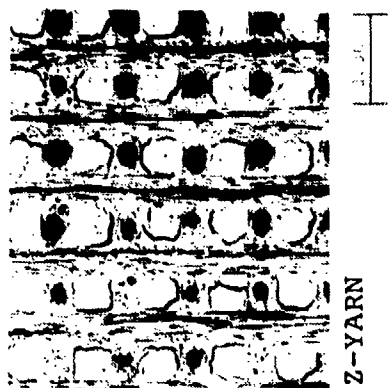
- HIGHEST ELEVATION - MATRIX
- LOWEST ELEVATION - TRANSVERSE YARN BETWEEN MATRIX POCKETS
- TRANSVERSE YARN IS HIGH BETWEEN Z YARNS AND LOW BETWEEN MATRIX POCKETS

MDAC HIP FACILITY - 7ATM
STEADY STATE
BULLET 668-11 - 0.28 INCH DIAMETER

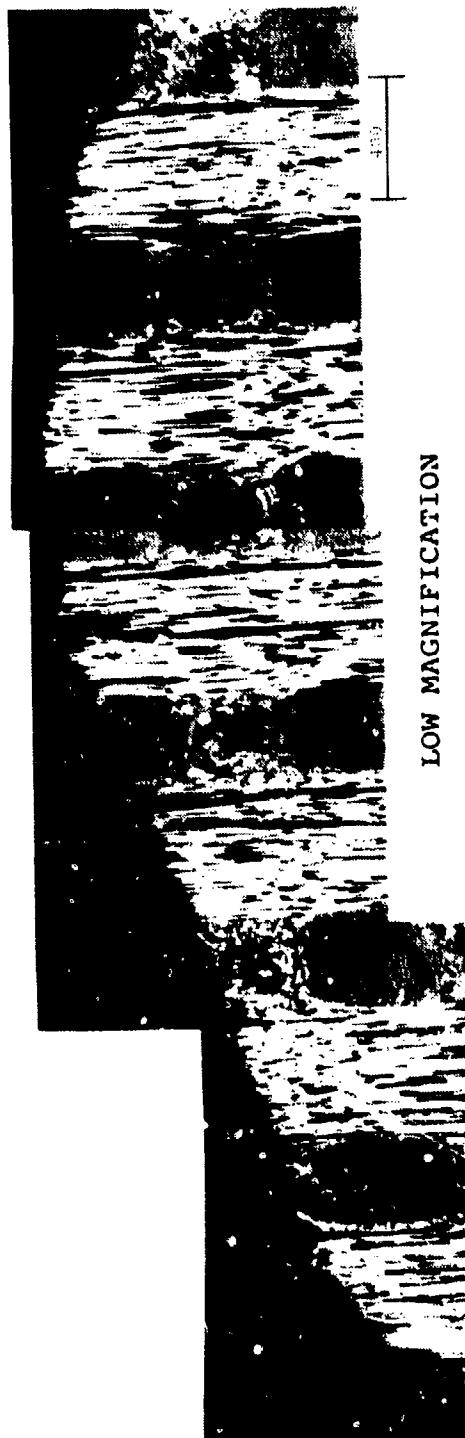
Figure 72 (continued) PHOTOMICROGRAPHS OF 223 PAN, CVD 668-11-HS2



CROSS SECTION

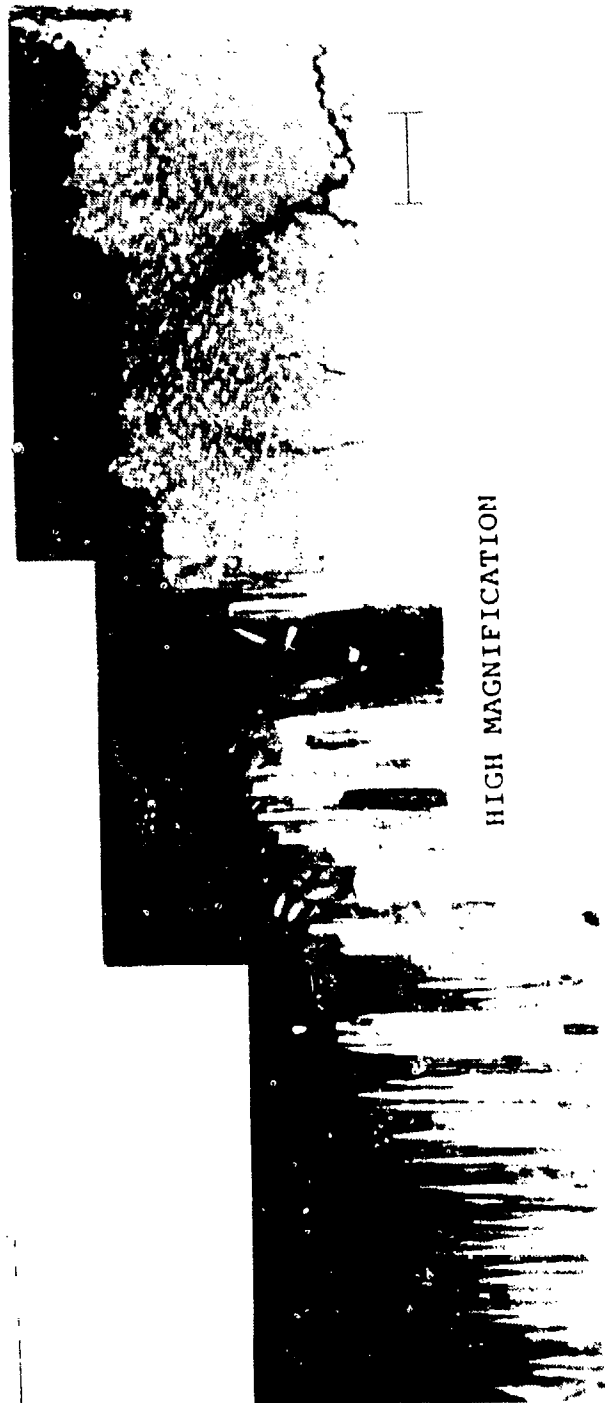


Z-YARN

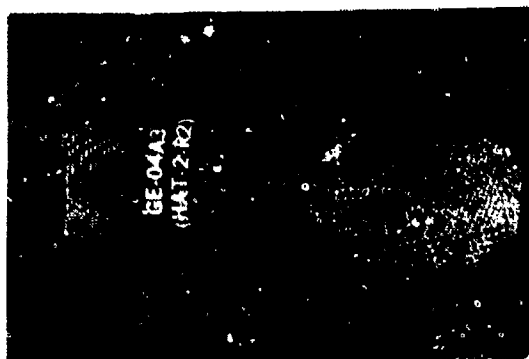


LOW MAGNIFICATION

AFFDL 50 MW . 76 ATM
RAMP, PEAKED ENTHALPY
BILLET HAT-2-R2 . 1.08 INCH DIAMETER



HIGH MAGNIFICATION



SIDE VIEW



STEREO VIEW



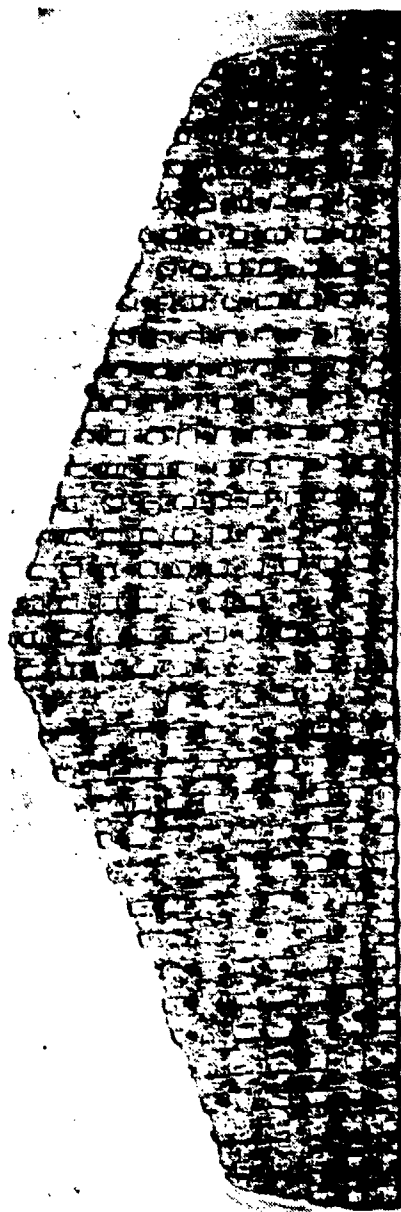
AFFDL 50 MW . 76 ATM
RAMP, PEAKED ENTHALPY

BILLET HAT-2-R2 . 1.08 INCH DIAMETER

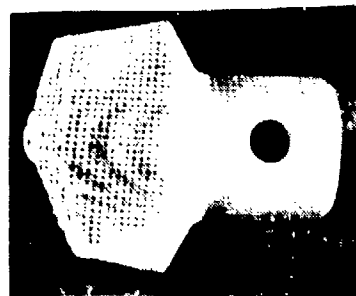
Figure 73 (continued) PHOTOMICROGRAPHS OF 223 PAN, HAT GE-04A3



LOW MAGNIFICATION

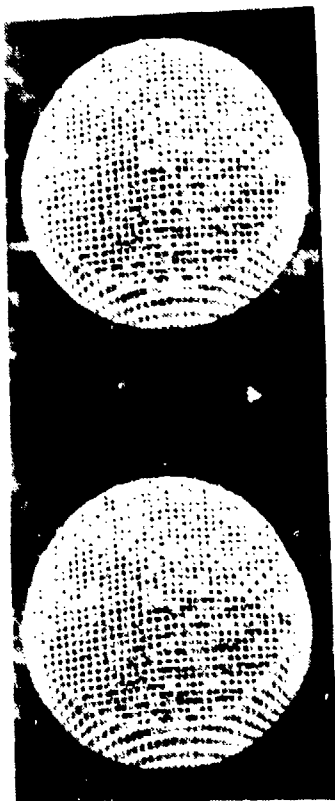


CROSS SECTION

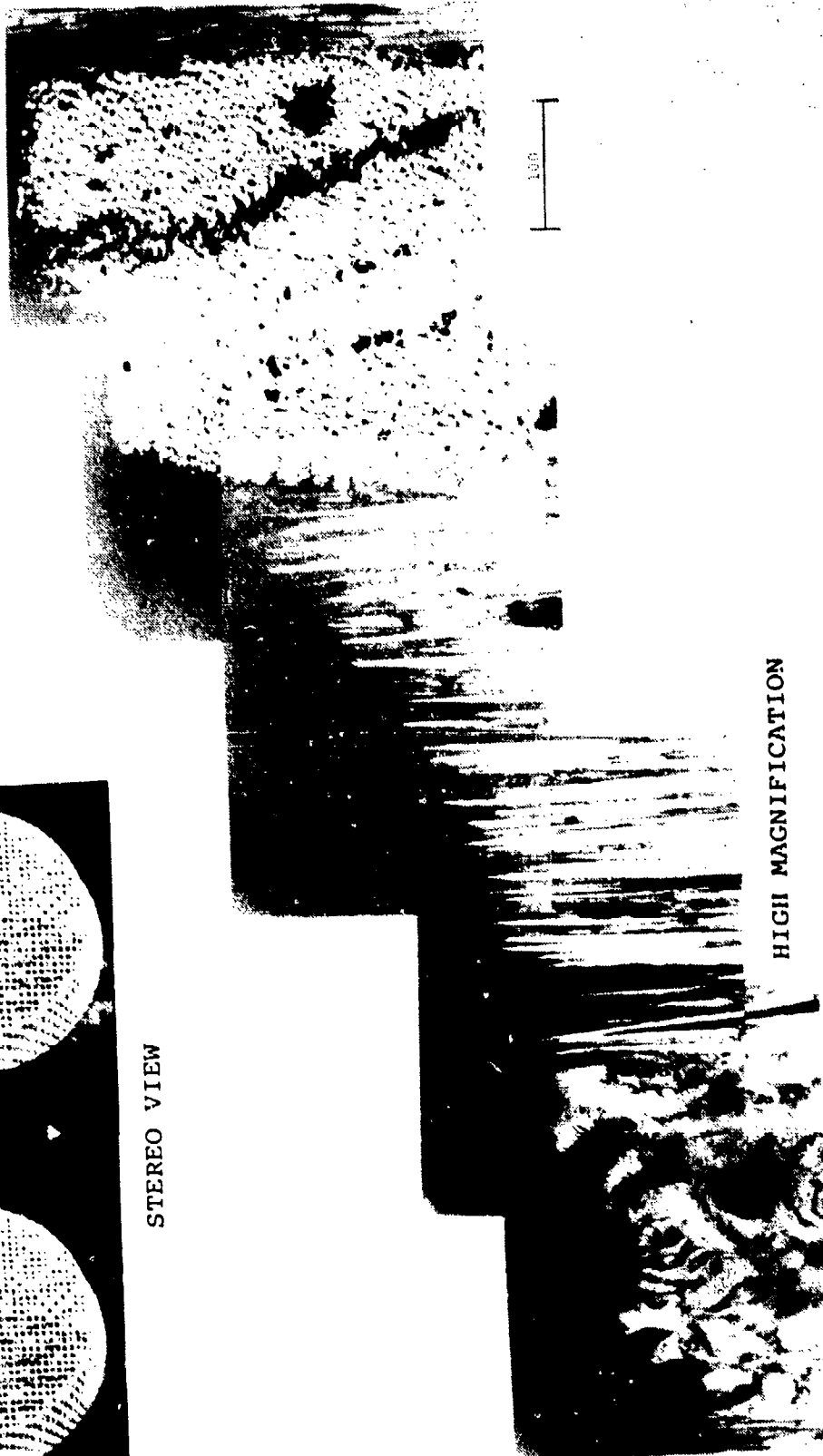


SIDE VIEW

AFFDL 50 MW - 76 ATM
RAMP, PEAKED ENTHALPY
1.03 INCH DIAMETER



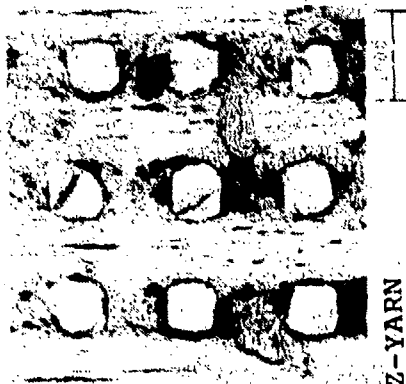
STEREO VIEW



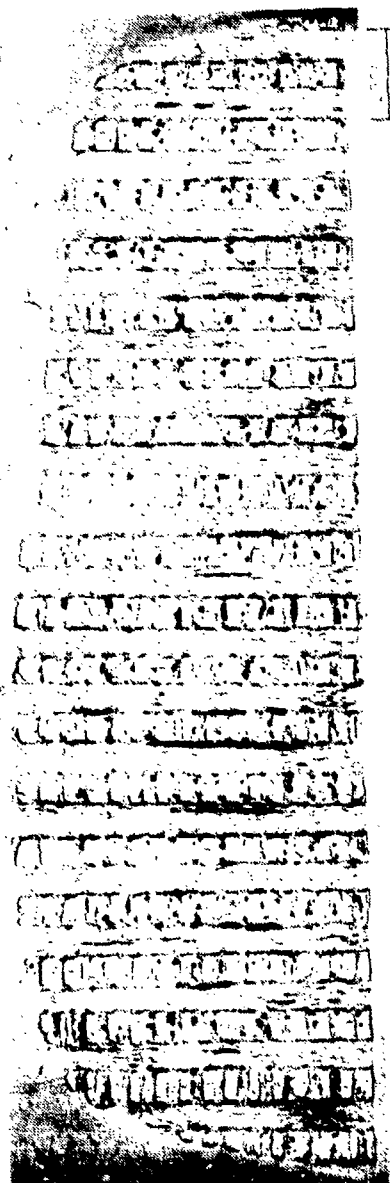
HIGH MAGNIFICATION

AFFDL 50 MW - 76 ATM
RAMP, PEAKED ENTHALPY
1.03 INCH DIAMETER

Figure 74 (continued) PHOTOMICROGRAPHS OF 223 PAN, HAT, 10 KSI PROCESSING HAT 5



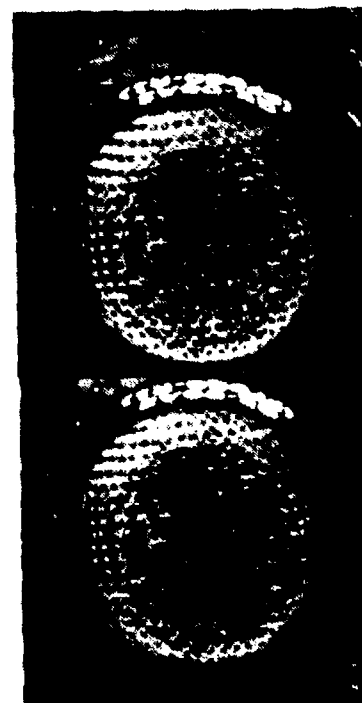
Z-YARN



CROSS SECTION



SIDE VIEW



STEREO VIEW

AFFDL 50 MW · 76 ATM
RAMP, PEAKED ENTHALPY
BILLET PF 920-R1 · 1.03 INCH DIAMETER

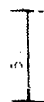
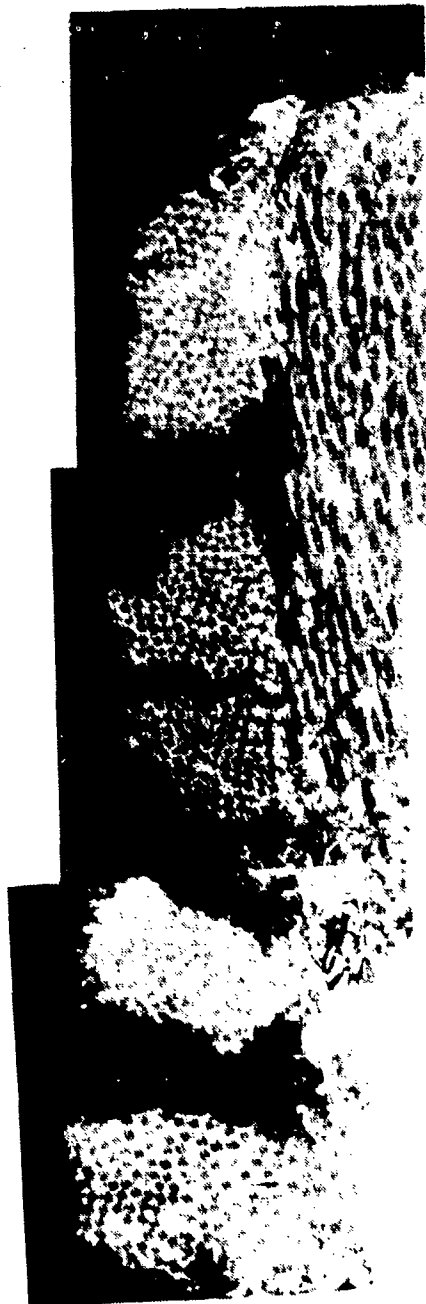


HIGH MAGNIFICATION

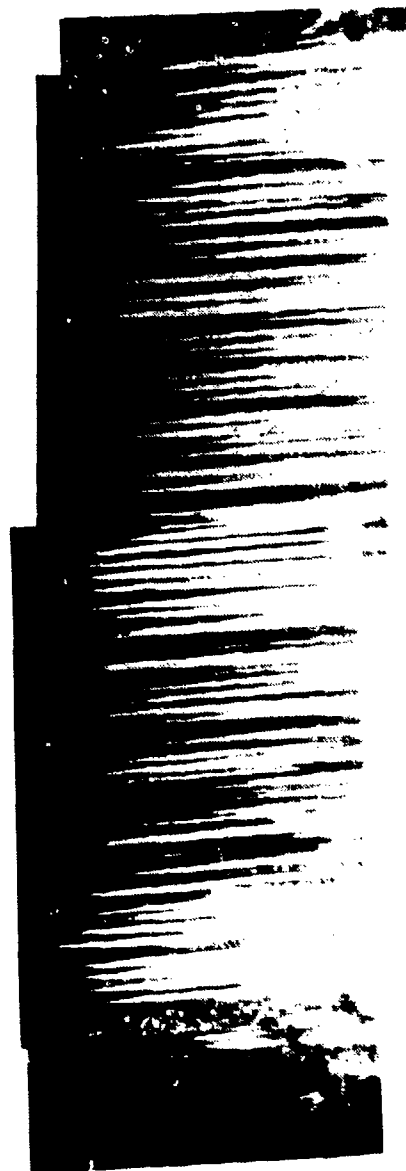


AFFDL 50 MW - 76 ATM
 RAMP, PEAKED ENTHALPY
 BILLET PF 920-R1 - 1.03 INCH DIAMETER

Figure 75 (continued) PHOTOMICROGRAPHS OF FWPF PAN GE-06A3



HIGH MAGNIFICATION



AFFDL 50 MW - 76 ATM

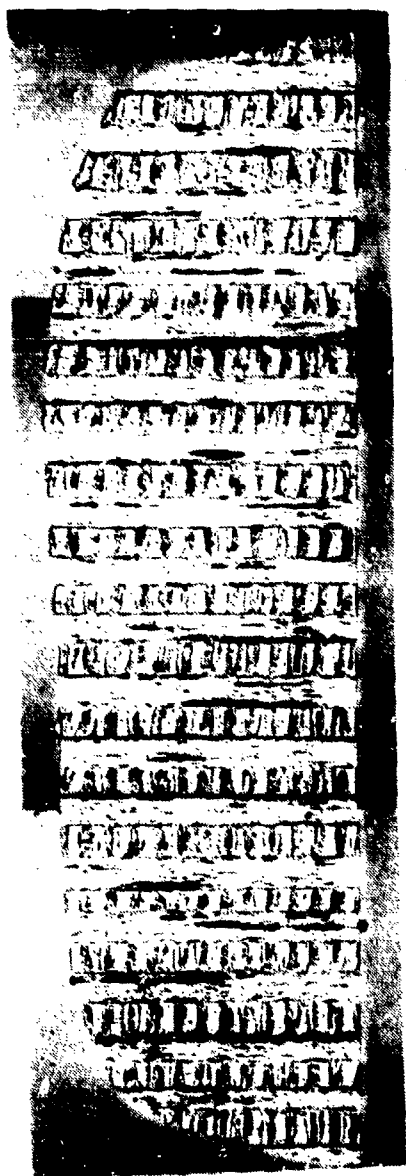
RAMP, PEAKED ENTHALPY

BILLET PF 920-R1 - 1.03 INCH DIAMETER

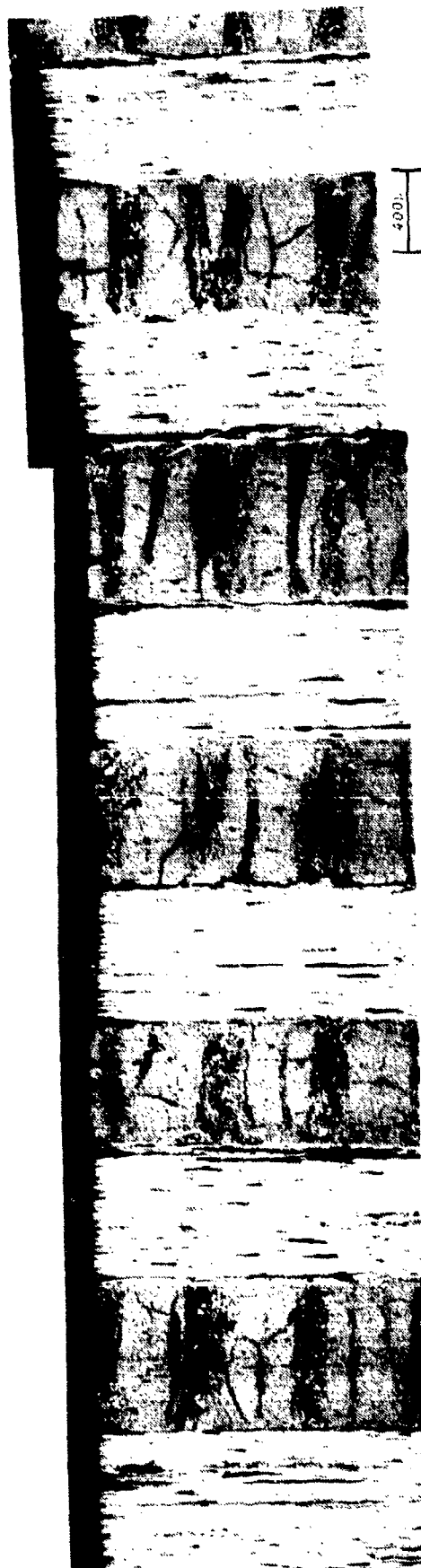
Figure 75 (continued) PHOTOMICROGRAPHS OF FWPF PAN GE-06A3



SIDE VIEW



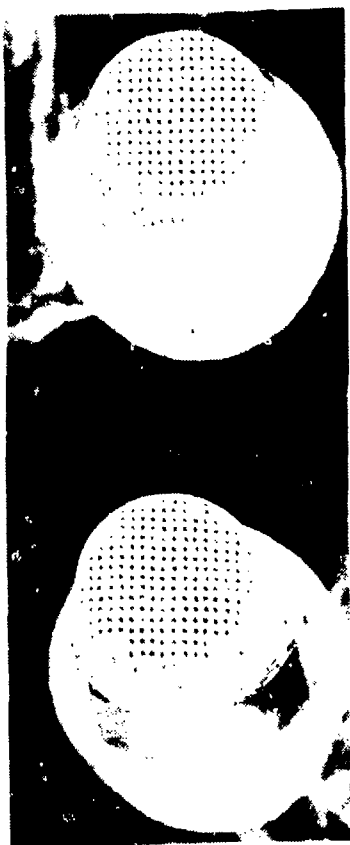
CROSS SECTION



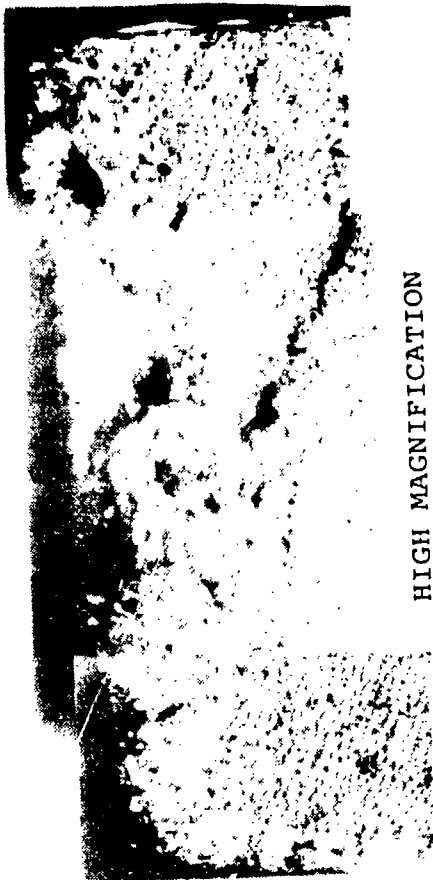
LOW MAGNIFICATION

AFFDL 50 MW · 76 ATM
RAMP, PEAKED ENTHALPY
BILLET PF 928 · 1.00 INCH DIAMETER

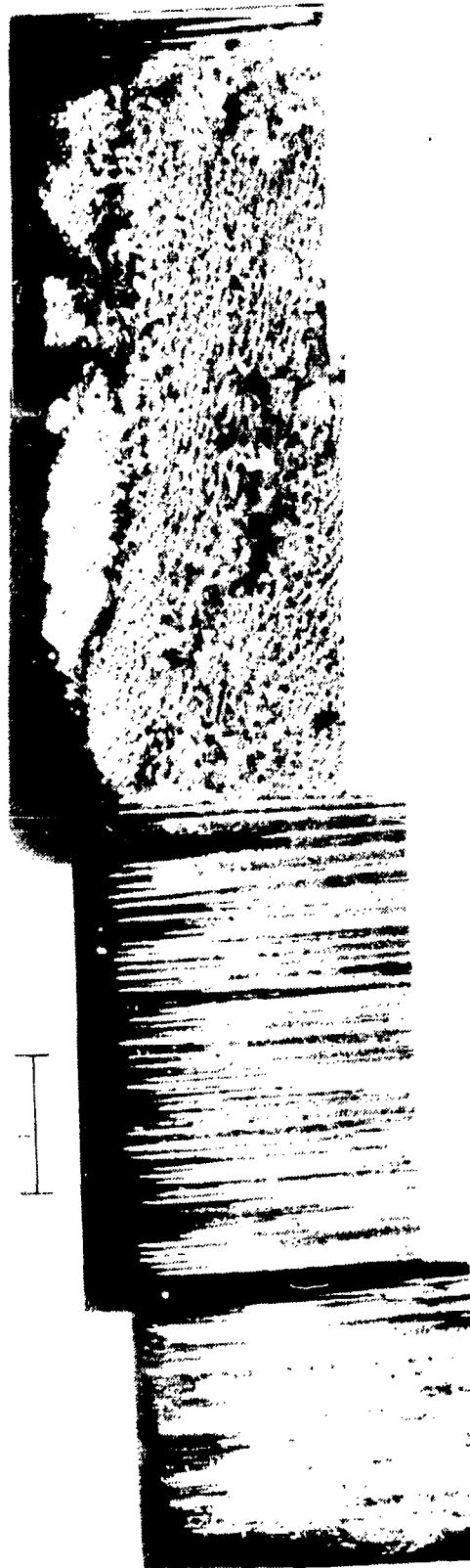
Figure 76 PHOTOMICROGRAPHS OF FWPF PAN GE-02PA



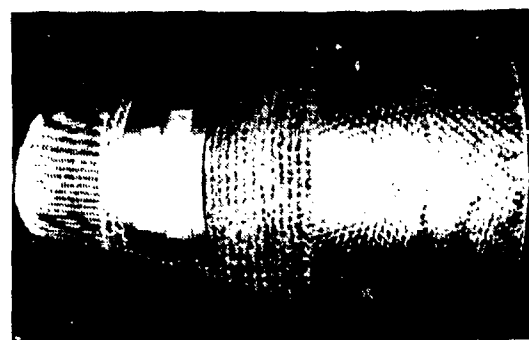
STEREO VIEW



HIGH MAGNIFICATION



AFFDL 50 MW · 76 ATM
RAMP, PEAKED ENTHALPY
BILLET PF 928 · 1.00 INCH DIAMETER



SIDE VIEW



CROSS SECTION

2000.



LOW MAGNIFICATION

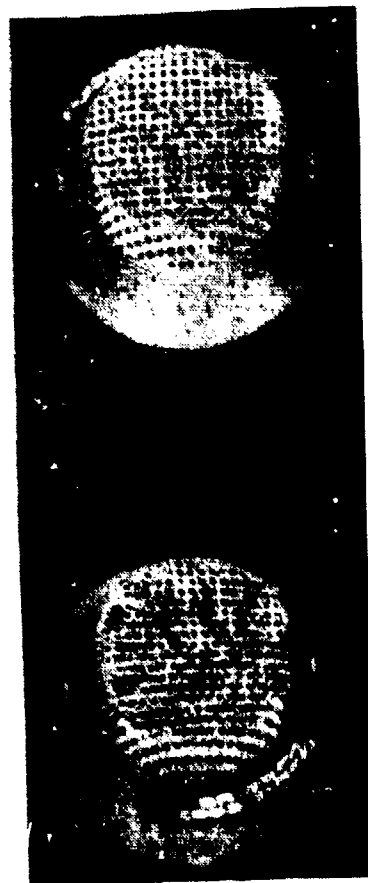
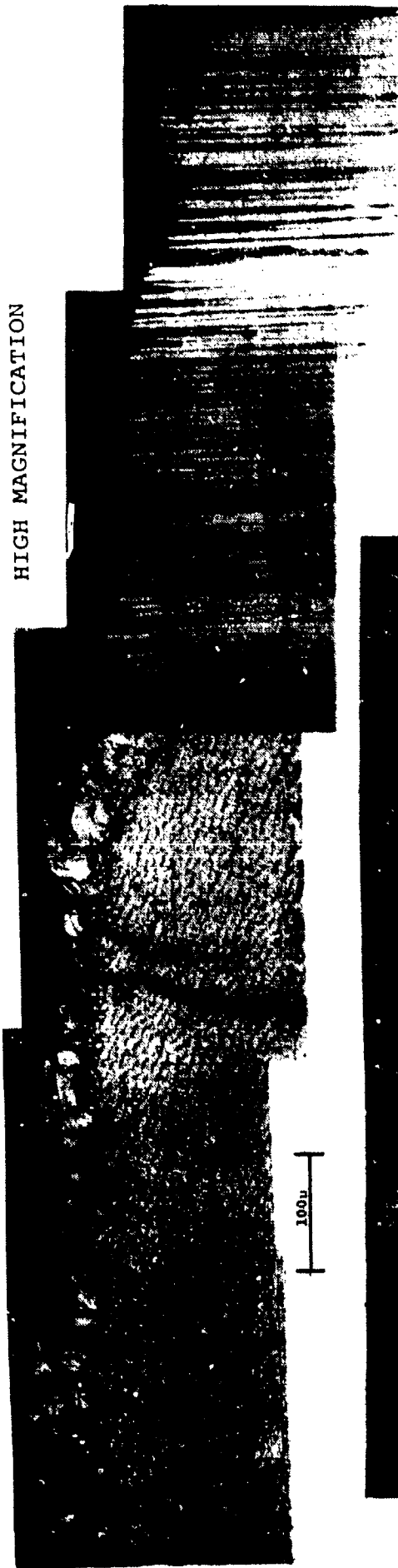
400.

AFFDL 50 MW - 76 ATM
RAMP, PEAKED ENTHALPY

BILLET 903-1-RZ1 - 1.00 INCH DIAMETER

Figure 77 PHOTOMICROGRAPHS OF FWPF PAN SR-25PA

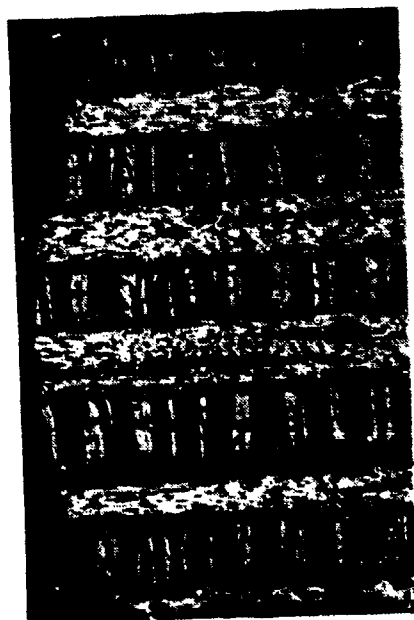
HIGH MAGNIFICATION



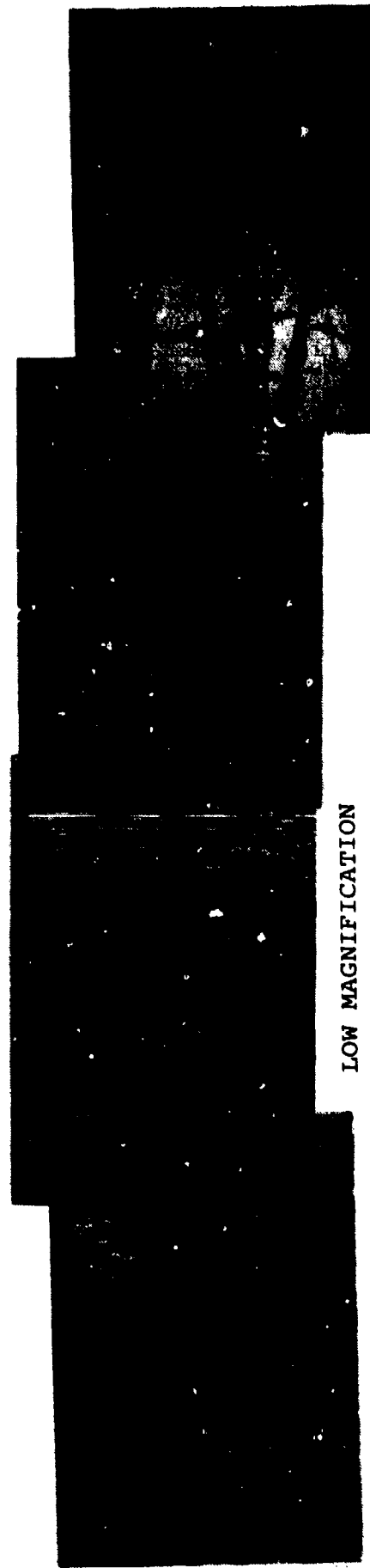
STEREO VIEW

AFFDL 50 MW · 76 ATM
RAMP, PEAKED ENTHALPY
BILLET 903-1-RZ1 · 1.00 INCH DIAMETER

Figure 77 (continued) PHOTOMICROGRAPHS OF FWPf PAN SR-25PA



CROSS SECTION

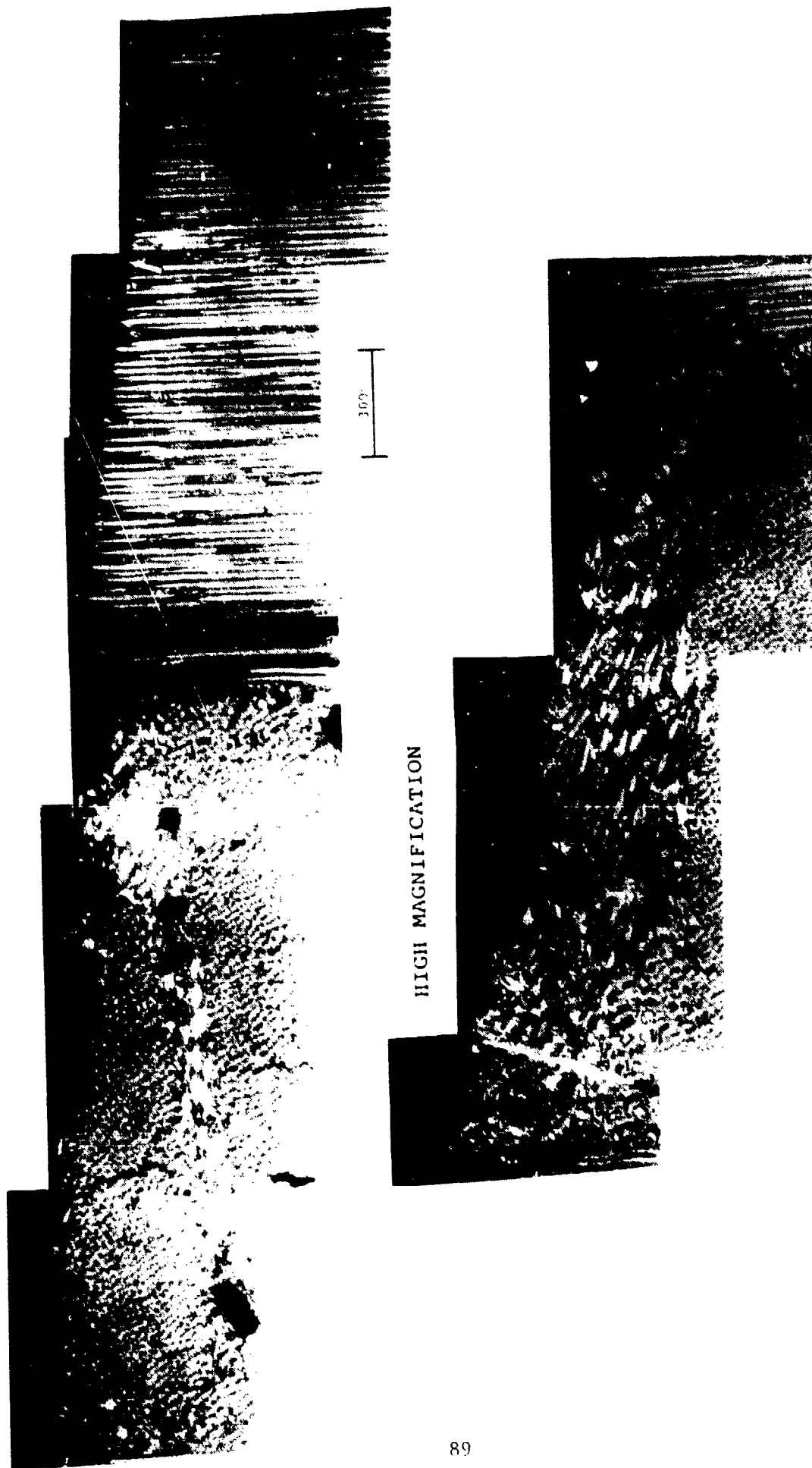


LOW MAGNIFICATION

MDAC HIP FACILITY • 7ATM

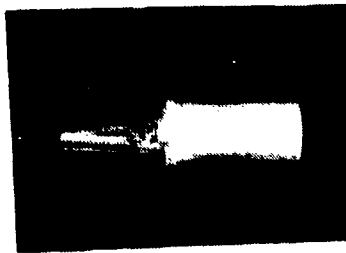
STEADY STATE

BILLET PF 928 • 0.28 INCH DIAMETER

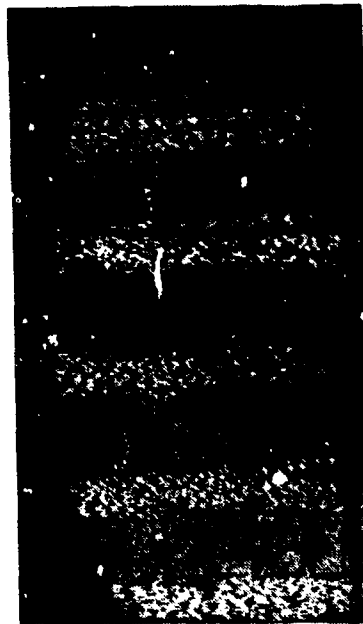


HIGH MAGNIFICATION

MDAC HIP FACILITY • 7ATM
STEADY STATE
BILLET PF 928 • 0.28 INCH DIAMETER



SIDE VIEW



CROSS SECTION

1000μ



LOW MAGNIFICATION

400μ

MDAC HIP FACILITY • 7ATM

STEADY STATE

BILLET PF 928 • 0.28 INCH DIAMETER

Figure 79 PHOTOMICROGRAPHS OF FWPF PAN PF928-HS3



HIGH MAGNIFICATION



MDAC HIP FACILITY - 7ATM

STEADY STATE

BILLET PF 928 - 0.28 INCH DIAMETER

Figure 79 (continued) PHOTOMICROGRAPHS OF FWPF PAN PF928-HS3



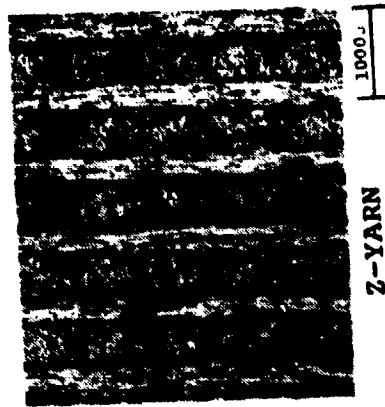
HIGH MAGNIFICATION

MD/C HIP FACILITY • 7ATM

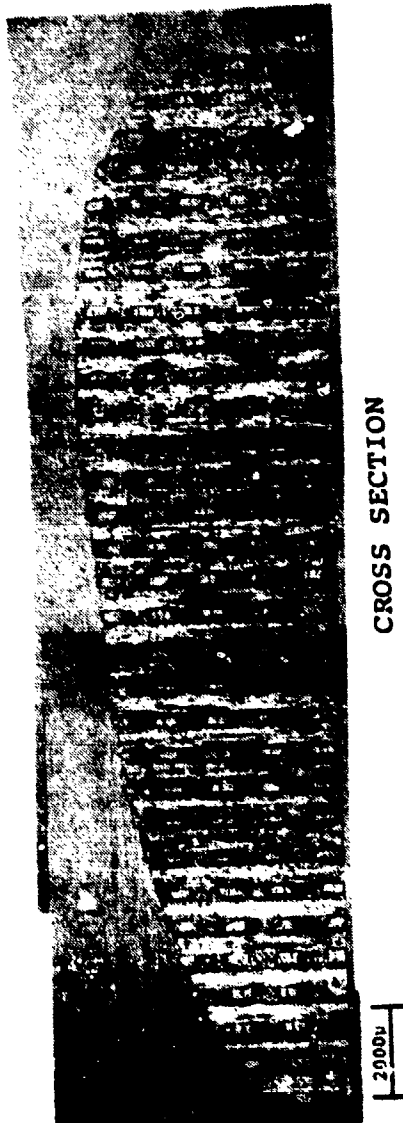
STEADY STATE

BILLET PF 928 • 0.28 INCH DIAMETER

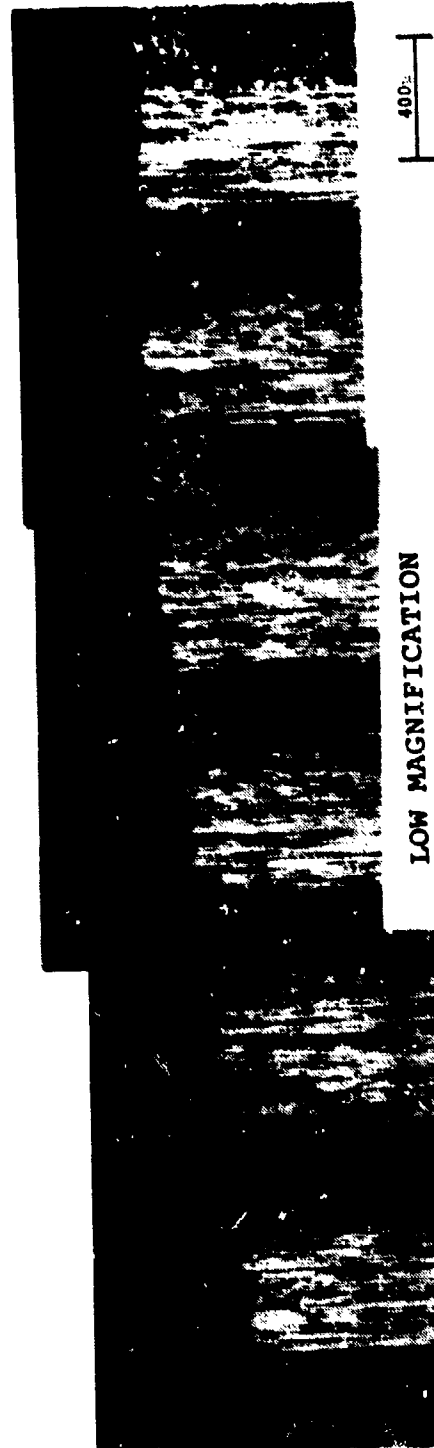
Figure 79 (continued) PHOTOMICROGRAPHS OF FWPF PAN PF928-HS3



Z-YARN



CROSS SECTION

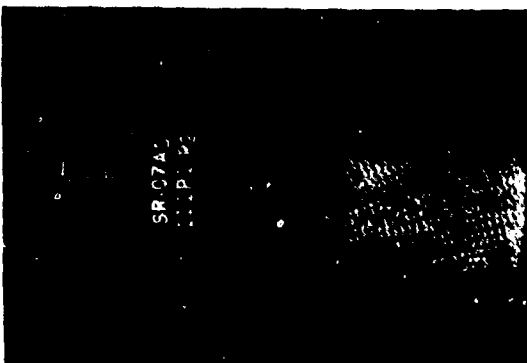


LOW MAGNIFICATION

AFFDL 50 MW · 76 ATM
RAMP, PEAKED ENTHALPY

BILLET 111P1-R2 · 0.95 INCH DIAMETER

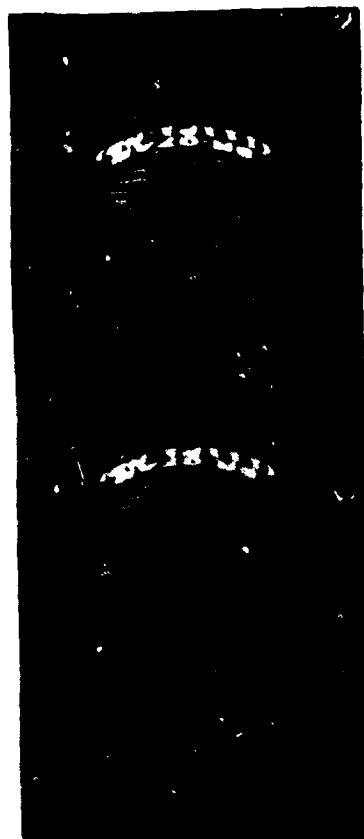
Figure 80 PHOTOMICROGRAPHS OF PITCH, no CVD SR-07AD



SIDE VIEW

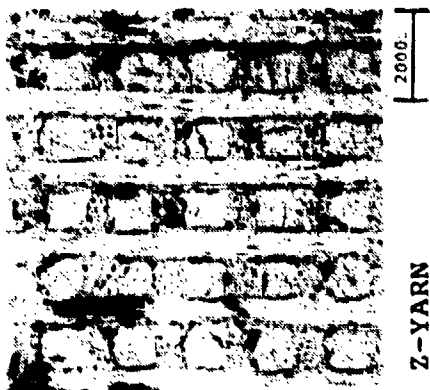


HIGH MAGNIFICATION

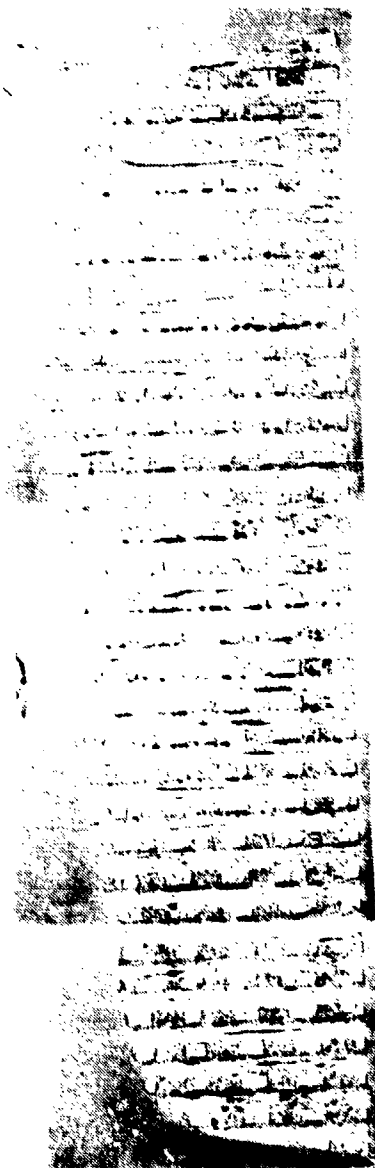


STEREO VIEW

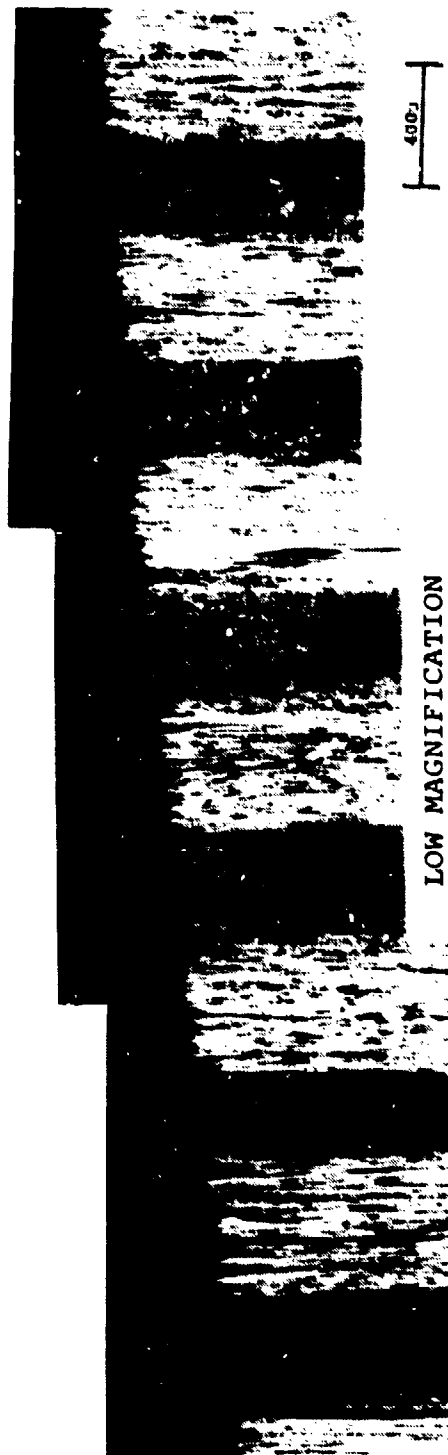
APFEL 50 MW - 76 ATM
 RAMP, PEAKED ENTHALPY
 Figure 80 (continued) PHOTOMICROGRAPHS OF PITCH, no CVD SR-07AD BILLET 111P1-R2 - 0.95 INCH DIAMETER



Z-YARN



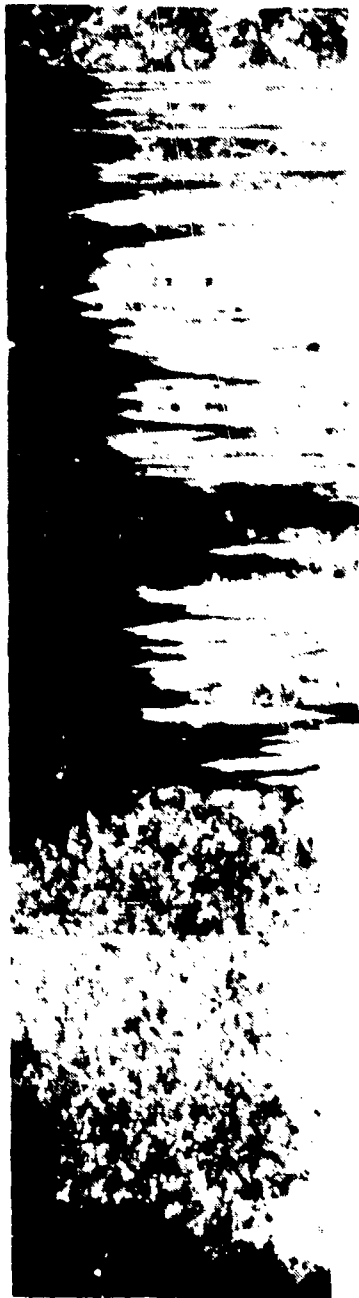
CROSS SECTION



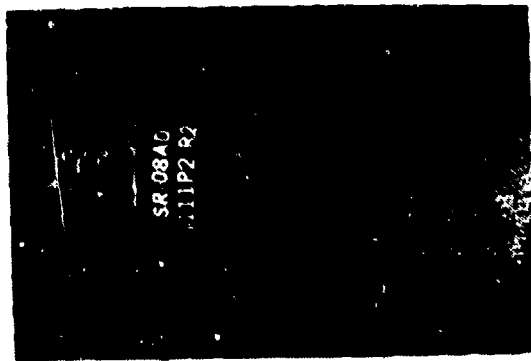
LOW MAGNIFICATION

AFFDL 50 MW - 76 ATM
RAMP, PEAKED ENTHALPY

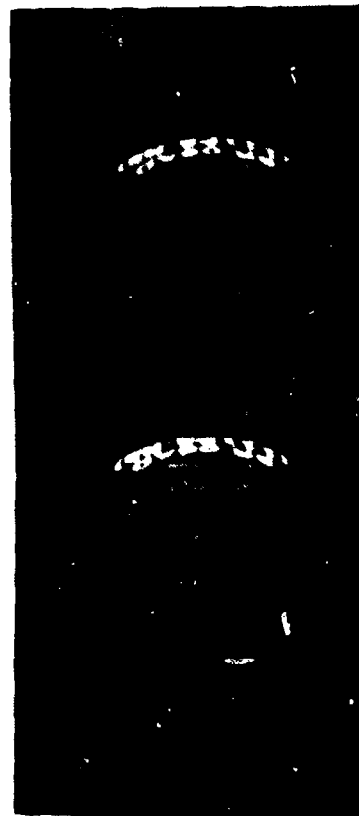
BILLET 111P2-R2 - 1.00 INCH DIAMETER



HIGH MAGNIFICATION



SIDE VIEW



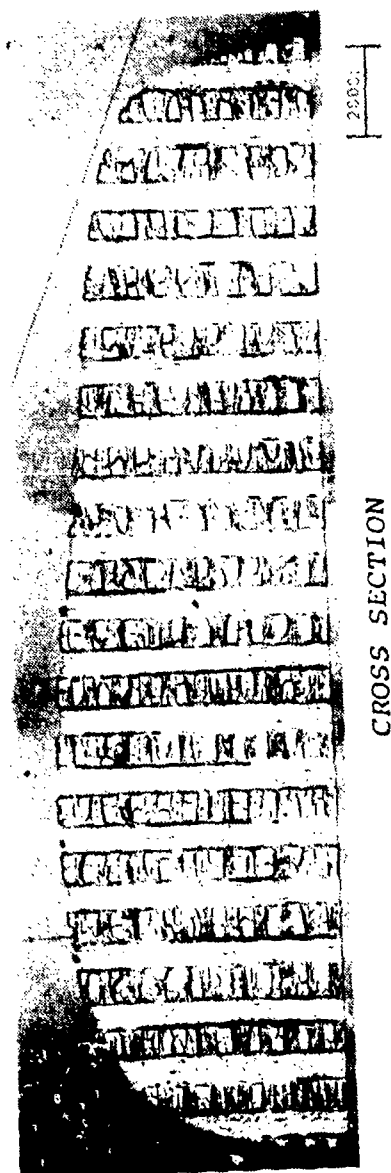
STEREO VIEW

APFDL 50 MW - '76 ATM
RAMP, PEAKED ENTHALPY
BILLET 111P2-R2 - 1.00 INCH DIAMETER

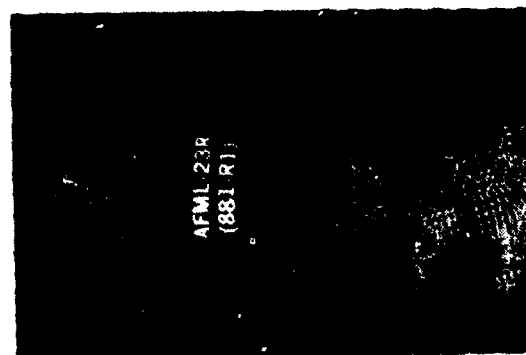
Figure 81 (continued) PHOTOMICROGRAPHS OF PITCH WITH CVD SR-08AD



Z-YARN



CROSS SECTION



SIDE VIEW

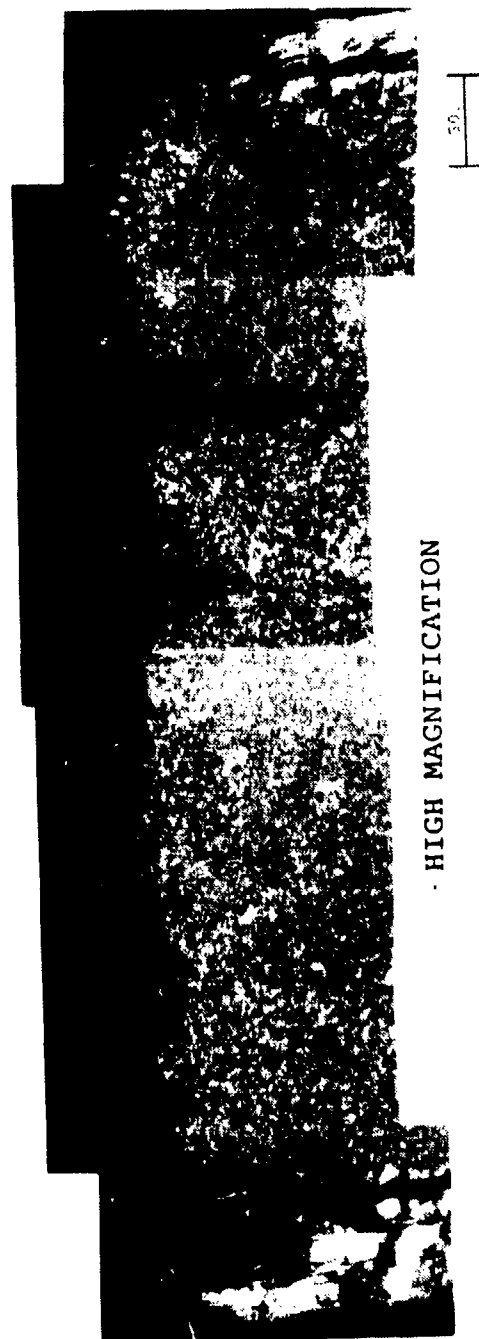
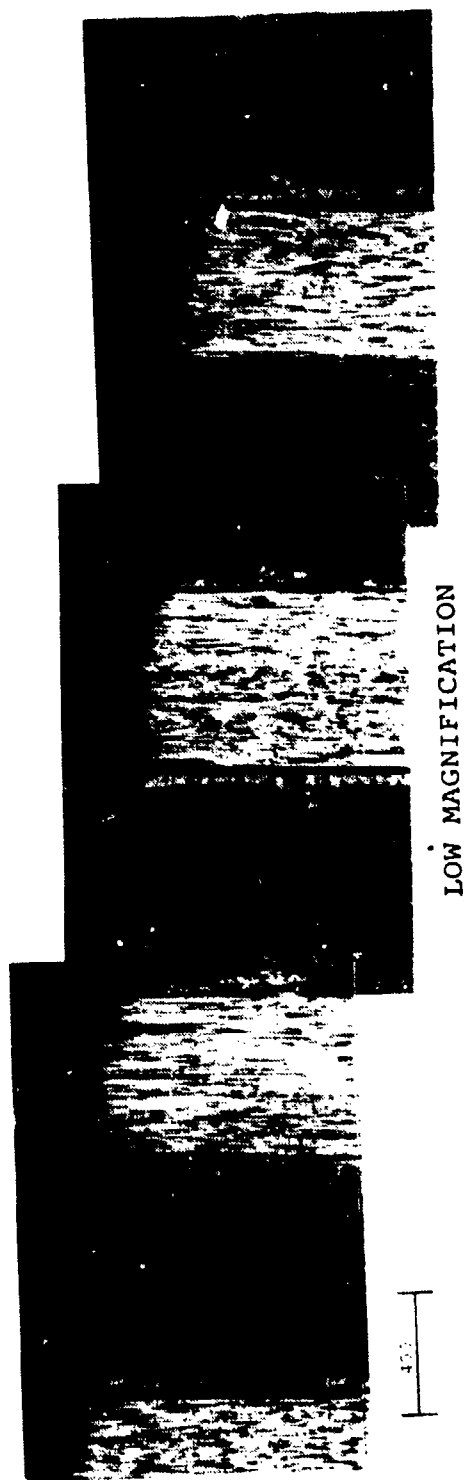


STEREO VIEW

AFDDL 50 MW · 76 ATM

RAMP, PEAKED ENTHALPY

BILLET 881-R1 · 1.00 INCH DIAMETER



AFD L 50 MW · 76 ATM

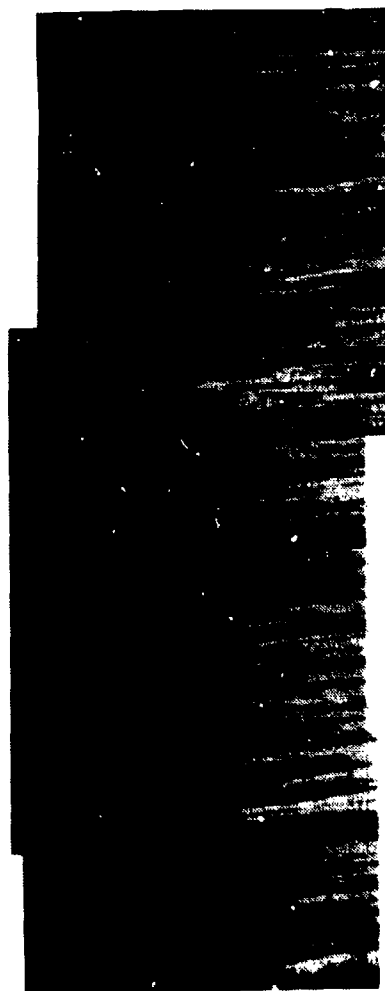
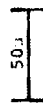
RAMP, PEAKED ENTHALPY

BILLET 881-RI · 1.00 INCH DIAMETER

Figure 82 (continued) PHOTOMICROGRAPHS OF FWP T-50, LOPIC AFML-23R



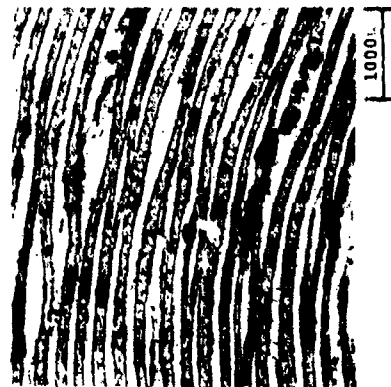
HIGH MAGNIFICATION



AFDDL 50 MW · 76 ATM
RAMP, PEAKED ENTHALPY
BILLET 881-R1 · 1.00 INCH DIAMETER



LOW MAGNIFICATION



AXIAL DIRECTION VIEW



STEREO VIEW

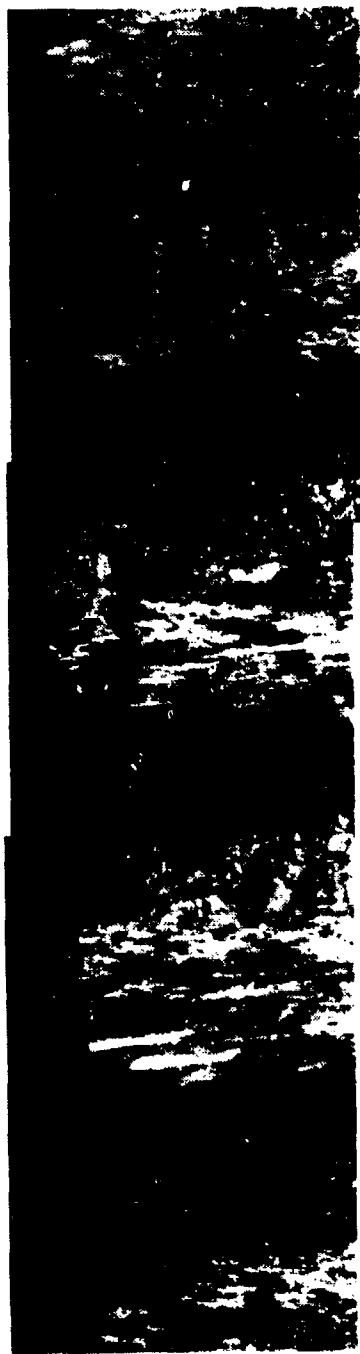


SIDE VIEW

AFFDI 50 MW · 76 ATM
RAMP, PEAKED ENTHALPY

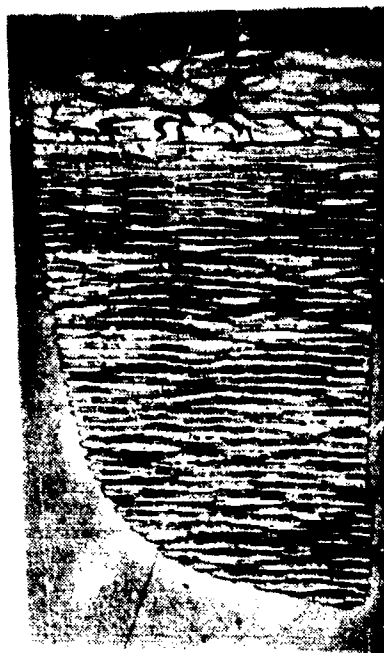
BILLET JR-4-2-R1 · 1.00 INCH DIAMETER

Figure 83 PHOTOMICROGRAPHS OF JELLYROLL AFML-19R



50μ

HIGH MAGNIFICATION

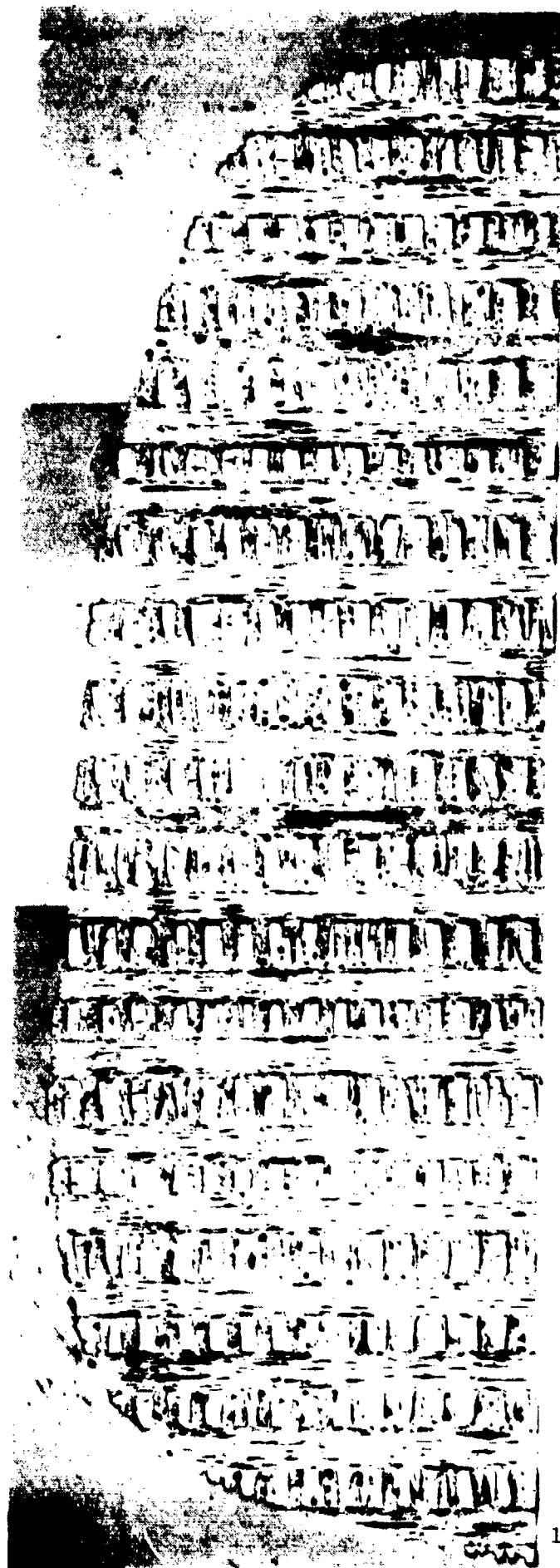


2000μ

CROSS SECTION

AFFDL 50 MW · 76 ATM
RAMP, PEAKED ENTHALPY

BILLET JR-4-2-R1 · 1.00 INCH DIAMETER



CROSS SECTION

2000μ

AFFDL 50 MW · 76 ATM

RAMP, PEAKED ENTHALPY

BILLET 921-R2 · 1.03 INCH DIAMETER

Figure 84 PHOTOMICROGRAPHS OF FWPF PAN AC-02N



2000μ

CROSS SECTION

AFDDL 50 MW · 76ATM
RAMP, PEAKED ENTHALPY
BILLET 921-R7 · 1.02 INCH DIAMETER
AC-03N FWPF PAN

Figure 84 (continued)

2.4 Ablation Model Observations

2.4.1 Yarn Effects on Matrix Microstructure (Figure 73 - 223 HAT, Figures 80 and 81 - pitch yarn). The 223 HAT material was a composite fabricated without CVD and processed at 10 KSI to provide a microstructure which typically transitions at high altitudes. This material, as expected, had large pores in the matrix pockets which were uniform throughout the sections examined. Its surface roughness was also approximately twice that of a standard 223 material, which had transistioned during a peaked enthalpy test (1.56 vs .83 mils equivalent sand roughness). An interesting comparison, however, can be made between this material, which was processed at 10 KSI, and the pitch-yarn materials, which were processed at 5 KSI. In view of the lower processing pressure, it would be expected that a similar microstructure with large pores would also develop in the pitch-yarn materials. However, the pitch-yarn materials have a matrix pore structure which is more typical of higher pressure processed materials (15 KSI) rather than the large pores associated with low pressure processing. A careful examination of these matrix pockets indicates that filaments have been frayed, or spalled, from the pitch-yarns during processing and are located in the matrix pockets. These filaments are probably the major cause for the fine porosity in the microstructure, since they provide a substrate for matrix formation.

2.4.2 Processing Facility Effects at Y-12 and MDAC - Three standard GE 223 models scheduled for flight tests and densified by two different processors were examined. The two processors were Union Carbide (Y-12) and MDAC. There appears to be a fairly significant difference between these pieces of material. An examination of the data shows that the permeability coefficients for models GE-07A and GE-01A (Y-12) were 101.4 \AA and 96.58 \AA respectively. While earlier data (Reference 5) shows that a

permeability coefficient (in the range of 43 Å to 92 Å) is not uncharacteristic of material processed at Y-12, both of these values are high, even for Y-12. In addition, both of the models from material processed Y-12 transitioned in ground tests which is uncharacteristic of standard GE 223. Model GE-07A, which had the highest permeability coefficient, showed more complete transition than did model GE-01A which is consistent with the correlation between high permeability and early transition noted in reference 5. The ablation models also showed extremely high preferential erosion of axial yarns, thereby leading to a macroroughness greater than any seen heretofore in GE 223. The model which was made from MDAC-processed material (GE-02A3) had a permeability coefficient of 65 Å, which is typical of standard GE 223 material. Also, it did not display the large preferential axial yarn erosion observed in the Y-12 processed material. It should also be noted that larger microroughness heights were found in the axial yarn ends of the MDAC material than in the Y-12 material. This is the opposite of what would normally be expected since larger microroughness heights imply earlier transition to turbulent flow. The fact that, for both materials, the axial yarns receded significantly below the surface may be important. If this recession was enough to remove the axial yarns from the flowfield, then the roughness of the other composite constituents would govern transition behavior. Of the remaining constituents, (matrix and transverse yarn), the only differences in matrix roughness were found with the Y-12 material being approximately 20% rougher than the MDAC material.

2.4.3 CVD Effects - (Figures 65, 66, 67) The effect of pre-form prestiffening was investigated on three 223 PAN models processed by MDAC. One of the materials had no CVD (Figure 65),

another had an initial low pressure carbonization (Figure 66), and the third had initial CVD with low temperature graphitization throughout processing (Figure 67). Both of the materials without CVD were similar in nature, even though one had an initial low pressure process cycle. The material with the initial low pressure processing cycle had approximately the same roughness character as the material which was all high pressure processed. The biggest differences between these two materials were in the amount of large porosity and in the permeability coefficients. A larger amount of porosity and a higher permeability coefficient were found in the material with initial low pressure processing. This higher permeability was consistent with the macrostructural observation that a large number of yarns were cracked on at least three sides. Both of the materials without CVD had few pores in the yarn bundles while the material with CVD exhibited extensive porosity in each yarn bundle cross-section. The material with CVD also displayed less differential erosion at the surface between each of the composite constituent phases.

2.4.4 Axially Symmetric Weave Geometries - (Figure 83) One new material, the AVCO "Jellyroll", was characterized after ground test. The model retained a laminar configuration throughout the peaked enthalpy test in spite of the fact that it exhibited a large macroroughness in cross-section. Microroughness measurements could not be made on this material due to the unusual character of its surface. It can only be surmised that the closed cell character formed through differential erosion between the reinforcement layers resulted in a configuration which did not influence the boundary layer sufficiently to cause transistion to turbulent flow conditions. Analysis of flow conditions over this type of surface may provide insight into the nature of this behavior, as well as influence the selection of

specimens for examination taken from other materials. If a closed cavity consideration is necessary, then perhaps more emphasis should be placed on modeling surface geometries in transistion modeling efforts.

2.4.5 Topographical Mapping of Ablation Models - (Figure 72)

A surface map was made of a 223 PAN laminar ablation model to compare surface characteristics with those deduced using plane section observations under the microscope. Stero pair scanning electron micrographs were used in constructing this surface map along with standard aerial map making machines. The mapping shows that yarns which lie parallel to the surface (X, Y Yarns) have varying amounts of recession related to the constituent material adjacent to the yarn. In the location examined, the transverse yarns eroded less than the axial yarns (Z yarns) and more rapidly than the matrix pockets. The axial yarns appeared to recede slightly more than matrix pockets, but the differential recession between the axial yarns and matrix pockets appeared to be on the order of only 0.001 inches. However, there were much larger differences between transverse yarn recessions and their nearest neighbor. Where the transverse yarn ran between two matrix pockets, its recession was significantly greater than the matrix pocket recession. This implies that each composite constituent is affected by the performance of its nearest neighbor. If this is indeed the case, then more extensive mapping would be required for obtaining sufficient data on this interactive behavior for input into modeling activities.

3.0 EROSION MODEL CHARACTERIZATION

A series of carbon-carbon specimens which had been subjected to erosion ground test were evaluated in this effort. Both standard GE 223 and 223 PAN were examined to compare their microstructural response in various ground test environments, Facility effects, particle velocity, and particle type were all addressed. Several of these specimens were also being studied under subcontract to California Research and Technology in support of modeling efforts on a program entitled Multiple Impact Modeling of Composites (AFML Contract F33615-78-C-5059).

One of the primary motivations for this work was that sections of samples which had been tested in Track G (ballistic range) exhibited a character completely different than that experienced in single particle impact testing. The ballistic range models showed a distinct lack of the type of subsurface damage commonly found in the microstructure of single particle impact specimens. The potential mechanisms for the lack of damage were:

1. Loss of material in the recovery tube.
2. Multiple particle impact effects.
3. Particle size effects.
4. Flowfield interaction.
5. Debris shielding.
6. Elevated temperature material response in the ballistic range.

3.1 Single Particle Impact Specimens

A total of 5 samples which had been subjected to single particle impact tests were examined. Three of the samples were standard GE 223 T-50 and two were GE 223 PAN. The initial four samples had been tested using 1000 micron glass beads at both room and elevated temperature. The intent of evaluating these samples was to determine if elevated temperature effects were strong enough to account for the loss of, or inhibition of, the in-

depth damage in the material. The fifth sample was 223 T-50 and was impacted with 350 micron glass beads at three locations to determine if particle size effects significantly altered the in-depth damage. All specimens were examined with cross-sections showing both the axial yarns (yarns parallel to the impact direction) and the transverse yarns (yarns perpendicular to the impact direction).

Cross-sections of the specimens which were impacted with 1000 micron glass beads at room temperature are shown in Figures 85 through 88. The standard 223 material shows considerable in-depth damage immediately below the impact site with extensive crushing at the bottom of the crater. The view with yarns parallel to the impact direction shows both shear failures immediately under the impact site and tensile failures in one yarn immediately to the right of the crater center as evidenced by the separations in the Z yarn. The damage appears much more extensive to the transverse yarns (Figure 86) which were immediately adjacent to the view shown in Figure 85. Yarn damage occurs well beyond the central location of the impact site and approaches the edge of the crater. In some instances there appears to be damage extending out beyond the edge of the crater. In addition there is considerable in-depth deformation of the weave geometry which, upon measuring, extends several unit cells below the readily observable damage. In order to characterize this deformation measurements were made of the space between the transverse yarns immediately below, to the right, and to the left of the impact site (two unit cell measurements to the right and left of the impact site). A plot of the unit cell spacing as a function of depth from the specimen surface is also shown in Figure 86.

The 223 PAN material is shown in Figures 87 and 88. While the damage immediately under the impact site appears much more



Figure 85 CROSS SECTION SHOWING EFFECT OF SINGLE PARTICLE IMPACT AT
ROOM TEMPERATURE ON AXIAL YARNS OF 223 T-50 (1000 μ glass bead,
13.2 kfps, 70°F)

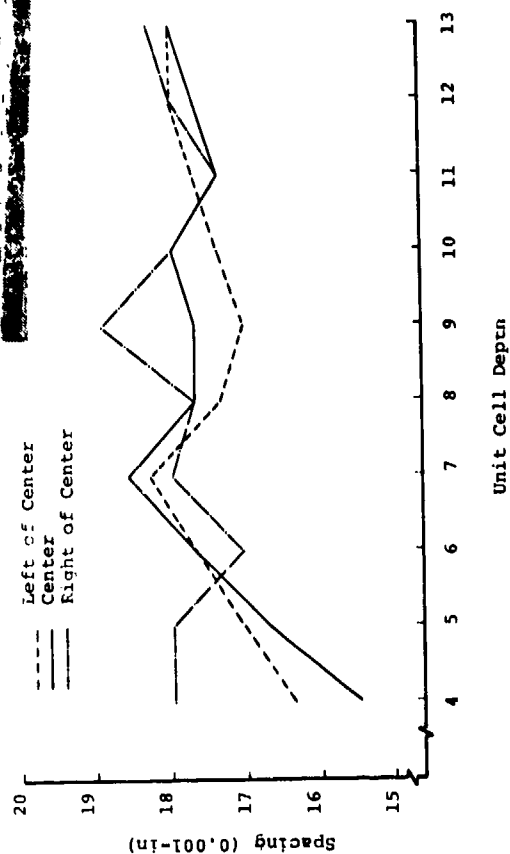
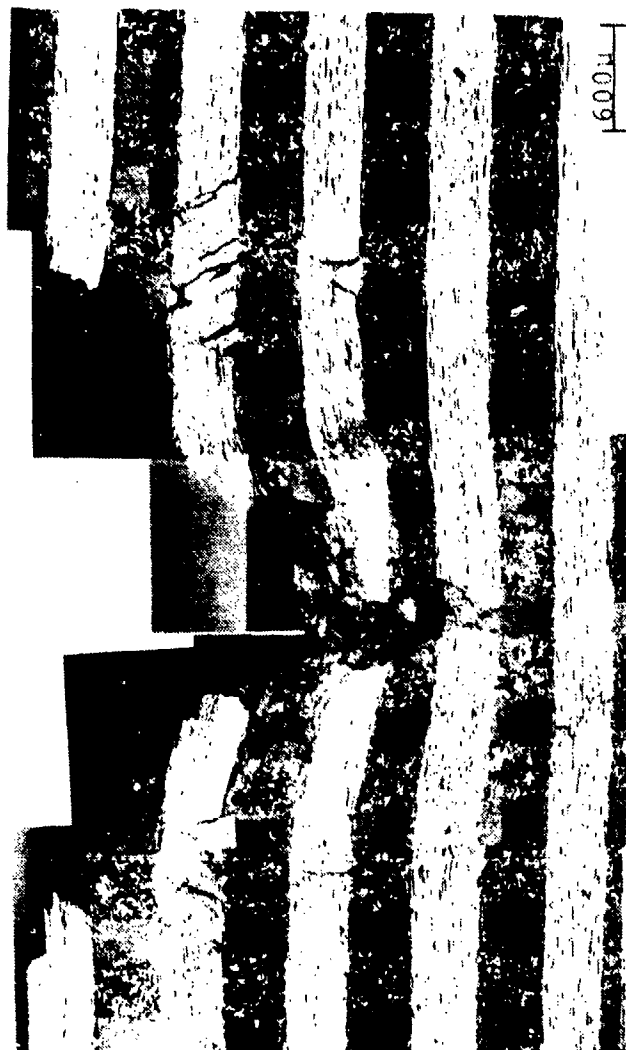


Figure 86 CROSS SECTION SHOWING EFFECT OF SINGLE PARTICLE IMPACT AT
ROOM TEMPERATURE ON TRANSVERSE YARNS OF 223 T-50 (1000μ glass
bead, 13.2 kfps, 70°F)

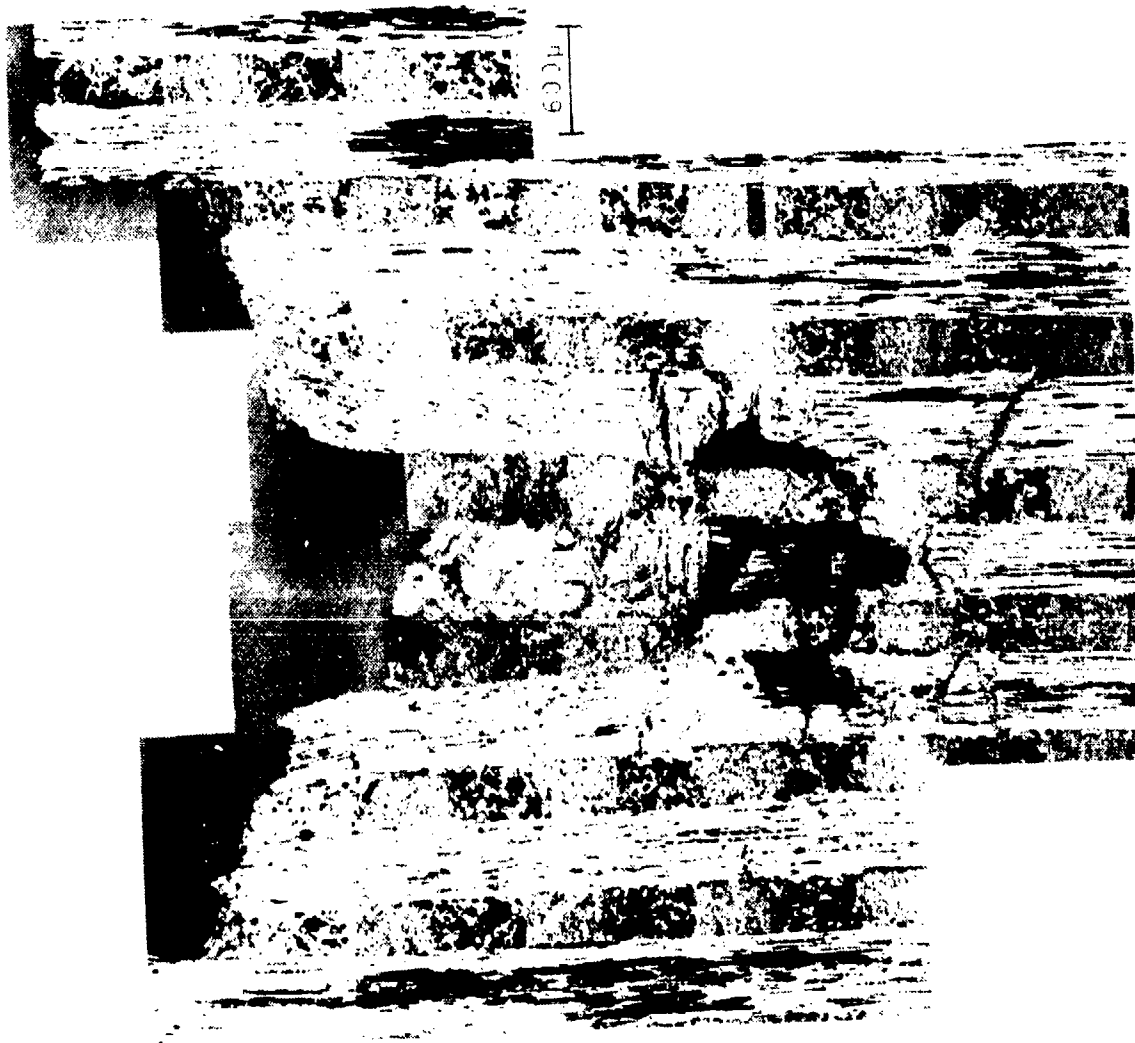


Figure 87 CROSS SECTION SHOWING EFFECT OF SINGLE PARTICLE IMPACT
AT ROOM TEMPERATURE ON AXIAL YARNS OF 223 PAN
(1000 μ glass bead, 18.4 kfps, 70°F)

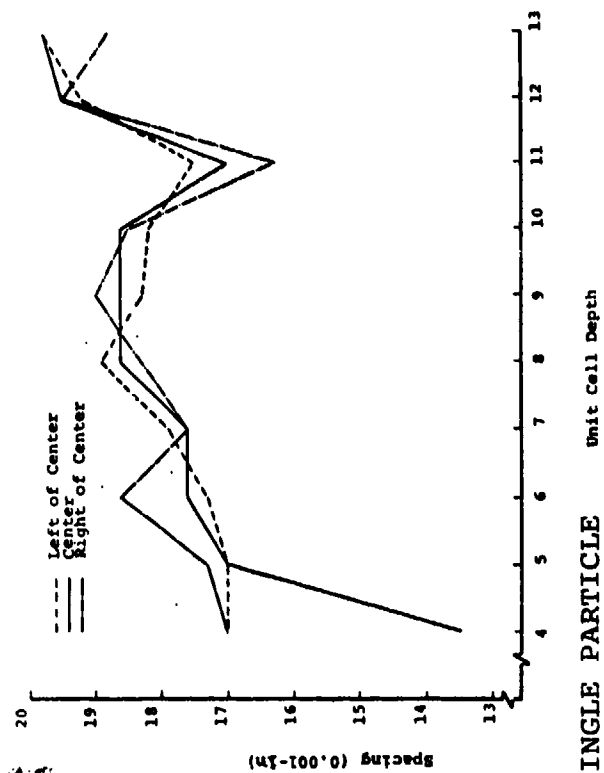


Figure 88 CROSS SECTION SHOWING EFFECT OF SINGLE PARTICLE
IMPACT AT ROOM TEMPERATURE ON TRANSVERSE YARNS
OF 223 PAN (1000 μ glass bead, 18.4 kfps, 70°F)

extensive than for Standard 223 T-50, it should be noted that the velocity of the impacting particle was much higher (18.4 versus 13.2 kfps). As was observed earlier the damage extends further toward the edge of the crater in the transverse section (Figure 88) than in the section with yarns parallel to the impact direction (Figure 87). Similarly a large amount of in-depth weave deformation was measured on this specimen as is shown by the plot included in Figure 88.

The elevated temperature test cross-sections are shown in Figures 89 through 92. The crater in the standard 223 T-50 material appears very similar to the room temperature test when yarns parallel to the impact direction are examined. However there is a great deal of difference in the cross-section with transverse yarns. The most apparent difference is that the yarns at the impact site bow upward toward the crater surface whereas in the room temperature test, which was shown in Figure 86, all of the yarns remained bent downward. In addition the transverse yarns are fractured well beyond the crater edge and deformation appears to have occurred deep in the composite. As with the specimens shown earlier, a plot of yarn spacing as a function of depth from the surface reveals deformation of the geometric structure of the composite well below the area of readily observable damage.

The elevated temperature test on 223 PAN is shown in Figures 91 and 92. Extensive tensile fracture can be observed in the view where yarns are parallel to the impact site. As was found in the standard 223 T-50 material, damage where yarns are transverse has also occurred well beyond the impact zone. Also, the in-depth deformation of the weave structure extends further than that experienced in the other specimens as is seen by the plot shown on Figure 92.

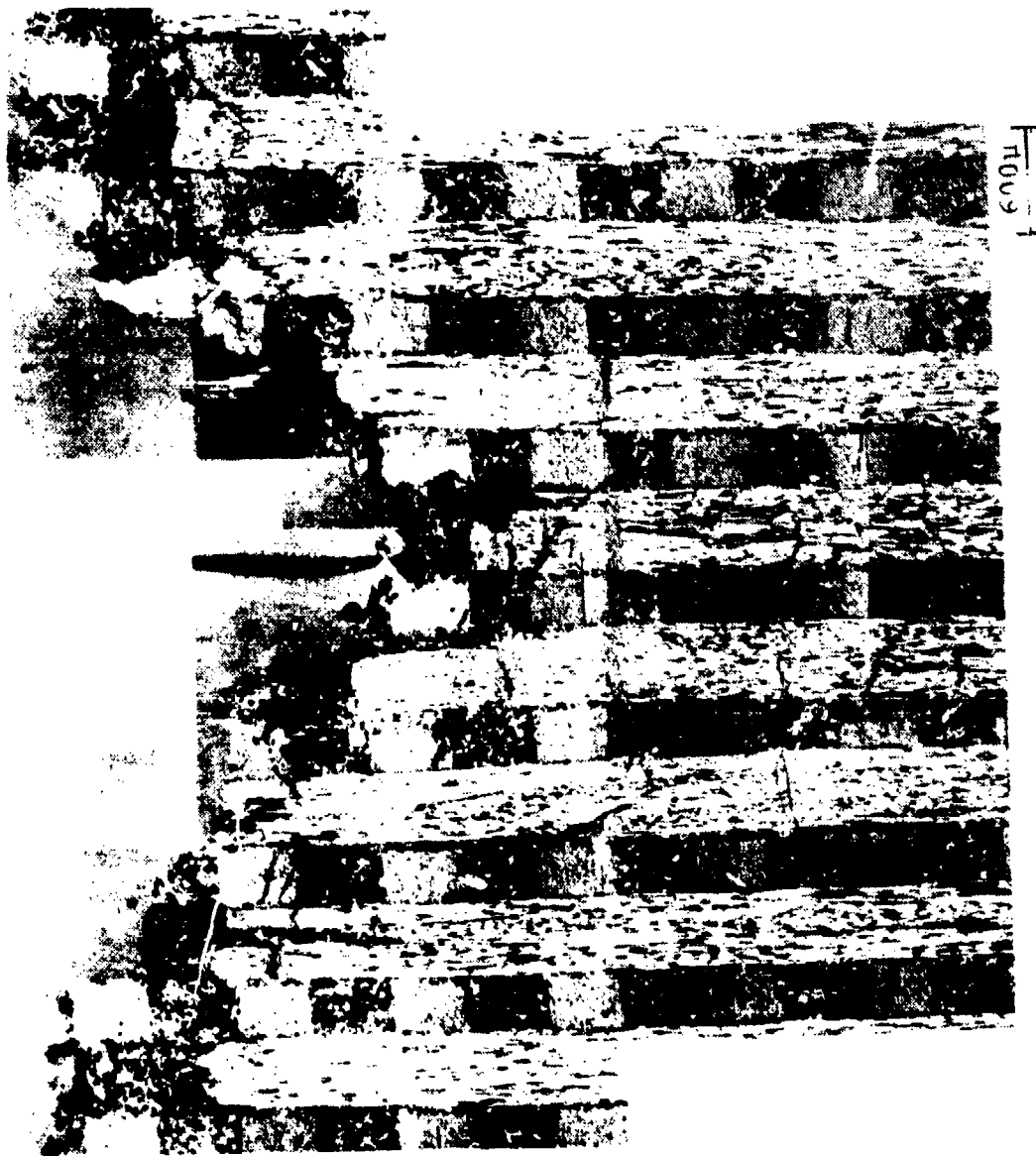


Figure 89 CROSS SECTION SHOWING EFFECT OF SINGLE PARTICLE IMPACT AT
ELEVATED TEMPERATURE ON AXIAL YARNS OF 223 T-50 (1000μ glass bead,
14.3 kfps, 3100°F)

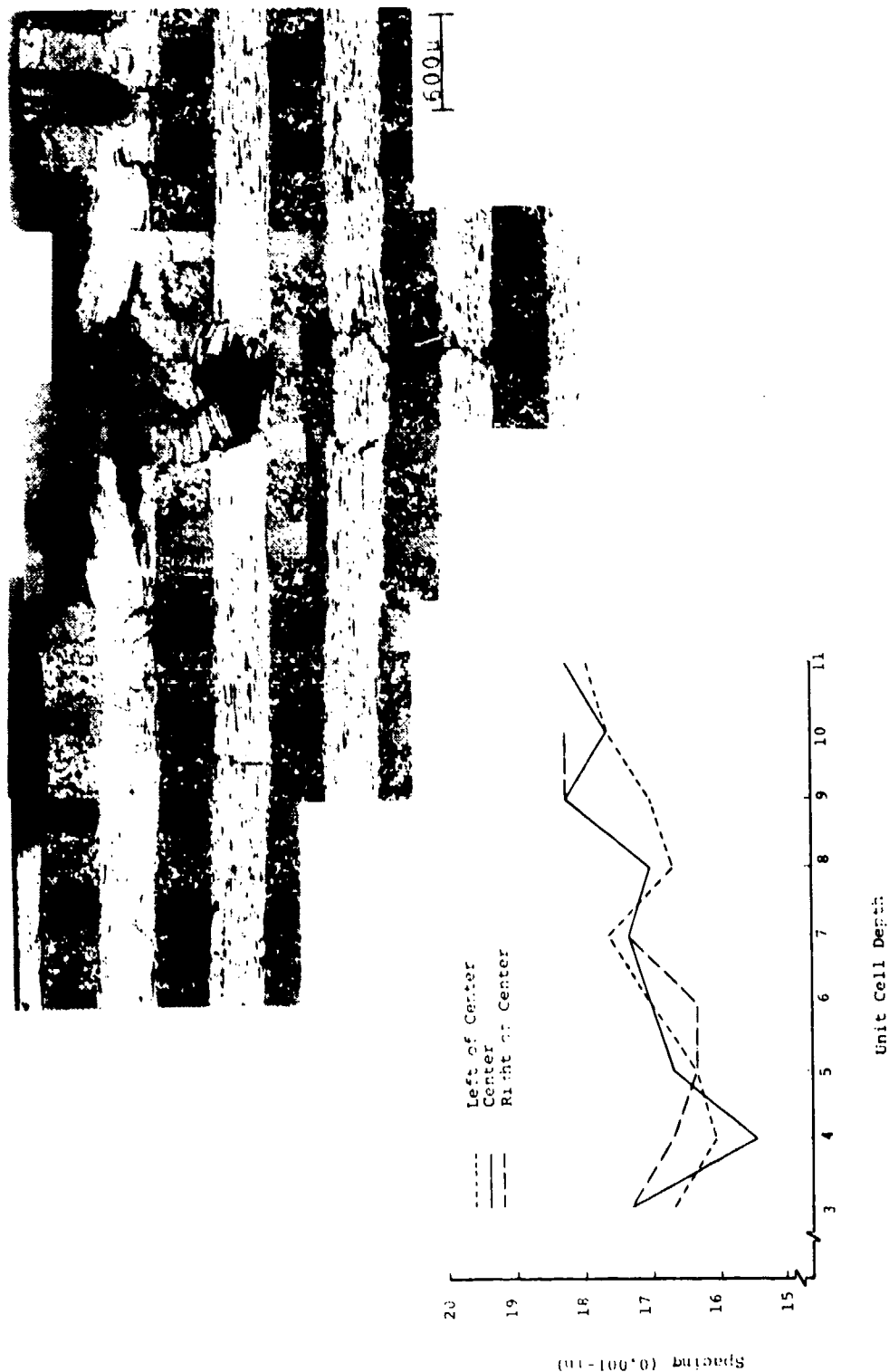


Figure 90 CROSS SECTION SHOWING EFFECT OF SINGLE PARTICLE IMPACT AT
ELEVATED TEMPERATURE ON TRANSVERSE YARNS OF 223 T-50 (1000μ
glass bead, 14.3 kfps, 3100°F)

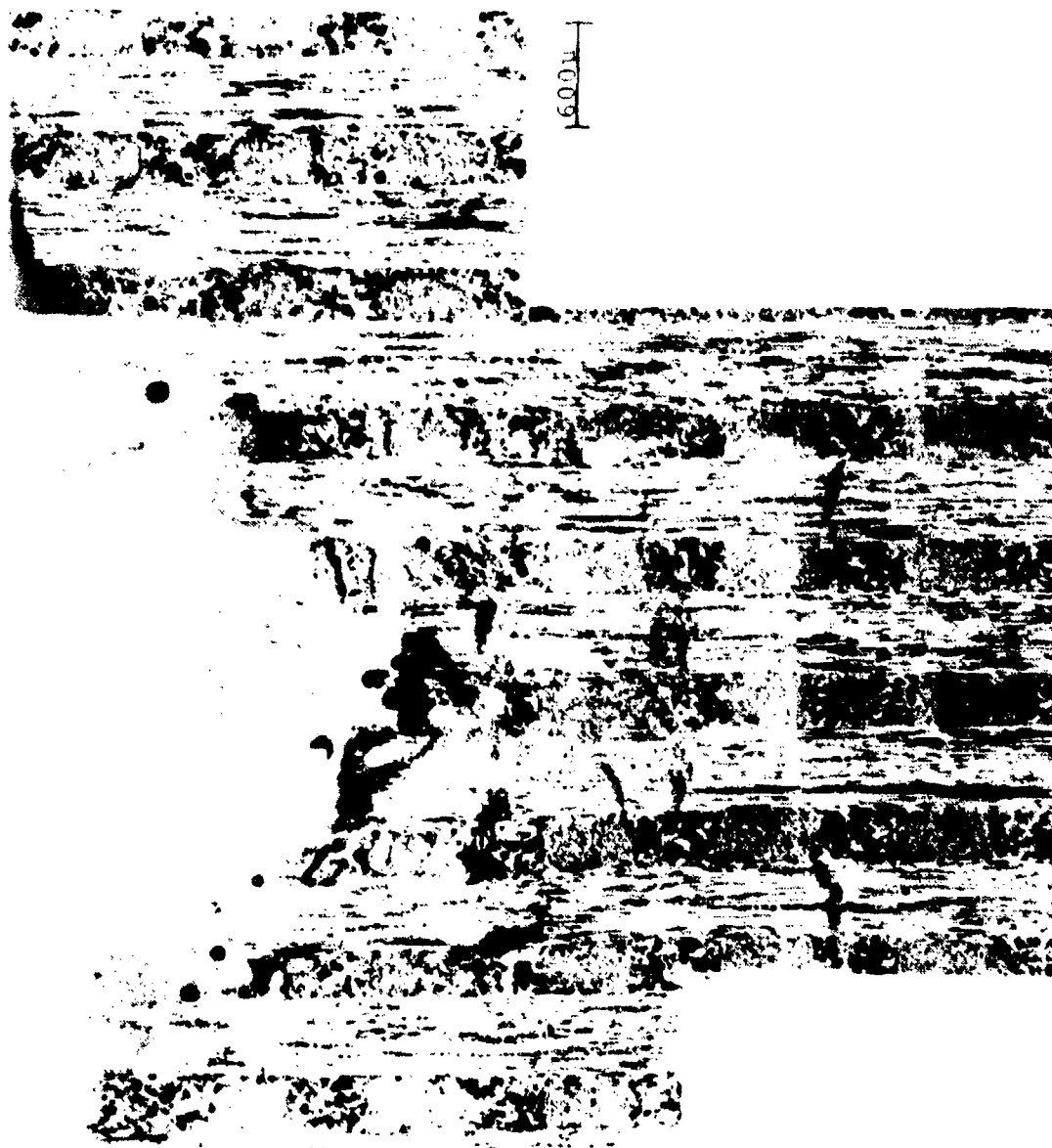


Figure 91 CROSS SECTION SHOWING EFFECT OF SINGLE PARTICLE IMPACT
AT ELEVATED TEMPERATURE ON AXIAL YARNS OF 223 PAN
(1000 μ glass bead, 14.6 kfps, 3900°F)

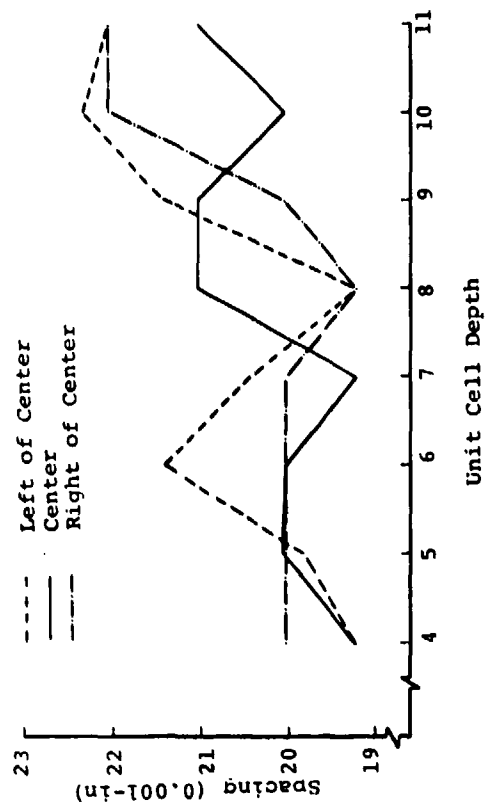
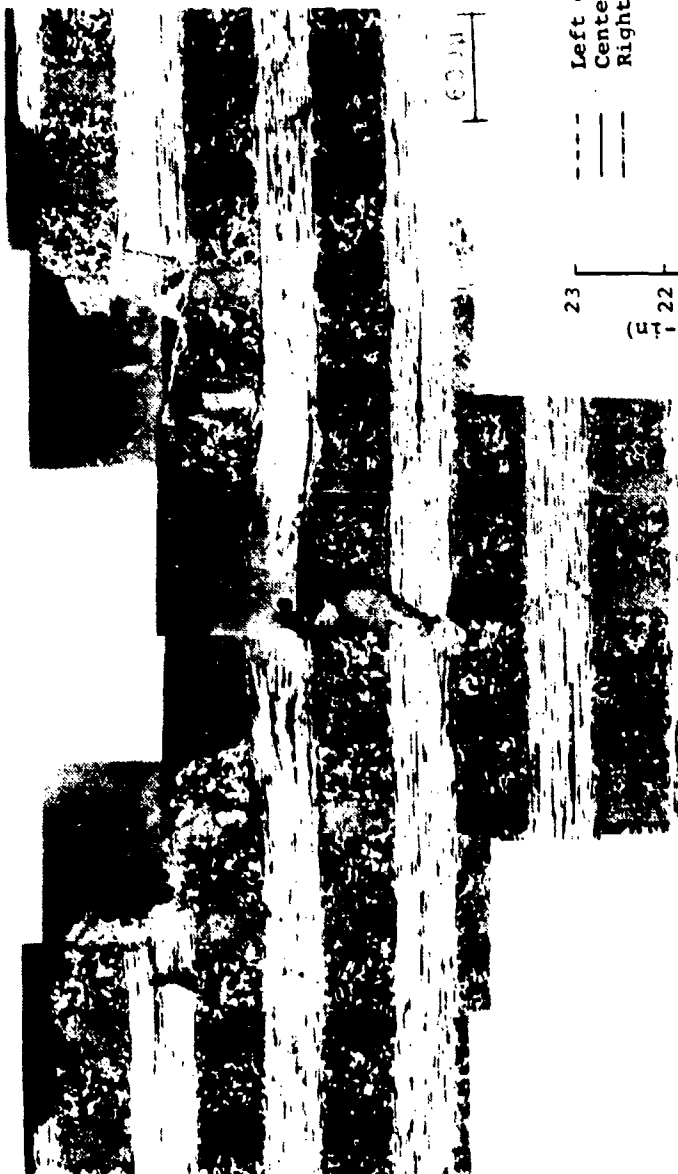


Figure 92 CROSS SECTION SHOWING EFFECT OF SINGLE PARTICLE IMPACT
AT ELEVATED TEMPERATURE ON TRANSVERSE YARNS OF 223 PAN
(1000 μ glass bead, 14.6 kfps, 3900°F)

The photomicrographs of these four specimens clearly reveal that elevated temperature is not responsible for inhibiting in-depth damage in ground test erosion models. They also show that the damage present in both standard 223 T-50 and 223 PAN is similar in nature with more tensile fracture occurring in the 223 PAN. Further, the measurements made on unit cell spacing under the impact site indicate that damage to the composite has occurred to a depth beyond that where yarn breakage can be observed. This observation is consistent with results obtained at ETI (Reference 6) in which the shear strength of material immediately below an impact site was measured. ETI reported that the shear strength of the material was degraded for an extensive distance below the point where microstructural yarn breakage had been previously observed.

The issue of small particle size was addressed in a single particle impact test in which three 350 micron particles were shot at a piece of standard 223 T-50 at room temperature at a velocity of approximately 12,000 ft/second. Cross-sections of these impacts are shown in Figure 93. As can be seen in these photomicrographs, in-depth damage is present in all views examined except when the impact was directly on the matrix pocket. However, the size of the impact site was such that the photomicrograph showing the matrix pocket is slightly off center from the immediate impact zone thereby accounting for the lack of observable in-depth damage.

3.2 Holloman Sled Test Specimens

Another series of five samples which had been tested in the rainfield on the Holloman sled were evaluated. The materials included 223 T-50, 223 PAN, Fine Weave Pierced Fabric PAN, a 1-1-1-3 4-D material (T-50) and a material designated SSN which has the standard 223 construction with metal in place of the carbon yarns

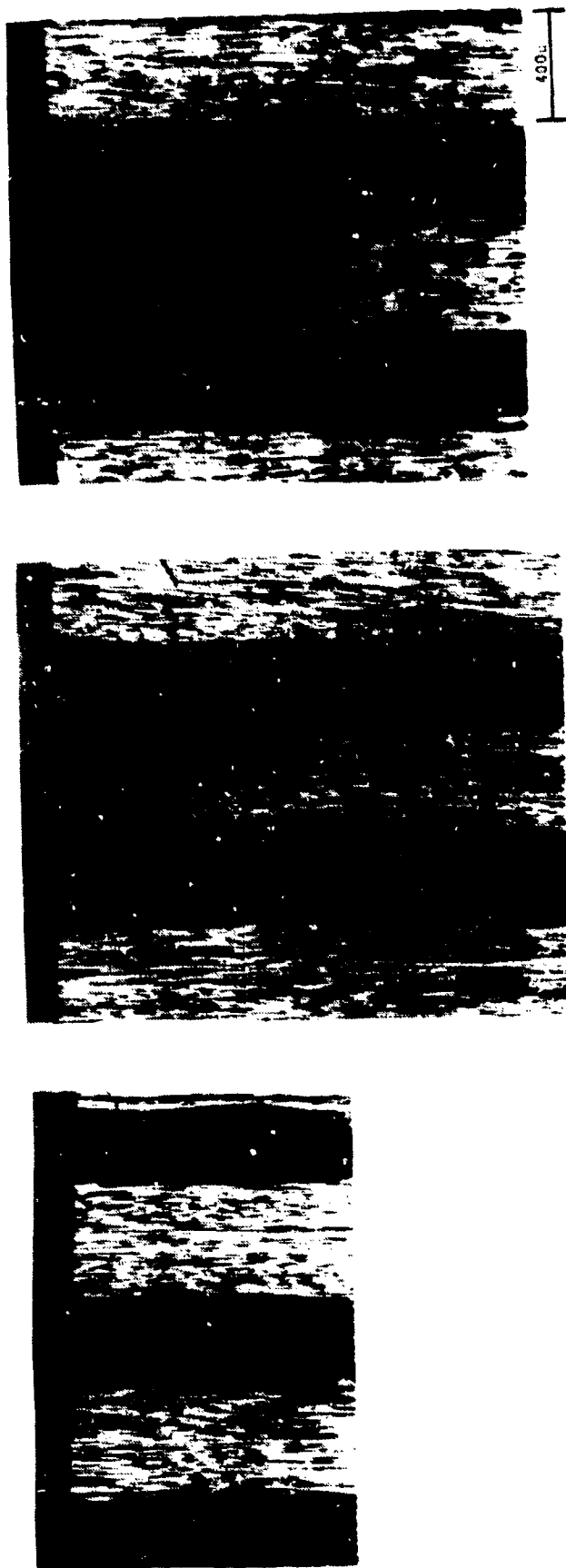


Figure 93 VIEW OF IN-DEPTH DAMAGE RESULTING FROM SMALL PARTICLE IMPACTS
(350 μ glass particles, 12 kfps)

in the direction parallel to the impact. All of the specimens were tested in a field which had raindrops with a mean diameter of 1.73 mm at a velocity of 4.2 kfps and an impact angle of 60° . It was anticipated that if flowfield effects were indeed important then the 60° orientation of the specimen would show drastic reductions in the amount of subsurface damage present even with the relatively low velocity experienced in the rainfield.

Typical cross-sections of the specimens evaluated are shown in Figures 94 through 99. As can be seen in these photomicrographs, the primary impact damage present is small cracks observable only at high magnification in the axial yarns. However, in some isolated cases more severe cracking was also observed (Figure 97) but to a much lesser extent than that observed in single particle impact tests.

It was not possible to ascertain whether any in-depth damage occurred in the SSN material. Since it appeared that the metal was relatively discontinuous, added damage was difficult to identify.

3.3 Ballistic Track (K)

A total of four samples were examined after recovery from ground tests in ballistic track K. All of these samples had been impacted using 700 micron particles at a velocity of 13 kfps. Both standard 223 and 223 PAN materials were subjected first to impact with a single particle and then to impact with two particles impacting in the same site. The standard 223 T-50 showed extensive in-depth damage retained in the impact crater with much of that damage being lost in the specimen which experienced two coincident impacts (Figure 100). The buckling and shearing of yarns parallel to the impact direction is obvious for the single impact case whereas for the double impact specimen only straight tensile fractures are present in these yarns.

TEST NUMBER 3OR-M11C
MATERIAL 223
VELOCITY 4202.25 kfps
ANGLE OF IMPACT 60°
PARTICLE 1.37mm Rain Drop

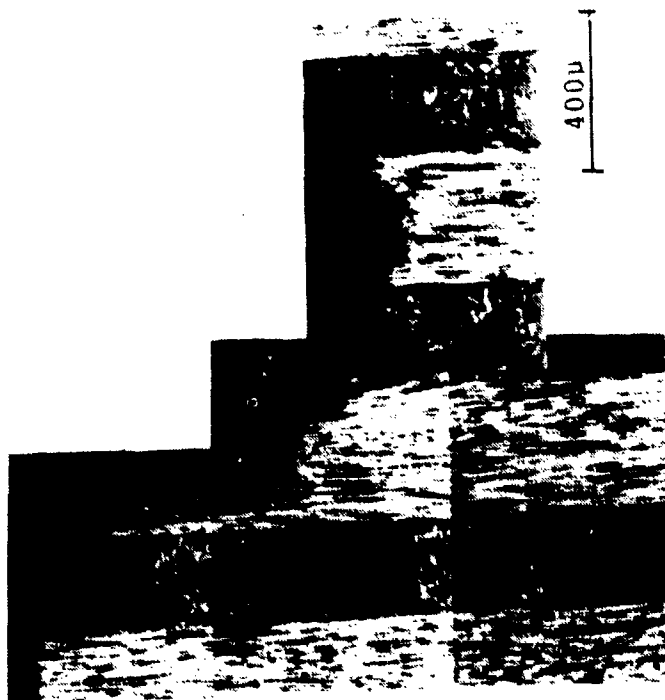
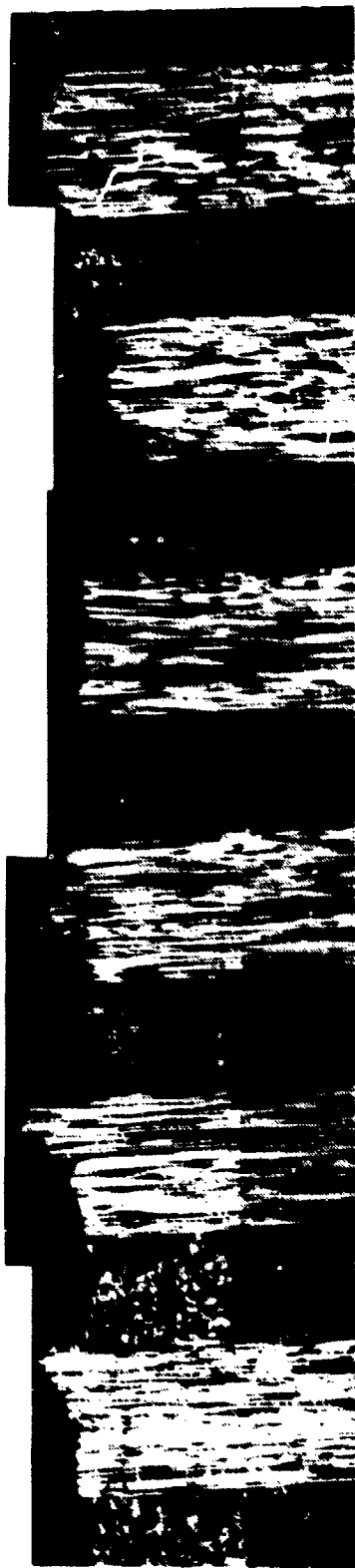


Figure 94 CROSS SECTION OF HOLLOMAN SLED TESTED 223 T-50



TEST NUMBER 3OR-M12C

MATERIAL 223 PAN

VELOCITY 4205.46 kfps

ANGLE OF IMPACT 60°

PARTICLE 1.37mm Rain Drop

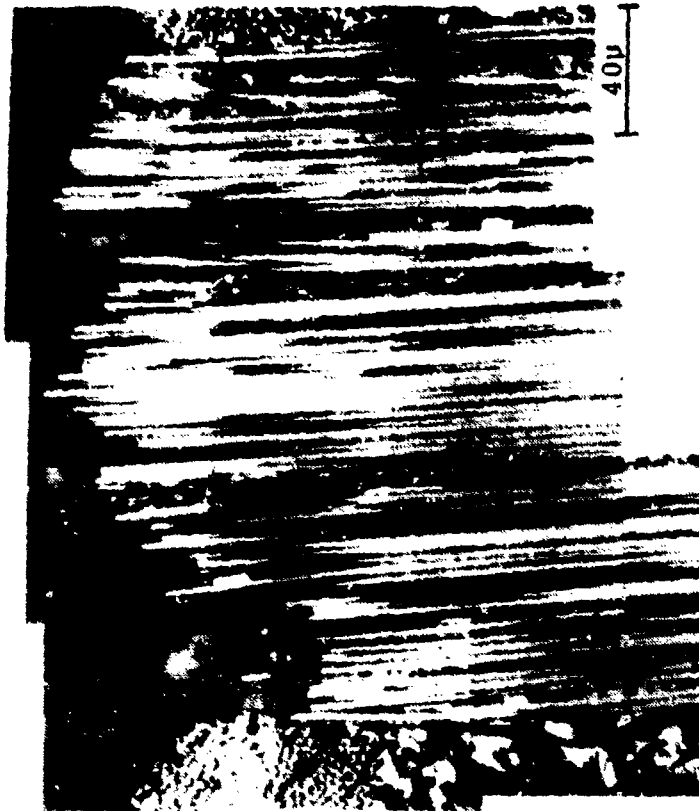


Figure 95 CROSS SECTION OF HOLLOMAN SLED TESTED 223 PAN

TEST NUMBER 3OR-M12C
MATERIAL FWPF PAN
VELOCITY 4205.46 kfps
PARTICLE 1.37mm Rain Drop



200μ



40μ



Figure 96 CROSS SECTION OF HOLLOMAN SLED TESTED FWPF PAN

TEST NUMBER 30R-M11C
MATERIAL 1-1-1-3
VELOCITY 4202.25 kfps
ANGLE OF IMPACT 60°
PARTICLE 1.37mm Rain Drop

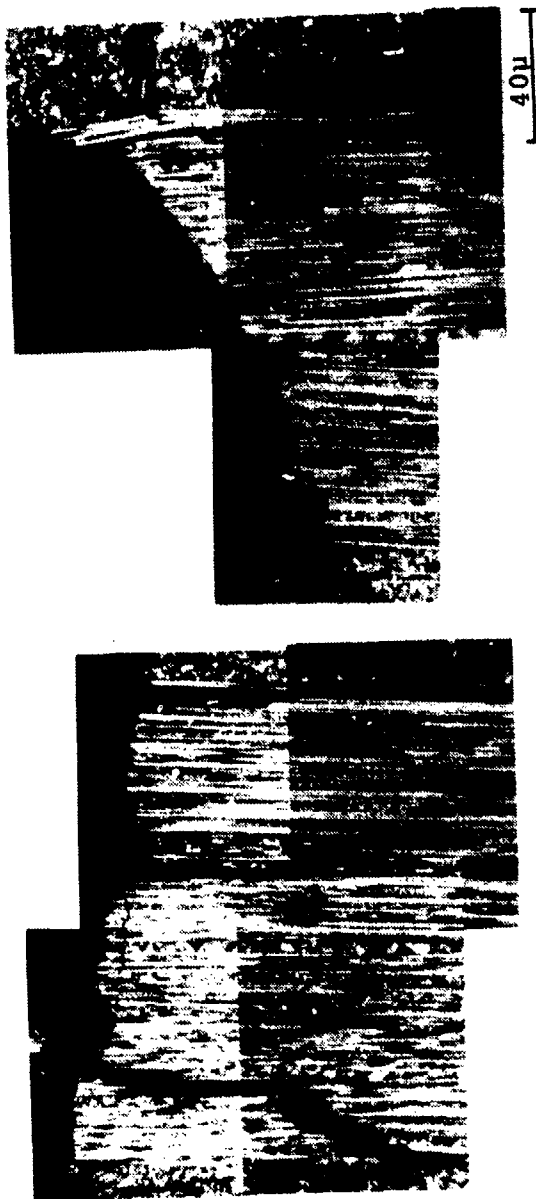
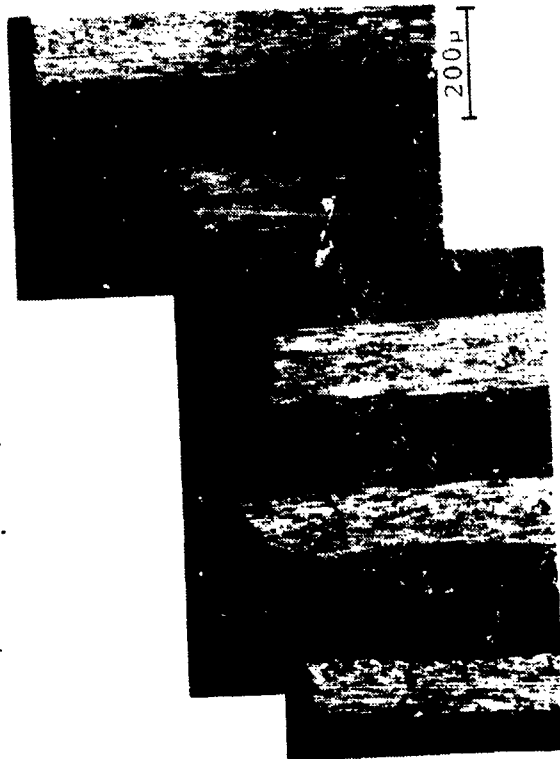


Figure 97 CROSS SECTION OF HOLLOMAN SLED TESTED 1-1-1-3 SHOWING
ISOLATED IN-DEPTH DAMAGE

TEST NUMBER 30R-M12C
 MATERIAL SSN
 VELOCITY 4205.46 kfps
 ANGLE OF IMPACT 60°
 PARTICLE 1.37mm Rain Drop

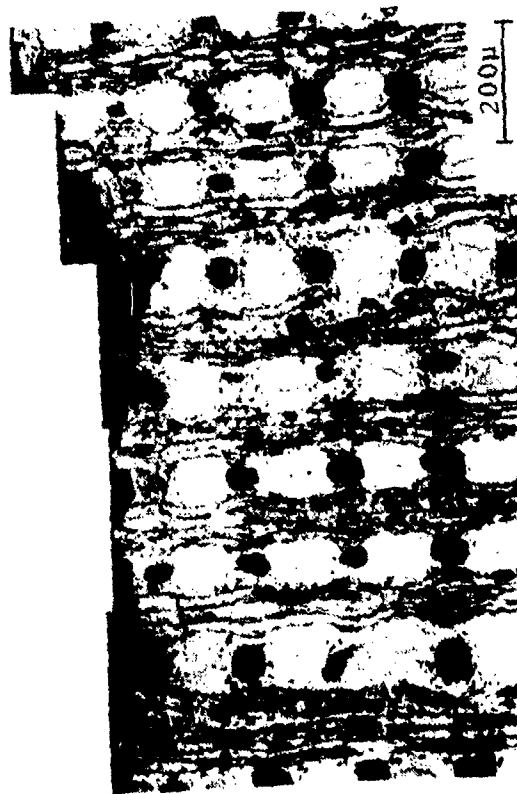
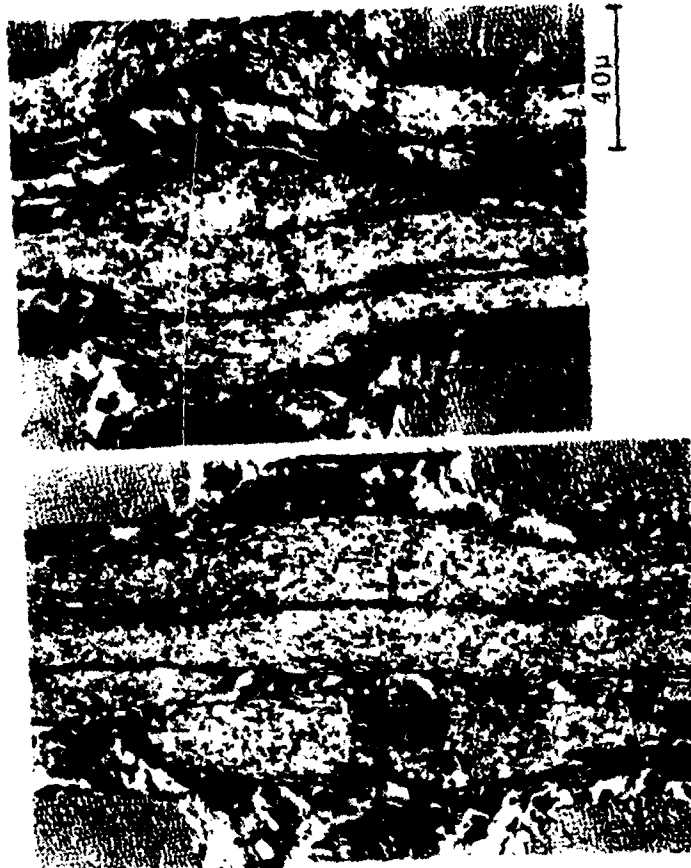


Figure 98 CROSS SECTION OF HOLLOMAN SLED TESTED SSN MATERIAL

TEST NUMBER 3OR-M12C
 MATERIAL SSN
 VELOCITY 4205.46 kfps
 ANGLE OF IMPACT 60°
 PARTICLE 1.37mm Rain Drop

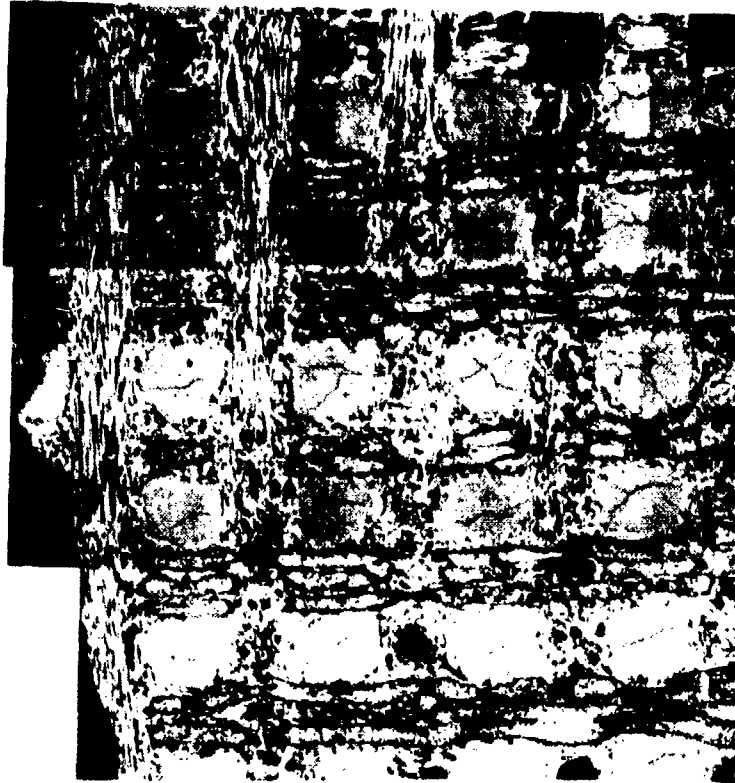


Figure 99 CROSS SECTION SHOWING TRANSVERSE YARNS IN HOLLOMAN SLED TESTED
 SSN MATERIAL



SINGLE IMPACT
Large Amount of Shear
and Buckling of Z Yarns



TWO IMPACTS IN SAME SITE
Tensile Fractures Only
in Damage Zone

Figure 100 CROSS SECTIONS SHOWING EFFECTS OF SINGLE IMPACT AND TWO IMPACTS ON STANDARD 223 (13 kfps, 700 μ particles, Track K)

contrast, the 223 PAN material (Figure 101) showed no extensive in-depth yarn fracture even after the single particle impact. The subsequent impact into the same zone appeared primarily to widen the impact site rather than increase its depth. For 223 PAN (Figure 102), the transverse yarns and matrix pockets appear to be removed around the impact crater with Z yarns protruding from the surface. The behavior of these materials in track K under single and multiple particle impact appears to point to the fact that both flowfield effects and multiple particle impact phenomena are responsible for the lack of in-depth damage in multiple impacted ballistic range samples.

3.4 Ballistic Track (G)

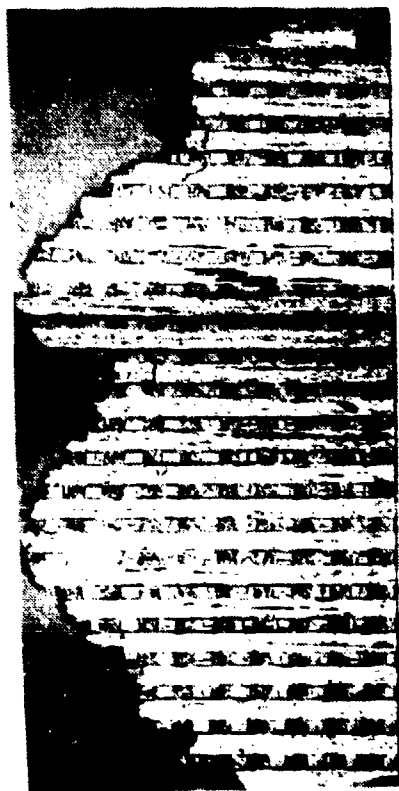
A total of 8 ballistic range models which had been tested in track G and recovered for post-test examination were evaluated. The initial sample had been impacted by large welding debris on the initial part of its flight down the range. While the character of this welding debris is not specifically known, the value of this specimen is that it clearly indicates that loss of predamaged material in the recovery tube is not a likely mechanism for removal of material which has been damaged during the impact event. While this type of material removal cannot be completely ruled out, the prior photomicrographs shown earlier indicate that multiple particle effects combined with a dynamic flowfield is a more likely cause for removal of predamaged material (Figure 103). Typical examples of the remaining materials tested are shown in Figures 104 through 107. These include standard 223 T-50 and 223 PAN tested with both dust and snow as the impacting particle. In all cases microcracks observable only at very high magnifications could be found in these samples. Yarn failures, such as that shown in Figure 103 and in typical single particle impact tests, were totally absent. In most cases,



Figure 101 CROSS SECTION SHOWING THE EFFECT OF A SINGLE IMPACT ON
223 PAN (13 kfps, 700 μ particle, Track K)



Figure 102 CROSS SECTION SHOWING THE EFFECT OF TWO IMPACTS ON 223
PAN (13 kfps, 700 μ particles Track K)

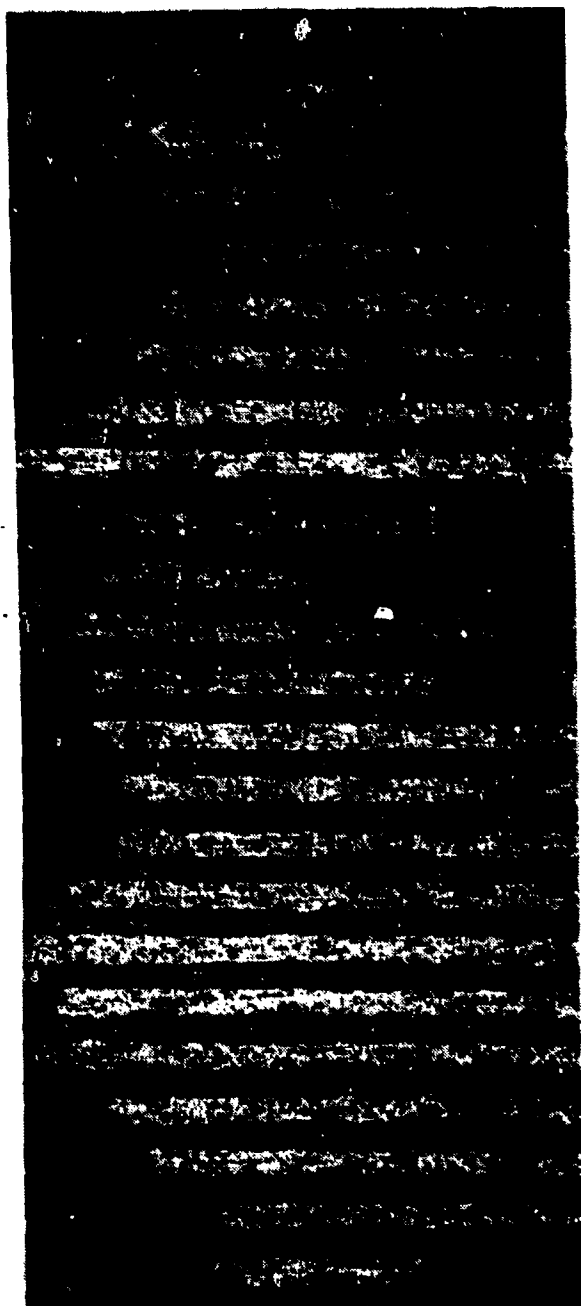


OVERALL SURFACE 10x



TYPICAL IN-DEPTH
DAMAGE 403x

Figure 103 CROSS SECTIONS OF GE 223 T-50 SHOWING EFFECT OF IMPACT BY
WELDING DEBRIS ON INITIAL PART OF FLIGHT (16 kfps, Track G)



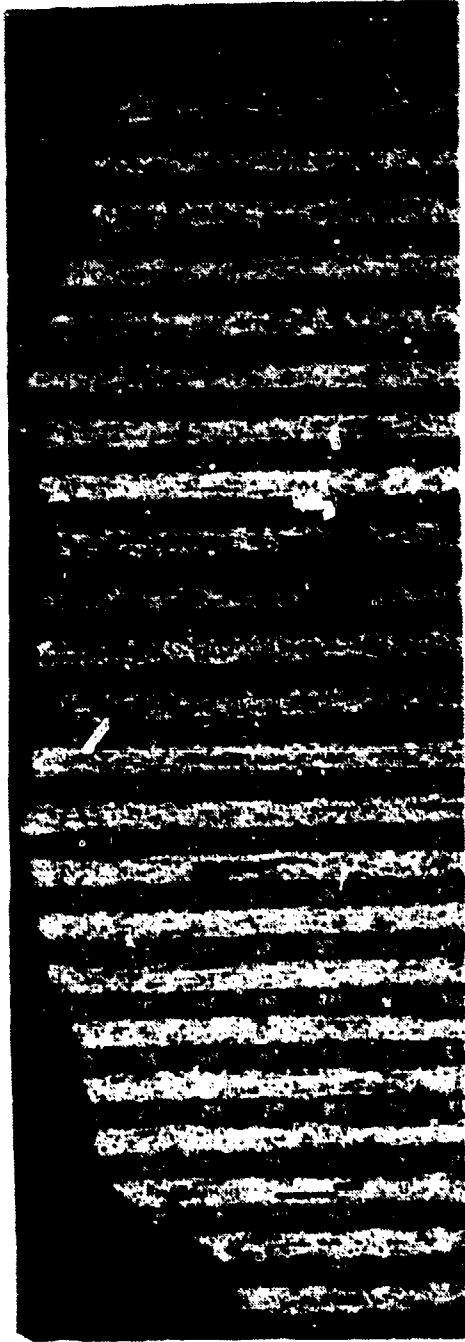
10x

OVERALL SURFACE



TYPICAL IN-DEPTH
DAMAGE

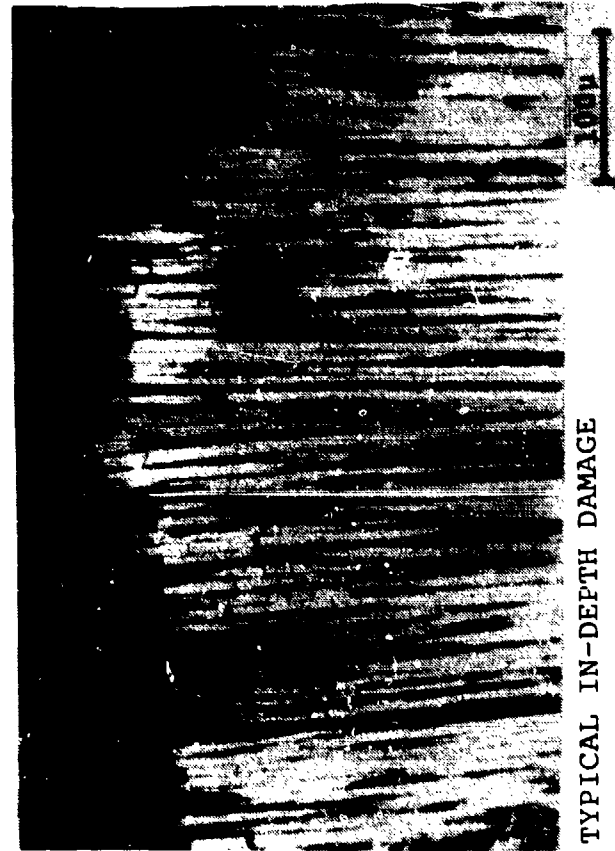
No In-depth Damage
Observed at
Lower Magnification



10x

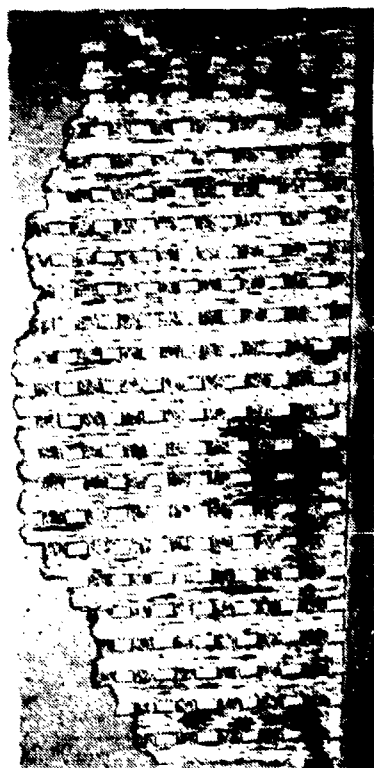
OVERALL SURFACE

No In-depth Damage
Observed at
Lower Magnification



TYPICAL IN-DEPTH DAMAGE

Figure 105 CROSS SECTIONS OF GE 223 T-50 IMPACTED BY SNOW (17 kfps, Track G)



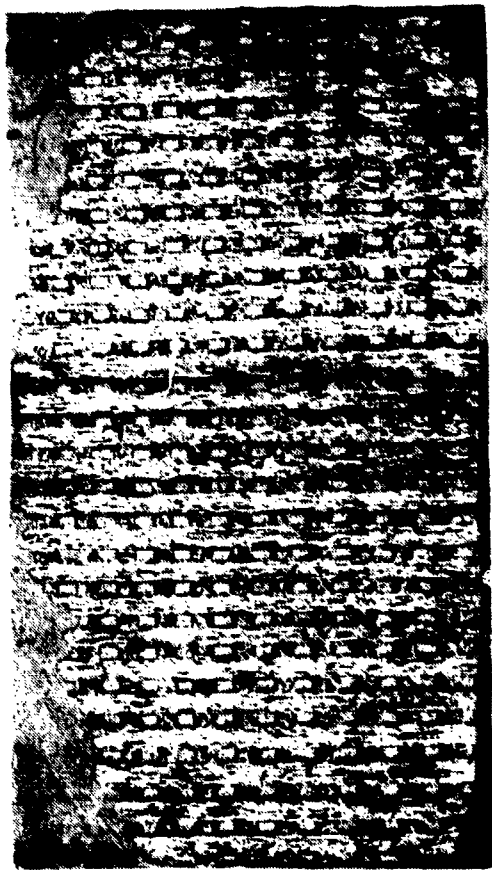
OVERALL SURFACE 10x



TYPICAL IN-DEPTH DAMAGE 100x

No In-depth Damage
Observed at
Lower Magnification

Figure 106 CROSS SECTIONS OF 223 PAN IMPACTED BY DUST (16.9 kfps, Track G)



OVERALL SURFACE 10x

No In-depth Damage
Observed at
Lower Magnification

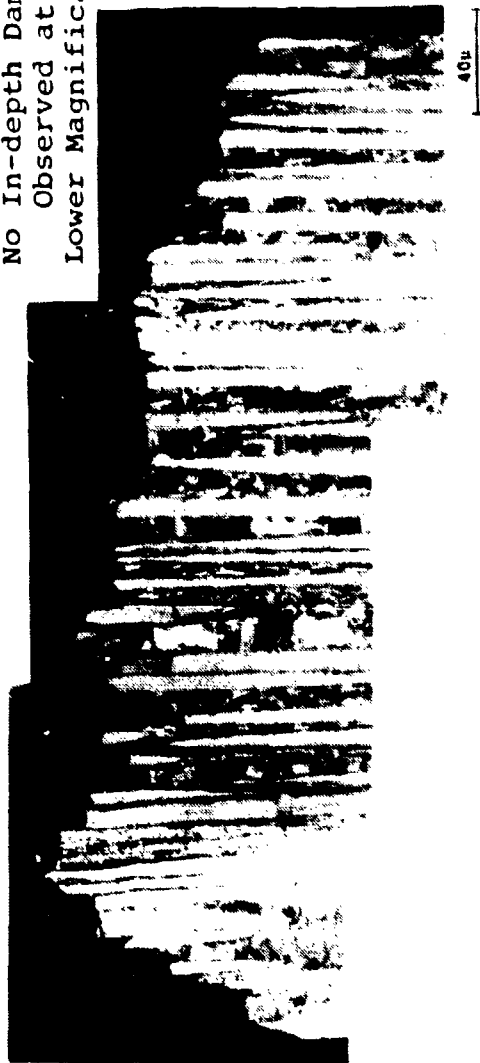


Figure 107 CROSS SECTIONS OF 223 PAN IMPACTED BY SNOW (16.9 kfps, Track G)

as seen in Figures 104 and 107, axial yarns protrude from the surface of the specimen after testing. This indicates that both the transverse yarns and the matrix pockets were significant contributors to mass loss in the impact event. This further indicates that improvements in material performance which address these material constituents (transverse yarns and matrix pockets) may have the potential for improving the erosion performance of the carbon-carbon family of materials.

4.0 CONCLUSIONS AND RECOMMENDATIONS

The results presented in this document, when considered in light of the analytical modeling efforts described in Reference 5, and with ongoing erosion modeling activity (AFML contract AF33615-78-C-5059), show that definite relationships exist between the microstructural characteristics of carbon-carbon composite materials and their performance in a simulated reentry environment. Based on this data the following conclusions and recommendations can be made.

1. The molecular permeability coefficient, B , has been shown to be a strong correlator of transition performance (Reference 5). Ablation models from billets fabricated by two different vendors were characterized prior to flight tests with the results showing that one of these materials, (Billet 399), had considerably higher permeability than did the other (Billet 408). This difference was pointed out in an interim report on this program (Reference 7). Subsequent flight test results showed that the material with the high permeability coefficient had a recession rate which was typical of fairly high altitude transition. The material with lower permeability appeared to stay laminar throughout the flight. While the flight test

conditions were not exactly the same - the low recession material was on a "bent" nosetip configuration - the differences in recession during flight were too significant to be explained by the configuration difference. In view of this correlation with flight test results, it is recommended that all carbon-carbon nosetip billets be characterized to determine the molecular permeability coefficient as a part of their receiving-inspection data package. This would involve tests to determine the bulk density, open porosity, data obtained from a permeability test, and data obtained from a mercury porosimetry test. All of these tests require less than .5-inch³ of material.

2. Topographical mapping and the appearance of the AVCO "Jellyroll" material strongly suggests the influence of macroscale roughness (on the order of yarn bundle size) on transition behavior. Modeling efforts to date have concentrated on utilizing roughness measurements made on much smaller scale discontinuities. It is therefore recommended that future analytical modeling efforts address the influence of gross surface topography in transition performance.
3. Sufficient microroughness data has now been obtained on laminar ablation models to input in future transition modeling efforts. However, it should be noted that the microroughness measurements on Fine Weave Pierced Fabric were considerably less consistent than those obtained for woven constructions. It is recommended that the data obtained in both this report and in Reference 5 be utilized in any current or future ablation modeling efforts.

4. Microstructural examination of erosion models clearly show that major differences exist in the material response for various ground tests. This information is currently being used to provide comparisons with erosion modeling efforts on contract F33615-78-C-5059. Particle size, elevated temperature, and flowfield effects continue to be issues that should be addressed in modeling efforts in order to provide material developers with direction in their material improvement efforts. It is therefore recommended that continued microstructural examination of tested erosion samples be conducted to provide material response information in support of these modeling efforts.

REFERENCES

1. S. Brunauer, P.H. Emmet, and E. Teller. BET Method. J. American Chem. Soc. 60, 309, 1938.
2. D. A. Eitman and J. D. Binder. Evaluation of Post-Test Ablation Models. Interim Report SAI-061-76-09-002. September, 1976.
3. P.I.C. Wiggs. The Relation Between Gas Permeability and Pore Size Distribution in Consolidated Bodies. Industrial Carbon and Graphite, Society of Chemical Industry. London, 1957.
4. R. B. Dirling, Jr. A Method for Computing Roughwall Heat Transfer Rates on Reentry Nosetips. AIAA Paper No. 73-763. July, 1973.
5. R. B. Dirling, Jr., D. A. Eitman, and J. D. Binder. Evaluation of Post-Test Ablation Models. Technical Report AFML-TR-77-225. Final Report for Period March 1976 - October 1977.
6. Industry Erosion Conference at Effects Technology, Inc., Santa Barbara, CA.
7. D. A. Eitman. Material Characterization of Post-Test Ablation Models. First Interim Report SAI-061-78-10-02. October 1978.

TABLE 7 MODEL TEST AND MATERIAL DESCRIPTION

MODEL	TEST CONDITIONS	BILLET NO.	MATERIAL DESCRIPTION
AFML-19R	Peaked Enthalpy	JR-4-2-R1	AVCO low pressure process, pitch and resin matrix precursor, "Jellyroll" construction
AFML-23R		881-R1	AVCO low pressure process, pitch and resin matrix precursor, FWPF
GE-01A		399-R1	Standard GE 223T-50 (ANT III Billet)
GE-02A3		408-R2	MDAC densified 223T-50 (ANT III Billet)
GE-04A3		HAT-2-R2	223 PAN, A-240 pitch matrix precursor, no CVD, 10 ksi process (ANT III A Billet)
GE-06A3		PF920-R1	FWPF with PAN (ANT II Billet)
SR-07AD		111P1-R2	FMI processed pitch yarn material, no CVD
SR-08AD		111P2-K2	FMI processed pitch yarn material with CVD
SR-10D		1819-3-R2	223 PAN, no CVD, 2750°C graph temp.
SR-12D		1819-5-R2	223 PAN, no CVD, initial LoPIC, 2750°C graph temp.
SR-13D		1819-RZ1	223 PAN with CVD, 2300°C graph temp.
GE-07A		425-R3	223 ENKA (T-50), Y-12 standard process, (ANT II Billet)
GE-39A		426-R4	223 PAN, standard process, (ANT II Billet)
GE-44A		427-R4	223 PAN, standard process (ANT III Billet)
AC-02N		921-RZ	FWPF
AC-03N		921-R7	FWPF

TABLE 7 (continued) MODEL TEST AND MATERIAL DESCRIPTION

<u>MODEL</u>	<u>TEST CONDITIONS</u>	<u>BILLET NUMBER</u>	<u>MATERIAL DESCRIPTION</u>
GE-02PA	Peaked Enthalpy	PF928	FWPF PAN, Standard GE Five-Cycle processing (HPIC), ANT-3A material.
SR-25PA	Peaked Enthalpy	903-1-RZ2	FWPF PAN, HIPIC four-cycle processing at MDAC, 2300°C graphitization 223-PAN, 10KSI processing
HAT-5	Peaked Enthalpy		223-PAN
427-HS1	Steady State	427	223-PAN
427-HS2	Steady State	427	FWPF PAN, EISP Process
PF928-HS2	Steady State	PF928	FWPF PAN, EISP Process
PF928-HS3	Steady State	PF928	223-PAN EISP Process
668-11-HS2	Steady State	668-11	

DISTRIBUTION LIST

Ballistic Missile Office
BMO/SYDT
Attn: Maj. K. Yelmgren (2)
Norton AFB, CA 92409

Defense Technical Information Center (2)
Cameron Station
Alexandria, VA 22314

Air University Library
Maxwell AFB, AL 36112

TRW DSSG
Attn: W. Grabowsky (2)
P. O. Box 1310
San Bernardino, CA 92402

TRW Systems Group (2)
Attn: J. Ohrenberger
M. Gyetvay
1 Space Park
Redondo Beach, CA 92078

Headquarters, Arnold Engineering
Development Center
Arnold Air Force Station
Attn: Library/Documents
Tullahoma, TN 37389

Armament Development and Test Center
Attn: Technical Library, DLOSL
Eglin AFB, FL 32542

Air Force Wright Aeronautical Laboratories (3)
Air Force Systems Command
Attn: M. Buck (AFWAL/FIM)
R. Neumann (AFWAL/FIMG)
V. Dahlem (AFWAL/FIMG)
Wright-Patterson AFB, OH 45433

U. S. Army Ballistic Missile
Defense Agency/ATC-M
Attn: J. Papadopoulos
P. O. Box 1500
Huntsville, AL 35807

Director, Defense Nuclear Agency
Attn: J. Somers (SPAS)
Washington, DC 20305

Naval Surface Weapons Center
Attn: Carson Lyons/K06
White Oak Laboratories
Silver Spring, MD 20910

Acurex Aerotherm
Aerospace Systems Division
Attn: C. Nardo
485 Clyde Avenue
Mountain View, CA 94042

Avco Systems Division
Attn: N. Thyson
201 Lowell Street
Wilmington, Mass 01887

General Electric Company
Attn: R. Neff
3198 Chestnut Street
Philadelphia, PA 19101

Lockheed Missiles and Space Co.
P. O. Box 504
Attn: G. T. Chrusciel
Sunnyvale, CA 94086

McDonnell Douglas Astronautics Co.
Attn: J. Copper
5301 Bolsa Avenue
Huntington Beach, CA 92647

PDA Engineering
Attn: M. Sherman
1560 Brookhollow Drive
Santa Ana, CA 92705

Sandia Laboratories
P. O. Box 5800
Attn: Library
Albuquerque, NM 87115

Science Applications, Inc.
Attn: A. Martellucci
994 Old Eagle School Road
Suite 1018
Wayne, PA 19087